Eta Production at High Transverse Momentum by Negative 520 GeV/c Pions Incident on Beryllium and Copper Targets

by

Robert Martin Roser

Submitted in Partial Fulfillment
of the
Requirements for the Degree

Doctor of Philosophy

Supervised by
Professor Paul Slattery

Department of Physics and Astronomy
College of Arts and Science

University of Rochester
Rochester, New York

1994

Curriculum [redacted]

Robert Martin Roser [redacted] In 1980, upon graduating from high school, he left Glastonbury for Storrs Connecticut, a small farming community and home of the University of Connecticut. There, under the guidance of Quentin Kessel, he began his career in physics.

He spent four years in Storrs at the University majoring in physics. Most of his time was spent, while not attending classes, or training for triathlons, working in Kessels' Van De Graaff Accelerator Laboratory. There, he helped design, construct, and perform a heavy ion-atom collision experiment. It was in this lab he first developed a feel for electronics, vacuum systems, accelerators, cryogenics, and how to solve challenging problems involving electronic noise. The author graduated Magna Cum Laude in 1984 with 4 co-authored journal publications to his credit. He was elected to Phi Beta Kappa, Sigma Xi, and Mortar Board.

Upon completion of his Bachelor of Science degree, the author left his home state for western New York to attend graduate school in physics at the University of Rochester. At Rochester, he was awarded a Rush Rhees Fellowship and immediately began working on Fermilab experiment E706 as a research assistant along with professors Fred Lobkowicz, Tom Ferbel, and Paul Slattery. In the fall of 1986, after completing all of his course work and preliminary examinations, the author left Rochester for approximately three years to pursue several entrepreneurial ventures. Although these ventures proved quite successful, the lure of physics brought him back the spring of 89 to complete his PhD work.

Six of the past 9 years were spent on E706, where the author was involved with all facets of the experiment except for the proposal stage. He started working on the design and construction of the large liquid argon calorimeter (LAC). He co-designed and co-authored the LAC data acquisition system employed during the 1990 and 1991 runs. He was involved with the operation of the large cryogenic systems, and participated in the design and development of the Monte Carlo simulations. Finally, he participated in the data taking for both the 1990 and 1991 Fermilab fixed target runs, and ultimately in the detailed data analysis.

Acknowledgements

It is currently mid-March and that means it is NCAA tournament time, a special brand of "March Madness" that a popular television station is fond of advertising. Over these past few weeks I have had my own brand of "March Madness" – somehow trying to write a rather terse document which does justice to my previous 5 years worth of effort. As with any journey, it was not possible to accomplish it alone. I wish to take this opportunity to thank some of the people who, whether they were aware of it or not, have helped and influenced me along the way.

First and foremost, I wish to thank my parents David and Joan Roser. They never discouraged me from trying something new, and although what I now do for a living is not something that is easily explained to their peers, their love and support has never wavered.

Professor Quentin Kessel at the University of Connecticut taught me how much fun experimental physics can be. I will never forget that fateful day when he walked into the introductory physics class I was taking and indicated that he was looking for a student to machine some experimental apparatus. I promptly joined him and spent the rest of my undergraduate career working in his lab. It was great fun. To Robert Rubino, my partner in crime and the other half of the "R-4" team in Kessels' lab, thanks for everything – you are still one of the best experimental physicists I have met.

While at the University of Connecticut, I was fortunate enough to make friends with Jim and Wendy Koch. Thank you both for helping me keep my undergraduate career in perspective. In other words, thanks for all the dinners, beers on the porch, and those wonderful fall bicycle training rides through the

Connecticut countryside. You two were always available for a workout and are wonderful friends that I have managed to keep in close contact with. And yes Wendy, I forgive you for winning all of those road racing trophies while I struggled to finish a distant 24th.

My advisor, Paul Slattery, has been nothing short of inspiring. A frequent flyer fanatic – who lives by the motto "It's Friday, it must be Fermilab". Thanks Paul for your support and confidence in me. After nearly a three year absence from high energy physics, I called Paul and asked if he could find room on E706 for his old student – the lure of physics had proved stronger than I realized when I left. Paul accepted me back immediately even though he was fully aware that the lifestyle of a graduate student in high energy physics would be quite different than the lifestyle I had grown accustomed to. The rest is history and I have never regretted that decision to come back.

I am also indebted to the secretaries and support staff in Rochester. They provided the vital link between the University and Fermilab as well as a friendly voice on the other end of the phone. Thank you Bettys' Cook and Bauer, Connie Jones, Judy Mack, Sue Brightman, and Barbara Warren. Ovide Correveau's efforts in the purchasing and acquisition of materials made E706 possible. A special thanks to Ovide for letting me help coach his sons hockey team for the two years I was in Rochester. We had alot of fun together and I came to appreciate the love, and devotion this French-Canadian brings to ice hockey. I also learned that you can get away with a great deal if you yell at the referee's in french. You feel better and luckily they have no idea what you are saying. Thank you Tom Haelen for toughening my hide, and never letting me forget how I immediately cap-sized your sailboat one afternoon on the lake.

Thanks go to George Ginther, the conscience and heart of our experiment. He has done much of the "dirty" work and book-keeping that has made this experiment famous. George and I have been in a number of precarious situations – from being "half-ass" electricians at 3:30 a.m. fixing cryogenic pumps, to realigning the hodoscope 243 times. George has also read this thesis more times than I have. Thank you again, we all appreciate your efforts. Thanks as well to Brajesh Chaudary, my house mate for nearly three years. We never agreed on anything – but it sure was interesting. I take full credit for any of the conservative tendencies he is now showing later in life. Thanks as well to Len Apanasevich, Steve Blusk, Paoti "Air" Chang, Mark Shaw, Rick ("I am open when I get out of my car") Jesik, and the rest of the basketball gang. While it usually is not pretty, it sure is alot of fun. And thank you Casey Hartman and Robin McCloskey for your friendship over the years. Casey was such a friend that he left town to defend his thesis during the Pistons-Bulls playoff games just so that I could escort his charming wife. I still owe you Wimbledon tickets! And to Pat Lukens – thanks for the canoe trips and for letting your wife drag you on vacations that don't require a canoe, fishing pole, or even a sleeping bag. Sally and I had fun while you two were away!

Thanks to John Mansour, Dane Skow, Chris Lirakis, and to the rest of the E706 gang for making this experiment more like a family and less like a job. A special thank you to Nikos Varelas. Our careers at MWEST seem to parallel each other. I write half the data acquisition system, he writes the other. I write the Monte Carlo, he does the LAC energy scale. I write my thesis on one neutral meson, his is on another. It has been great fun working with you and I could not have done this without you. If history repeats itself, I will find TOP on CDF, and you will find it on D0 (albeit a few years later... and with much larger error bars).

Several people made important contributions to the success of E706 whose names will not appear on the lists of authors for our papers. A special thanks to Dan Ruggiero – the caretaker of MWEST and the people who live there. Dan has been an essential part of this experiment handling everything from electronics repairs to running the computer farms. He handles all chores that do not involve a sharp instrument with ease. Thank you as well for introducing me to really spicy food, I think. Thank you as well to Mr. Shi for keeping our FASTBUS system going. A further thank you goes to Paul Madsen. We appreciate all of your help and enthusiasm you bring each and every summer to MWEST as well as the lively lunchtime conversations. Thank you Ann Keane for all your help and friendship and for being a willing diversion when I needed one.

Maureen Hesney, one of several people I worked with during my leave of absence from physics, deserves a great deal of praise. She listened to what she first described as my "hair-brained" solution to a problem but she had enough confidence in the two of us to pursue it anyway. Together we reshaped the way companies view documentation. It was a fun time in my life and an experience I will always remember.

To Carl Bromberg, physicist and race car driver extrordinaire. Thanks for your friendship and guidance throughout the years. I have learned a great deal of physics from you during discussions to and from the race tracks. I have also learned more than I ever wanted to about repairing Triumph Spitfires – from broken axles, blown up spark plugs, blown head gaskets, (Did I mention broken axles?), and the like. In an odd sort of way, I suppose I should say thank you for your off-road "excursion" at Indianapolis Race Park. It was in the Emergency room, during surgery, and in the recovery room that I got to know my girlfriend Kirsten Tollefson. Kirsten is a truly remarkable woman and physicist, who

for some reason wants to spend time with me. A heartfelt thanks Kirsten for getting me through all aspects of this experiment – from putting up with very short dates on those days in which I was on the 4:00 a.m. to noon shift and needed some sleep, to the past 6 months of my saying "I am almost done." Most of all, thank you for making every day special.

Last but not least, I wish to thank my two brothers Jamie and Mark Roser – my two best friends. Thanks guys for always being there for me. You are constantly testing the limits of what is possible. Your goals and achievements are a constant source of strength. I am sure the three of us will one day stand together at The Brickyard – with a victory!

Abstract

This thesis presents a measurement of the production of high transverse momentum η mesons by a 520 GeV/c ($\sqrt{s} = 31.2$) π^- beam using data collected during the 1990 fixed target run of Fermilab experiment E706. E706 is a second generation fixed target experiment designed to measure direct-photon production in hadron–nucleus collisions. These data provide a clean test of perturbative QCD and serve as a valuable tool for probing hadronic structure.

The $\gamma\gamma$ decay mode of the η meson was studied using data from a highly segmented electromagnetic lead liquid argon sampling calorimeter. Results are presented for inclusive η production by π^- beams on both beryllium and copper targets. The η to π^0 production ratio and the nuclear dependence of the η production cross section are also reported. These results are for η's in the transverse momentum range 3.5 to 9 GeV/c and the center of mass rapidity range -0.75 to 0.75, and are the highest energy results ever obtained for inclusive η production using a π^- beam.

Table of Contents

List of Tables

List of Figures

Chapter 1 Introduction

1.1 Overview

This thesis presents results from data taken during the 1990-1991 fixed target data run of experiment E706 at Fermi National Accelerator Laboratory (FNAL). E706 is a second generation fixed target experiment designed to measure direct-photon production in hadron–hadron collisions. A "shakedown" or engineering run of the MWest spectrometer and of the Meson West beam line occurred during the 1987-1988 FNAL fixed target run. Results from that effort have recently been published [1]. The 1990-1991 fixed target run was the primary data run of this experiment and made use of what was learned during and after the 1987-1988 run in order to gather higher quality and much higher statistics data. Although the subject of this thesis is the production of η mesons, the design and operation of E706 were driven by the desire to study direct photons. This chapter will therefore also briefly discuss the primary physics motivation of E706 – direct-photon production.

1.2 Background

The present understanding of elementary particles is that quarks and leptons are the fundamental constituents from which all of matter is built. Particles which mediate the forces between these constituents are gauge bosons, such as the gluon and the photon. Subnuclear particles which experience the strong force are called hadrons. These hadrons (e.g. protons, neutrons, mesons,...) are composed of quarks and gluons. The strong force binds these protons and neutrons together to form atomic nuclei.

All known hadron species are combinations of more fundamental entities called quarks [2]. Five kinds or "flavors" of quark have been identified — the up(u), down(d), charm(c), strange(s), and bottom(b) — a sixth flavor called top(t) is believed to exist but has yet to be directly detected. Quarks have half a unit of spin and also carry electric charge equal to a precise fraction of an electron's charge (as shown in table 1.1).

Charge	**Quarks**		
$+2/3e$	u (up)	c (charm)	t (top)
$-1/3e$	d (down)	s (strange)	b (bottom)

Table 1.1 Classification of quarks by charge

Pauli's exclusion principle states that no two identical particles possessing half-integral spins (fermions) can simultaneously occupy the same state. This exclusion principle accounts elegantly for the configurations of electrons that determine an element's place on the periodic table. Consequently, it is reasonable to expect it to be a plausible guide for the valence quark constituents of hadrons as well. "Valence quarks" exist within hadrons unpaired with their anti-quark; in contrast, "sea quarks" are present only as quark-antiquark pairs. In order to reconcile the Pauli exclusion principle with the valence quark classification of hadrons, a new kind of charge called "color" was invented.

Each quark flavor carries one of three colors. Hadrons do not exhibit a color charge; the combination of the component quarks' colors must be color neutral. The observed color neutral combinations are mesons (consisting of a quark and an oppositely colored antiquark) or baryons (triplets consisting of one quark of each color). Colored states such as free quarks have not been observed.

Hadrons consist of specific combinations of valence quarks such that the sum of their electric charges is integral. For example, the electric charge of the quark and antiquark that constitute a meson have charges that add up to -1, 0, or +1. A proton is a baryon which consists of two valence u quarks and one valence d quark, for a total electric charge of +1. A neutron, on the other hand, consists of one valence u quark and two valence d quarks, which yields a total electric charge of 0.

1.3 Investigating Quantum Chromodynamics

Quantum Chromodynamics (QCD), was introduced to explain the strong interaction between colored partons. In QCD, partons refer to either quarks or gluons. Gluons are electrically neutral spin 1 particles which mediate the strong force in QCD. Gluons play a role analogous to that of photons in Quantum Electrodynamics (QED).

Cross sections for QCD processes are not presently exactly calculable. Rather, they are approximated by expansions in terms of the coupling constant. The coupling strength in QCD is given by α_s, which is, to leading log in Q^2: [3]

$$\alpha_s(Q^2) = \frac{12\pi}{(33 - 2n_f)log(Q^2/\Lambda^2)} \qquad 1.1$$

where Q^2 is a measure of the momentum transfer in the collision. Λ is a scale parameter required by the expansion, and n_f is the number of quark flavors accessible at the energy of the collision. If the expansion could be done to all orders of α_s, the result would be independent of the choice of Λ; however, because of the complexity of such a task, present experiments must choose a value which best fits the data. Equation 1.1 illustrates that as $Q^2 \rightarrow \infty$, $\alpha_s \rightarrow 0$. (This phenomenon is referred to as "asymptotic freedom.") Thus, the coupling between quarks diminishes as their interaction distance decreases or as

the momentum transfer increases. This means that at high momentum transfer, quark confinement inside of hadrons can be neglected. The constituents are essentially free and the hadron-hadron interaction may be calculated in terms of a parton-parton interaction. Even at $Q^2 \approx 2(GeV/c)^2$, α_s is relatively small and perturbative techniques can be applied for calculating cross sections. Because high p_T interactions can thus be treated perturbatively, it is useful to study such interactions in order to obtain quantitative comparisons between QCD and experiment.

Investigating the properties of QCD involves the study of parton interactions. These interactions can be represented pictorially by Feynman diagrams. Figure 1.1a depicts a typical parton interaction in which a quark and an anti-quark annihilate to form two gluons. Figure 1.1b shows quark-gluon scattering with the emission of a quark and a photon. This second diagram describes a process in which a photon is produced directly at the parton-parton scattering vertex. (Such photons are commonly referred to as "direct photons" since they come from the constituent interaction rather than from hadron decays.)

In studying QCD processes, one wishes to extract information from the observed particles about the underlying constituent interactions. The beam and the target hadrons are composite objects consisting of these constituent partons. The scattered partons undergo a process called "fragmentation" while emerging from the interaction. Fragmentation is the process by which partons evolve into observable hadrons [4].

Figures 1.1a and 1.1b are over-simplified indications of what occurs in an actual collision. It is not two quarks which collide but rather it is two hadrons. Each hadron supplies one parton to this interaction. The remaining spectator quarks in both the beam and target must also recombine into emerging

hadrons. What the experimenter measures is information about these products of fragmentation, not about the direct interaction of the two quarks. This is illustrated in Figure 1.1c and 1.1d. Extracting information about this underlying parton scattering process can be quite complicated.

There are two main advantages of using processes involving direct photons in order to study parton-parton interactions.

- The final state photon is color neutral and therefore does not undergo fragmentation. Thus the direct photon directly reflects the kinematics of the underlying interaction. The alternative is to detect the intermixed collection of quark and gluon jets emerging from the parton-parton interaction, where all of the particles resulting from the interaction must be reconstructed in order to properly estimate the underlying parton momenta. The direct photon also provides a straight-forward experimental signature by which to identify these high transverse momentum parton parton interactions.
- To first order in α_s, the coupling constant for the strong interaction, there are only two processes which contribute to the production of direct-photons – quark/anti-quark annihilation and quark/gluon Compton scattering processes. These diagrams are shown in Figure 1.2. In contrast to direct-photon physics, there are many more diagrams for the 3 quark species which contribute to jet-jet production [3]. Extracting information about particular subsets of this many diagrams is obviously very challenging.

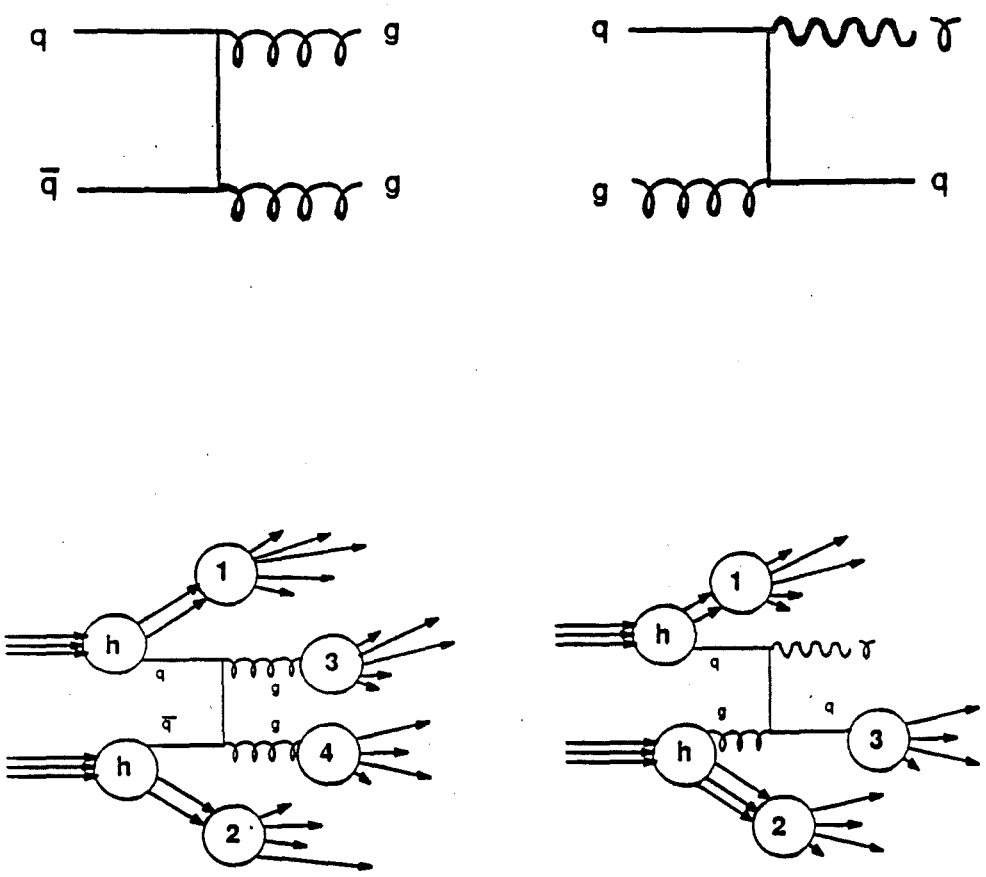

Figure 1.1 Simple Feynman diagrams shown with and without hadronic structure.

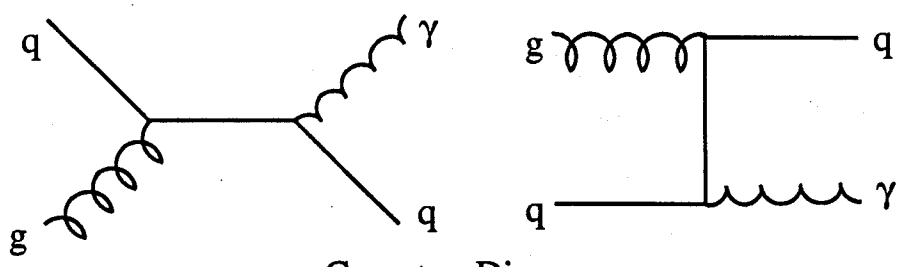

Compton Diagrams

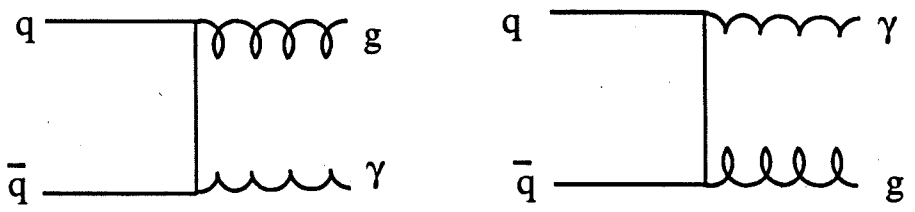

Annihilation Diagrams

Figure 1.2 Feynman diagrams of lowest order direct-photon processes.

1.4 Cross Section Calculation

Consider the general reaction $A + B \rightarrow C + X$. Here, A and B are the interacting hadrons. C is a specific product of the reaction, and X is everything else which is produced. The invariant inclusive cross section for this process can be expressed in terms of the contributing subprocesses as follows:

$$E_C \frac{d\sigma}{d^3 p_C}(AB \rightarrow CX) = \sum_{abcd} \int dx_a dx_b dz_c G_{a/A}(x_a, Q^2) G_{b/B}(x_b, Q^2) \times D_{C/c}(z_c, Q^2) \frac{\hat{s}}{z_c^2 \pi} \frac{d\sigma}{d\hat{t}}(ab \rightarrow cd) \delta(\hat{s} + \hat{t} + \hat{u}) \quad 1.2$$

In this equation, the sum is over the constituent partons a and b of the original hadrons A and B, and over all possible products c and d which could result from the interaction. x_i is the fraction of the momentum of hadron I that is carried by parton i. $G_{i/I}$ is the probability that parton i within hadron I has a momentum fraction x_i, when probed at the specified Q^2 value. The parton point like scattering cross section is represented by the term $d\sigma/d\hat{t}$. The "fragmentation function" $D_{I/i}$ is the probability that a parton i will hadronize to produce the particle I with a fraction z_i of the original parton momentum.

The variables $\hat{s}, \hat{t}$, and $\hat{u}$ are the Mandelstam variables for the pointlike scattering. They are given by:

$$\hat{s} = (p_a + p_b)^2 \quad 1.3$$

$$\hat{t} = (p_a - p_c)^2 \quad 1.4$$

$$\hat{u} = (p_a - p_d)^2 \quad 1.5$$

where p_i is the four vector momentum of parton i. The Q^2 dependence of the parton distribution functions $G_{i/I}$ and the fragmentation functions $D_{I/i}$ is

referred to as "scaling violation." Simply stated, the parton distribution that a gluon "sees" depends on the amount of momentum it is transferring.

It is instructive to look at the specific example of the direct–photon process. Recall that photons emerge from the interaction without hadronization. Consequently, one can study the product of a parton-parton interaction directly without the necessity of reconstructing a jet of particles. For direct–photon production, equation 1.2 can be rewritten as: [5]

$$E_\gamma \frac{d\sigma}{d^3p_\gamma}(AB \to \gamma X) = \sum_{abcd} \int dx_a dx_b G_{a/A}(x_a, Q^2) G_{b/B}(x_b, Q^2) \frac{\hat{s}}{\pi}\frac{d\sigma}{d\hat{t}}(ab \to \gamma d)\delta(\hat{s}+\hat{t}+\hat{u}) \quad 1.6$$

To lowest order, the sum is over two diagrams with cross sections given by:

$$\frac{d\sigma}{d\hat{t}}(\bar{q}q \to g\gamma) = \frac{8\pi\alpha\alpha_s}{9\hat{s}^2} {e_q}^2 \frac{\hat{u}^2+\hat{t}^2}{\hat{u}\hat{t}} \quad 1.7$$

$$\frac{d\sigma}{d\hat{t}}(qg \to q\gamma) = \frac{-\pi\alpha\alpha_s}{3\hat{s}^2} {e_q}^2 \frac{\hat{u}^2+\hat{s}^2}{\hat{u}\hat{s}} \quad 1.8$$

Although direct photons seem like an ideal probe for QCD physics, they do have an important limitation. Direct photons are produced at a low rate relative to jet production. The production is suppressed by approximately α/α_s for each of the diagrams in which a photon replaces a gluon. Hence, in order to study this class of events, one must either record large quantities of data, most of which will be rejected in the subsequent analysis, or else implement an experimental trigger which preferentially selects this type of physics.

1.5 Motivation for the Study of Neutral Mesons

π^0 and η decays represent the major sources of background to the direct-photon signal. Since the primary goal of E706 is to measure the inclusive direct-photon cross section, these processes must be studied to understand the backgrounds to that signal. There are, however, other reasons to study high p_T neutral meson production as well. While the study of direct photons yields information about the intrinsic QCD processes at large momentum transfer, high p_T meson production can also yield insights into QCD processes along with information on the fragmentation function, $D_{C/c}$, of partons. Such fragmentation functions are not calculable by perturbative QCD and thus must be determined experimentally. The experimental cross sections are sensitive to these fragmentation functions, and therefore provide a means of measuring such functions.

The η to π^0 production ratio can also be used to study the relative importance of gluons and quarks (both valence and sea) in the production of high p_T neutral mesons. The π^0 and η valence quark content can be approximated as: [6]

$$\pi^0 = \frac{1}{\sqrt{2}}(u\bar{u} + d\bar{d}) \qquad 1.9$$

$$\eta = \frac{1}{\sqrt{6}}(u\bar{u} + d\bar{d} - 2s\bar{s}) \qquad 1.10$$

where u, d, and s refer to the up, down and strange quarks, respectively. Since the η has a substantial strange valence quark component and there are no strange valence quarks component in the beam pions, or in the protons or neutrons in the target, any contribution from valence-quark fragmentation to high-p_T neutral meson production could result in suppression of η relative to π^0 production.

Based on HERWIG [7], the Monte Carlo event generation package which was used to simulate high p_T η production, the prominent sources of η's in high p_T interactions are valence quarks, sea quarks and gluon fragmentations, and pair creation by gluons. Although there are slight differences between the masses of the up, down and strange quarks, one expects that the population of u, d, and s sea quarks is similar in this energy range. Neglecting the π^0/η mass difference, there is no reason to expect a gluon to preferentially fragment into any one of these three quark species over another. Thus, if the primary source of high p_T η and π^0 production is the fragmentation of partons, one might expect the η to π^0 production ratio to be close to unity.

Consequently, from the η/π^0 ratio, one can investigate the relative importance of gluons and valence quarks in the production of high p_T neutral mesons. A ratio near unity would indicate that the process of pair creation and sea quark and gluon fragmentation play a more dominant role in the production of these neutral mesons than do the valence quarks. The smaller this ratio becomes, the larger is the implied role of the valence quarks in production.

The measurement of the η cross section also serves as a test of current perturbative QCD calculations. The first next-to-leading-log calculations of high p_T η production has recently been provided by M. Greco *et al.* [8]. Their initial interest in this subject stemmed from their desire to understand the various backgrounds to the process $Higgs \rightarrow \gamma\gamma$ in the energy domain of the proposed Large Hadron Collider (LHC) at CERN. Their theoretical models of η production are based entirely on fits to HERWIG Monte Carlo events at very large values of $\sqrt{s}$. The η cross sections measured in E706 can be used to test their calculation in a different kinematic range and thus serve as input to constrain their theoretical model.

1.5.1 A-Dependence Measurement

Those experiments that employ nuclear targets can provide insight on the rescattering of hadrons or partons and the time development of these states. The dependence of secondary particle production from a nuclear target is generally parametrized in the form A^{α}.

Previous data indicate that at p_T's below about 1 GeV/c, the A-dependence of the cross section can be approximated by $A^{2/3}$. Here nuclear shadowing is playing an important role and the cross sections are proportional to the cross-sectional areas of the nuclei. At higher p_T's, point-like interactions between the constituents of the hadrons start to dominate. The produced partons can scatter many times leading to a dependence that is related to the number of rescatters. As a consequence, for purely hard scattering, one expects α to be greater than 1 and depend on the degree of rescattering of quarks and gluons.

1.6 Previous Experiments

Over the past 15 years, a number of experiments have studied the production of η mesons at high p_T. These experiments vary widely in terms of the type of detectors used and the kinematic regions which were investigated. This section will briefly describe some of these experiments. Their measurements will be compared with the results of this analysis in Chapter 8.

1.6.1 Fermilab

Four experiments which have published measurements of high p_T production of η and π^0 mesons are E706 [1], CDF [9], E111 [10], and E629 [11]. E111 was run in the M2 beamline using a hydrogen target and a variety of beam particle types and momenta. They presented results for $\pi^{\pm}$, K, and p beams at 100, 200, and 300 GeV/c incident momenta. E629 measured η and π^0 production

on carbon, aluminum and beryllium targets for 200 GeV/c π^+ and p beams. E706 published data from its engineering run for π^- and p on beryllium at 500 GeV/c. We measured cross sections for η's, π^0's, and direct photons. CDF recently published its results from $\bar{p}p$ collisions at $\sqrt{s} = 1600$ GeV recorded during the 1989 collider run.

1.6.2 CERN

Within the past 5 years, several CERN experiments have published results on high p_T neutral meson production. Most notable among them are WA70 [12] and UA6 [13]. WA70 used $\pi^{\pm}$ and p beams at 280 GeV/c on a hydrogen target to study the production of π^0 and η mesons as well as direct photons. UA6 used a hydrogen jet in the SPS ring as their target to study the production of the η and π^0 mesons at a $\sqrt{s} = 24.3$ GeV.

Prior to WA70, and UA6, three groups pioneered the study of direct-photon production at the Intersecting Storage Ring (ISR) at CERN. These groups were AFS [14] , CCRS [15], and R806 [16]. The CCRS (CERN Columbia Rockefeller Saclay) collaboration measured the production of π^0 and η mesons at 90 degrees for $\sqrt{s}$ between 23.5 and 62.4 GeV. R806 and AFS also measured the production of the π^0's and η's at $\sqrt{s}$ of ≈ 53 GeV/c.

Table 1.2 provides a summary of the principal characteristics of these experiments.

1.7 Thesis Overview

The remaining sections of this thesis will discuss in detail the E706 experiment including the apparatus, the data acquisition and data reconstruction techniques, the Monte Carlo model employed and the analysis procedures used

Exp.	$\sqrt{s}$ (GeV)	p_T Range	y	Detector
AFS	53	2.→ 6.	-.4 → .4	Uranium Scint.
CCRS	62	2.→ 4.5	90 Deg.	Pb Glass
R806	52.7, 62.4	3 → 8	0	Liquid Argon
E629	20	2. → 5.	-.5 → .1	Liquid Argon
E706	31	3.5 → 10	-.7 → .7	Liquid Argon
WA70	22.9	3. → 7.	-1. → 1.	Pb,Liquid Scint
UA6	24.3	2.5 → 5.	-.7 → .7	Pb, Prop tubes
CDF	1600	15.→ 20.	-1. → 1.	Pb,Scint

Table 1.2 Experiments Measuring high p_T π^0 and η Cross Sections

to determine the high p_T η cross sections. Comparisons to other experiments and to phenomenological calculations will also be presented.

Chapter 2 The Experimental Apparatus

2.1 The Spectrometer

The MWest spectrometer can be divided into five general subsystems based on functionality; the beam transport system, the trigger system, the charged particle tracking system, the calorimetry, and the muon identifier. Each of these systems was optimized to meet the specific goals of the experiment. The relevant subsystems will be described in this chapter.

Figure 2.1 shows the physical layout of the various devices in the MWest experimental hall. Included in this diagram is the experimental apparatus for E672, which ran concurrently with E706. The muon identifier and the associated E672 dimuon trigger had no direct relevance to this analysis; hence that part of the spectrometer will not be discussed. The sections describing the liquid argon calorimeter (LAC) are expanded since Rochester had primary responsibility for that device, and since the author played key roles in its construction, readout and analysis.

The hardware is presented in the order in which an incident beam particle would encounter each of the different devices. The coordinate system adopted by the experiment is a right handed system, with its origin near the target. The Z-axis is aligned with the nominal incident beam direction, the Y-axis is vertical, and the X-axis is horizontal. Coordinates R and ϕ will be used to express nominal positions within the electromagnetic calorimeter which is uncorrected for alignment.

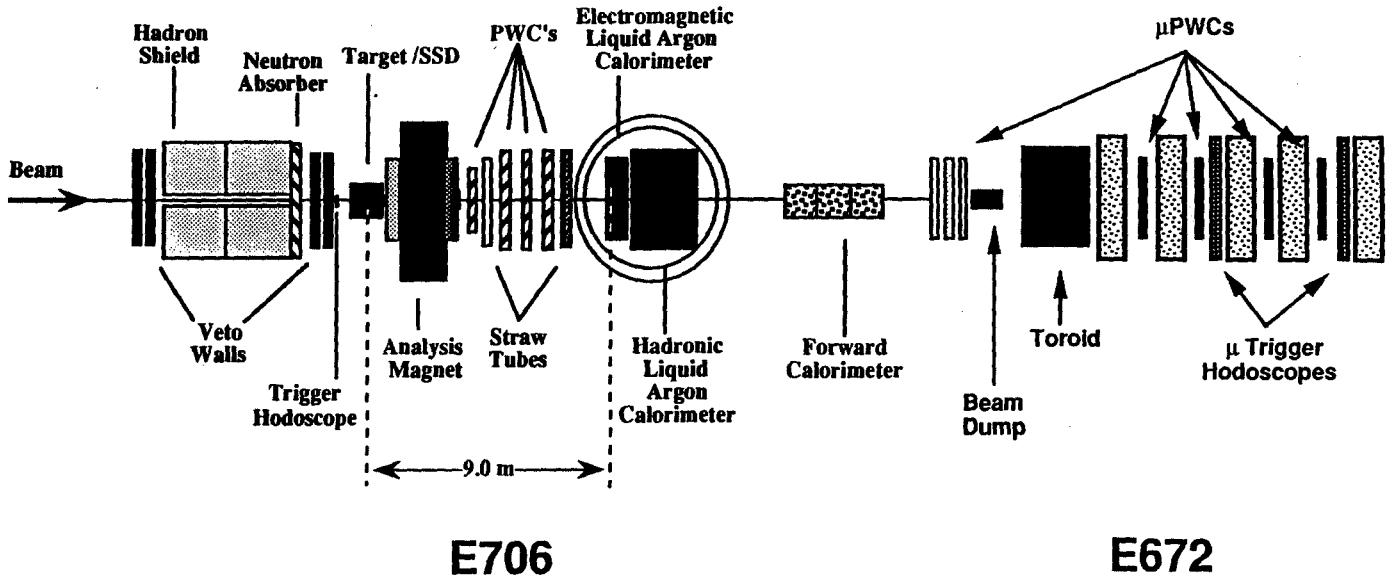

Figure 2.1 The physical layout of the MWest spectrometer in the detector hall.

2.2 The Beam Transport and Trigger System

2.2.1 Beamline and Cerenkov Counter

E706 was located in the Fermilab Meson West beamline. This above ground beamline was built specifically for the experiment. The beamline extended north from the existing Meson Detector Building to the MW9 experimental hall. The beamline was designed to transport positively and negatively charged particles with a maximum momentum of 1 TeV/c.

The Tevatron provided a beam of 800 GeV/c protons to the switchyard. At the switchyard, the beam was split and steered into Fermilab's three major beam areas: Meson, Proton, and Neutrino. The meson beamline had its own switchyard to subdivide the beam further among the various experiments in this area. The primary target for E706 was located inside the Meson Detector Building. This target was a 1.14 interaction length beryllium block, 46.5 cm in length and 2.22 cm diameter, in which the secondary particles were produced. Beam intensities on the primary target were typically 5-6 $\times 10^{12}$ protons per spill for negative secondary beam and 2 $\times 10^{12}$ protons per spill for positive secondary beam during high intensity running periods. The 1990 data run employed negative secondary beam exclusively. The 1991 run was split into three components, positive and negative secondary beam (protons and pions), and primary protons (See table 2.1 for the amount of data taken for each set of beam conditions.) The only data used in this analysis were the 1990 π^- sample.

The beam had a 19.1 ns bucket structure from the characteristic radio frequency (RF) of the Tevatron. The beam was extracted during 23 second spills. The spills were separated by a 35 second period during which the beam for the upcoming spill was being accelerated.

Year	Momentum (GeV/c)	Species	Target	Events	Sensitivity
1990	520	π^-	Be	30×10^6	8.6 ev/pb
			Cu		1.4 ev/pb
1991	800	P	Be	23×10^6	7.3 ev/pb
			Cu		1.8 ev/pb
			H		1.5 ev/pb
	530	P,π^+	Be	14×10^6	6.4 ev/pb
			Cu		1.6 ev/pb
			H		1.3 ev/pb
	530	π^-	Be	4×10^6	1.4 ev/pb
			Cu		.3 ev/pb
			H		.3 ev/pb

Table 2.1 The 1990 and 1991 run summary for E706.

The beamline parameters were adjusted to transport a 530 GeV/c secondary beam. This simplified the comparison between the data from primary protons and pions, since the average momentum of the valence quarks would be similar for 800 GeV/c proton and the 530 GeV/c pion. In practice, the actual beam momentum for the 1990 data run was 520 GeV/c.

The secondary beam used for E706 was not a pure pion beam; it also contained a non-negligible component of kaons and a very small percentage of antiprotons. A Cerenkov detector was installed to "tag" those particles. The Cerenkov detector was positioned in a long parallel section of the beamline in where the beam had minimal angular divergence.

The angle of emission of Cerenkov radiation is related to the velocity of the incident particle and the index of refraction of the medium it is in. By

adjusting the pressure, the index of refraction changes. Since the momentum of the beam was fixed by the beamline optics, changing the pressure inside the counter is equivalent to selecting a specific mass for a detector positioned at a fixed opening angle.

The Cerenkov detector, as shown in figure 2.2a, was 42.1 meters long and had a radius of 24.4 cm. A spherical, high quality mirror was placed at the downstream end of the counter to reflect the photons generated by the passage of beam particles and to effectively double the path length and hence the opening angle or separation of the light coming from the different particle types. Near the upstream end of the Cerenkov counter, three rings of six phototubes were used to collect the radiated photons. The geometry of the rings was chosen such that at the correct operating pressure, the three major components of the beam could be tagged simultaneously. Helium gas, at a pressure between 4-8 psia was used as the radiator.

A Cerenkov pressure curve, shown in figure 2.2b, illustrates the detector's ability to distinguish particle types. Pressure curves were generated by varying the gas pressure inside the device which sweeps the Cerenkov light across the face of the counters. A change in gas pressure resulted in a change in the opening angle of the Cerenkov light cone, and thus the position at which the light struck the optics at the instrumented upstream end of the counter. The number of counts observed in each of the rings was measured as a function of pressure. By plotting the number of counts collected in each ring as a function of gas pressure, one can measure the counter's efficiency, and determine the pressure which optimizes the relative fraction of particles tagged simultaneously in each of the three rings of photon detectors.

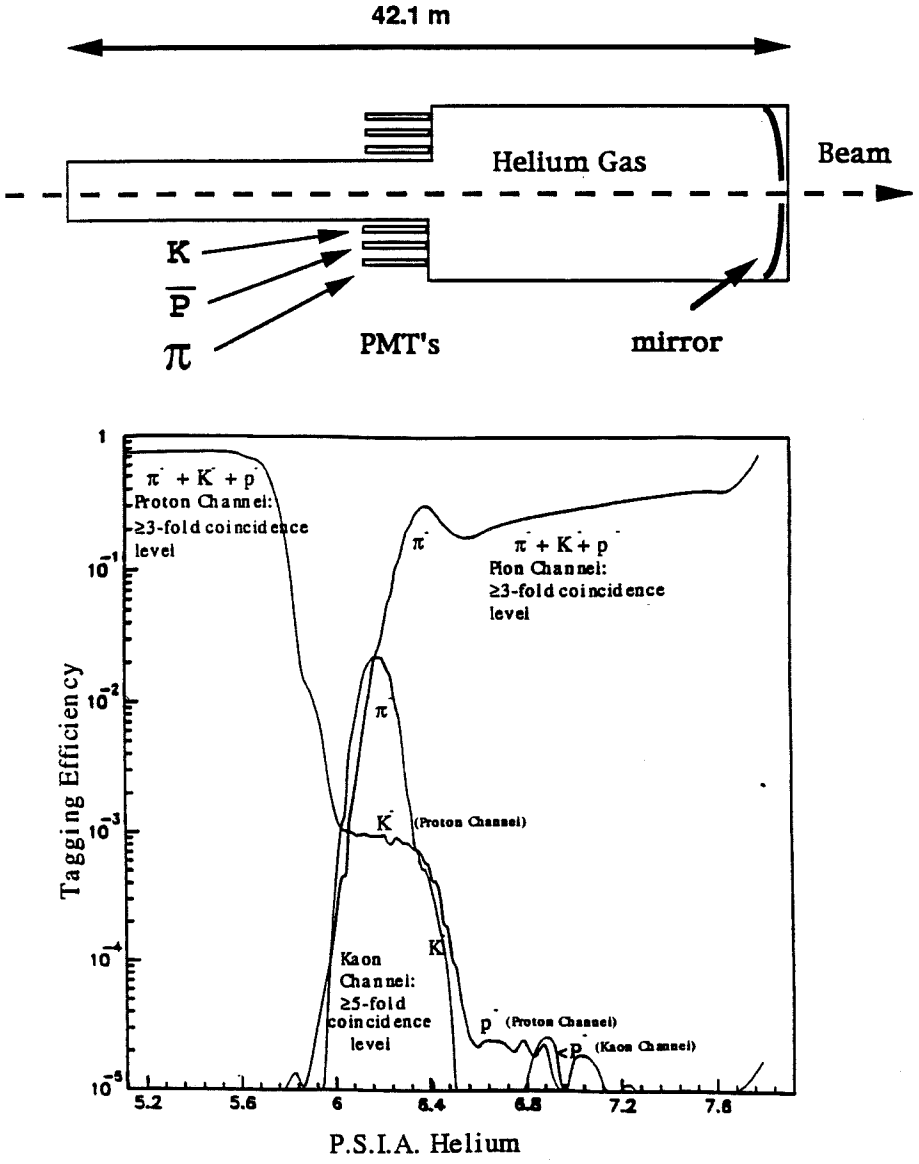

Figure 2.2 The Cerenkov detector (a) and an associated pressure curve (b) taken with this device for 520 GeV/c π^- data. The contribution from the individual beam particle types is indicated.

A series of pressure curves were taken periodically throughout the run. Such curves indicate which pressure maximized the fraction of particles tagged simultaneously in each of the different rings. The pressure curves were also used to estimate the relative fraction of protons, pions, and kaons in the beam. Since the counter was very sensitive to the beam energy and beam position, a pressure curve was taken every time the experiment changed beam energies, or immediately following a significant change in the beam steering. The results of this curve were used to optimize the performance of the counter for that particular set of run conditions.

At this point in time, the analysis of the Cerenkov data is incomplete. The exact fraction of minority particles in the beam has not yet been determined. However, the relative fractions should be close to what was observed during the 1988 data run [1]. Those numbers are presented in table 2.2

Species	Beam
π^-	97.0%
K^-	2.9%
$\overline{p}$	0.1%

Table 2.2 Beam content for 500 GeV π^- data for the 1988 run.

2.2.2 Hadron Shield and Veto Walls

At the end of the beamline just inside the MW9 hall was a hadron shield 4.3 m wide, 4.7 m long, and 3.7 m high. The purpose of this huge stack of steel was to absorb beam halo, those particles traveling parallel with the beam. The shield had a hole for the beam to pass through, and a removable vertical slab so that the beam could be scanned vertically across a portion of the LAC during

calibration. Just downstream of the hadron shield was a tank of distilled water used to absorb neutrons.

To tag particles that traversed the hadron shield, a series of 3 veto walls were constructed; one upstream of the hadron shield and two downstream. Each wall contained a number of large scintillator counters attached to phototubes. Muons that were not swept clear of the spectrometer by the upstream "spoiler" magnets were tagged by these veto walls.

2.2.3 Hodoscope

A beam hodoscope was used to identify beam particles incident on the target. It consisted of three planes of tiny scintillator paddles. The paddles ranged in width from 1 to 5 millimeters. The 12 paddles that comprised each of the 3 planes (labeled X, Y, and U) covered a total area of 2x2 centimeters. The hodoscope had the advantage over the single paddle used in the 1988 run because the phototube rate in each hodoscope element was less likely to "sag" (saturate) as a result of high beam currents than the single broad counter. The hodoscope was an integral piece of the trigger system. Not only did it "shadow" the target and alert the spectrometer to a potential interaction, the hodoscope also discerned if there were multiple beam particles in a single accelerator RF bucket.

2.2.4 Interaction Counters

There were four scintillation counters employed to detect an interaction in the target vicinity. Two counters were located just downstream of the silicon tracking system on the upstream side of the analysis magnet and flat against the mirror plates. Two additional counters were mounted on the downstream mirror plate. These counters were not sensitive to the non-interacting beam due to holes cut into the counters.

2.3 The Tracking System

In order to study the hadronic jets associated with direct-photon production, E706 employed a charged particle tracking system, including a precision silicon system to locate both primary and secondary vertices within the target. (The term vertex refers to the point of origin of a group of particles. The point where the incident beam interacts with the target is referred to as the primary vertex. Secondary vertices can arise from either the decay or interaction of particles produced at the primary vertex.) The vertex position was important because the experiment simultaneously employed two different target materials. Determining the Z position, and hence in which target the interaction occurred, was thus critical for doing nuclear dependence measurements.

The tracking system also proved to be essential in the rather challenging job of determining the LAC energy scale. Zero Mass Pairs (ZMP's), photons which converted into e^+e^- pairs, were identified via the tracking system and provided valuable insight into the behavior of electromagnetic shower development in the LAC. Energy scale determination will be discussed in detail in the analysis chapter.

The tracking system consisted of Silicon Strip Detectors (SSDs) for upstream tracking, a large aperture analyzing dipole magnet, and a downstream tracking system comprised of both Proportional Wire Chambers (PWCs) and Straw Tube Drift Chambers (STRAWS).

2.3.1 Silicon Strip Detectors

SSD's measure the position of charged particle which pass through them by means of collecting signals induced on strips etched onto silicon wafers. The E706 SSD system [17], as shown in Fig. 2.3, consisted of 16 separate planes.

These planes were arranged in pairs consisting of one whose strips were oriented along the X axis and one whose strips were oriented along the Y axis. The SSD system surrounded the target region. Three pairs of silicon planes, 3 cm on a side with a 50 μm pitch, were placed upstream of the target. These planes were used to record beam track information. The remaining 5 pairs of planes, 5 cm on a side, were placed downstream of the target and used for track finding and vertex reconstruction. The first XY pair downstream of the target had a region of 25 μm pitch. The other downstream SSD planes had a 50 μm pitch.

The SSD's and their front-end electronics were housed in a aluminum box to physically protect them and to shield them from electronic noise. The target itself was also housed inside this box. The angular resolution of the SSD system was 0.1 milliradians. The vertex position resolution was 10 μm in X and Y, and 350 μm in Z. Fully instrumented, the SSD's detectors contained in excess of 10,000 channels, of which 8912 were read out. The uninstrumented channels corresponded to the peripheral channels on the upstream wafers and to strips outside of the angular coverage of the last downstream wafer.

During the 1990 data run, the target consisted of several pieces of beryllium and two thin upstream pieces of copper. For the 1991 run, a liquid hydrogen target was added The exact target specifications for the 1990 configuration are given in table 2.3.

Material	Z Position	Diameter	Thickness
Cu	-15.52 cm	2.0 cm	0.08 cm
Cu	-15.19 cm	2.0 cm	0.08 cm
Be	-12.79 cm	2.0 cm	3.74 cm
Be	-09.36 cm	2.0 cm	1.12 cm

Table 2.3 Dimensions of the 1990 experimental target.

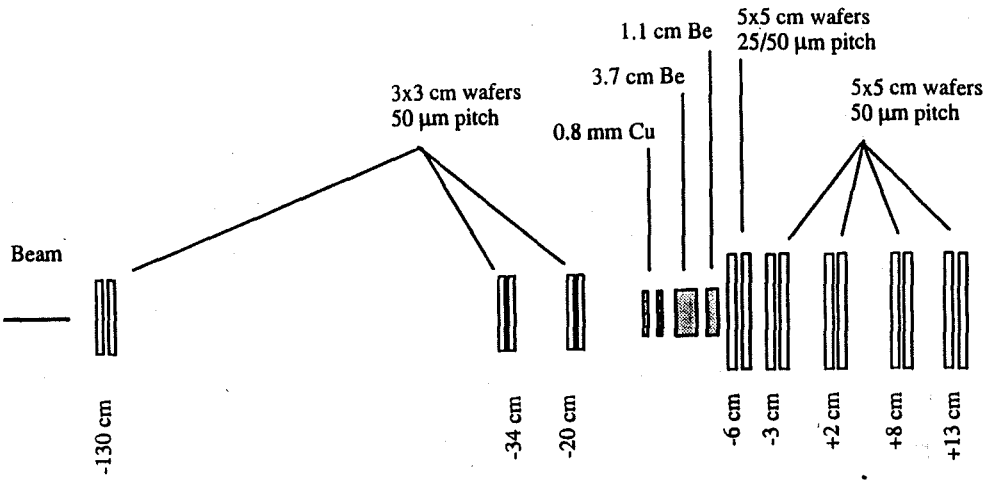

Figure 2.3 The SSD system and target region.

2.3.2 Analysis Magnet

A 350 ton rectangular conventional electromagnet was employed as the analysis magnet. The center of the magnetic field was located 198 cm downstream of the origin. The magnet aperture was filled with a bag containing helium gas to allow particles to pass through with a minimum probability of interacting. The magnetic field was adjusted to impart a 450 MeV/c transverse momentum impulse to charged particles. The change in direction that this transverse kick generated was used to measure particle momenta. Mirror plates were installed to reduce magnetic fringe field interference with the performance of the interaction counter phototubes, as well as to simplify the job of track reconstruction.

2.3.3 Proportional Wire Chambers

The primary tracking detectors located downstream of the magnet were 16 planes of Proportional Wire Chambers (PWC's) [18]. These planes were grouped into 4 modules, commonly referred to in ascending Z as PWC1, PWC2, PWC3, and PWC4. Each module consisted of an X plane, a Y plane, a U plane (rotated +37 degrees) and a V plane (rotated by -53 degrees). All of the planes were roughly 2 meters by 2 meters and had an anode wire spacing of 2.5 mm. The cathodes were constructed of graphite coated mylar. The gaseous ionization medium inside these chambers was a mixture of 18% isobutane, 1.1% isopropyl alcohol, 0.1% freon, and 79.7% argon. The argon provided most of the electrons produced from ionization.

2.3.4 Straw Tube Drift Chambers

The straw tube drift chambers (STRAWS) were constructed and installed between the 1988 and 1990 data runs to aid in linking the upstream and

downstream tracks at the center of the magnet as well as to improve the precision of the momentum determination [19]. Two straw tube drift chambers were built. One chamber was hung between PWC1 and PWC2 and the other was hung on the upstream edge of the LAC support structure, just downstream of PWC4. The straw tubes had an angular resolution of about .06 mrad.

Each straw chamber consisted of eight planes, four oriented along the X axis and four along the Y axis. Each plane was offset from the previous one by one quarter of the diameter of a tube. The tubes were made of aluminized mylar. Twenty micron diameter gold plated tungsten wires were threaded through each of the tubes and centered. The STRAWS were filled with a standard mixture of argon ethane gas, bubbled through ethyl alcohol at 0 degrees celsius just above atmospheric pressure.

2.4 Calorimetry

The E706 spectrometer contained three specialized calorimeters:

- An Electromagnetic Liquid Argon Calorimeter (EMLAC)
- A Hadronic Liquid Argon Calorimeter (HALAC)
- A Forward Scintillator Calorimeter (FCAL).

The EMLAC and HALAC are referred to collectively as the "LAC".

A sophisticated electromagnetic spectrometer which had fine position resolution was necessary in order for E706 to carry out a precise measurement of direct-photon production. An overview of the salient features of the LAC will be given here. However, a detailed discussion of the design considerations of the EMLAC can be found elsewhere [20]. The EMLAC was a sampling device; only a fraction of the energy deposited by an incident particle ionized the liquid argon.

The remaining energy was deposited inside a variety of absorber materials and was unavailable to contribute to the collected signal. This arrangement, albeit far from ideal for a precise energy measurement, provided the most practical and affordable method of achieving fine granularity, high response rates, and good energy resolution, as well as a reasonable "foot print" in the experimental hall.

2.4.1 Structure – The Gantry and Cryostat

The EMLAC and HALAC were suspended from a gantry, a mobile support structure, shown in Fig 2.4, used to move the detectors traverse the beam for calibration and to position the detectors over a "pit" to either release or pickup the outer cryostat. The pit was a deep hole at one end of the travel of the gantry which acted as a staging area for the cryostat when it was not attached to the cap. The cap for the cryostat which enclosed both calorimeters was an integral part of the gantry.

The cryostat cap was a cylinder built from mild steel that had a diameter of 17 feet and a height of 6 feet. Eight rods projected thru the top of the cap and connected to steel box beams in the gantry. These eight rods provided the sole support for the electromagnetic and hadron calorimeters. The cap featured 30 access ports distributed around its circumference to allow for connections to both calorimeters. There were also additional ports on top to permit further access to these devices. These ports carried the charge signals and high voltage feeds as well as provided access to thermocouples and strain gauge monitors, heaters and various other necessary attachments.

The lower half of the cryostat was made from a stainless steel cylinder, 17 feet in diameter and 21 feet deep with a rounded bottom. A 5 cm diameter port made of 1.6 mm thick stainless steel was located at the point where the non-interacting beam struck the cryostat. This beam window reduced the amount of

material in the path of the beam and therefore, reduced the amount of scatter into the calorimeters.

The gantry, an A frame structure made of steel "I" beams transmitted the weight of the calorimeters to a set of Hillman rollers. These rollers allowed the gantry to move transverse to the beam via a motorized drive screw. The rate of this movement was approximately 6 inches per minute at full speed.

In operation, the two detectors were immersed in approximately 17,000 gallons of liquid argon. This argon was kept cold by boiling liquid nitrogen in refrigeration coils placed just above the liquid level. These refrigeration coils maintained a constant temperature in the LAC by manipulating the outlet pressure of the nitrogen. The inside of the cryostat was kept thermally isolated from the outside world by a complicated layering scheme of various insulating and fireproofing materials.

2.4.2 Filler Vessels

In order to get an accurate measure of a photon's energy, the shower of ionized electrons in the liquid argon should start in a region in which the detector was sensitive. Due to the size of the calorimeter, it would have been nearly impossible to build a thin wall cryostat with a flat upstream face. Yet without such a geometry, the EMLAC could not be positioned up against the dewar wall. It was necessary to build a low density "filler vessel" positioned between the upstream wall of the cryostat and the EMLAC to displace liquid argon from the uninstrumented region of the cryostat. The filler vessel reduced showering before the EMLAC where electrons could be collected and read out. The filler vessel was made of Rohacell foam coated with fiberglass and epoxy. This composite was then encased in a 1.6 thick stainless steel skin which provided structural

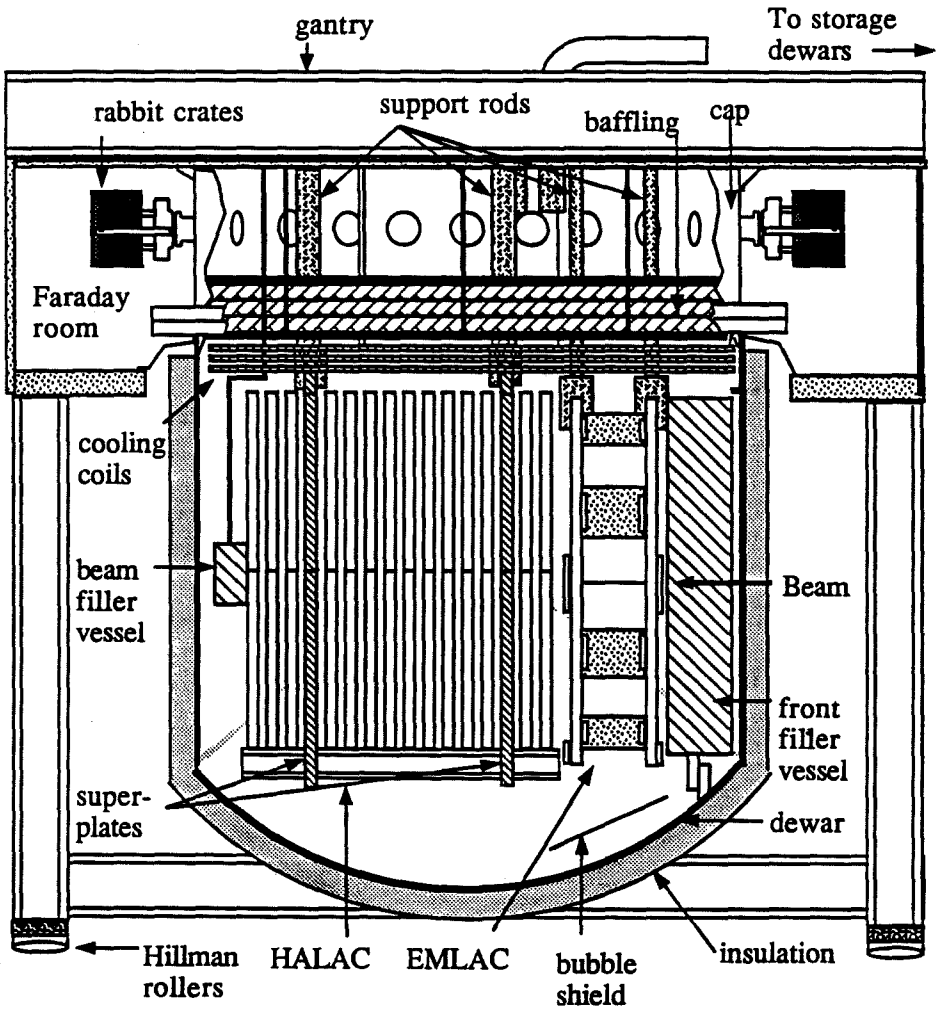

Figure 2.4 A side view of the LAC gantry and cryostat.

rigidity. The filler vessel was bolted to the inside of the cryostat to prevent it from floating about.

Along the same lines, a "beam filler vessel" was also introduced to further reduce beam scatter into the calorimeters. This truncated cone beam tube was placed within the calorimeters collinear with the beam. This beam filler vessel extended from the downstream face of the front filler vessel to the downstream wall of the cryostat. This tube was made of stainless steel which was sealed from the surrounding argon. Due to the pressure of the liquid argon on this tube, it was filled with gaseous helium just over atmospheric pressure rather than evacuated.

2.4.3 Faraday Room

The entire cap was surrounded by a Faraday room, which shielded the electronics from external noise. Most of the readout electronics were mounted directly on the cap. These ports channeled the signal from inside to the outside of the cryostat while maintaining argon purity. Great care was taken to isolate the Faraday room from the outside world. Transformers isolated the power. Signals entering or leaving this room were isolated either optically or, for fast logic trigger pulses, with pulse transformers.

2.4.4 Argon Purity

The purity of the argon was critical to the performance of the LAC. Any impurity in the argon which had an affinity for electrons, for example; oxygen would degrade the signal since electrons captured by an impurity would not contribute to the final energy measurement. Argon was chosen because it is a noble gas and thus chemically inert. Argon is also relatively abundant. Its phase change from liquid to gas occurs at 88K at atmospheric pressure. This

is very close to the temperature at which liquid nitrogen undergoes the liquid to gas phase transition. Thus liquid nitrogen serves as a relatively inexpensive refrigerant. Oxygen on the other hand is a particularly worrisome impurity. Its -2 valence gives it a high affinity for electrons, and its abundance in the atmosphere means that great care must be taken during all phases of argon handling to insure its purity.

The argon inside the cryostat was replaced in early 1990, just prior to the 1990 data run. This was done to remove any contaminants that might have polluted the argon during the previous 2 years. Removing the liquid argon was by no means a trivial process. The majority of the estimated 17,000 gallons of liquid argon was removed using a cryogenic pump. However, this technique could no longer be employed once the liquid level fell much below the pump-out port, and the remaining liquid was transferred in gaseous form instead.

The purity of the new argon was tested before it was transferred into the cryostat. A sample of argon was carefully drawn off the truck and condensed inside a test cell. This test cell housed a capacitor with a 2 mm gap – a mock LAC. A Ruthenium Beta (Ru 106) source was mounted on one of the plates which ionized the liquid argon within the charge collection gap. The amount of charge collected was measured as a function of applied voltage. The resultant curve was then fit with a function used to relate charge collection to equivalent oxygen contamination. No argon shipments which contained impurities of greater than 0.5 ppm of oxygen were accepted.

2.4.5 Electromagnetic Calorimeter

The electromagnetic calorimeter, the most upstream of the three calorimeters was located approximately 9 meters downstream of the target. The structure of the EMLAC is shown in Fig. 2.5. The EMLAC was cylindrical in shape,

with its axis along the beamline. It had a diameter of 320 cm. There is a 40 cm diameter hole, centered on the beam axis in the calorimeter. This hole was filled with a beam filler vessel to minimize the interactions in the beam region. This left an active region from approximately 20 cm to 160 cm in radius.

The EMLAC was divided into 4 equivalent quadrants. Each quadrant was composed of 33 cells along the Z axis. Each cell, as shown in Fig. 2.6, consisted of the following: an R board, a .078 inch liquid argon gap, a 0.082 inch thick lead sheet, another liquid argon gap and a ϕ board. The R and ϕ board were 1/16 inch thick octant sized double sided copper clad G-10 sheets. The copper on each sheet was scribed on both sides to form electrically isolated strips. (G-10 is a form of epoxy fiberglass. It is used extensively in the construction of the LAC. This particular grade was chosen because of the absence of a fire retardant material found to contaminate liquid argon.) Besides the production simplifications, the octant split of the R boards provided advantages in the matching of showers detected on the R and ϕ boards.

The R boards were segmented into arcs of concentric circles of increasing radius while the ϕ boards were segmented radially. The width of the R-strips on successive R boards were adjusted such that a particle originating in the target would pass through the same sequential R-strip in each successive cell. The lead plate in each cell served a dual role; it acted as an absorber and as a high voltage cathode.

The ϕ boards were divided into two views an inner ϕ and an outer ϕ. The outer ϕ view had twice as many strips as did the inner view. If a single strip size had been used for a ϕ board, the strips would have been either too wide at the outer edge, or so narrow at the inner edge that it would be difficult if not impossible to cable properly. The inner/outer ϕ boundary occurred at a radius

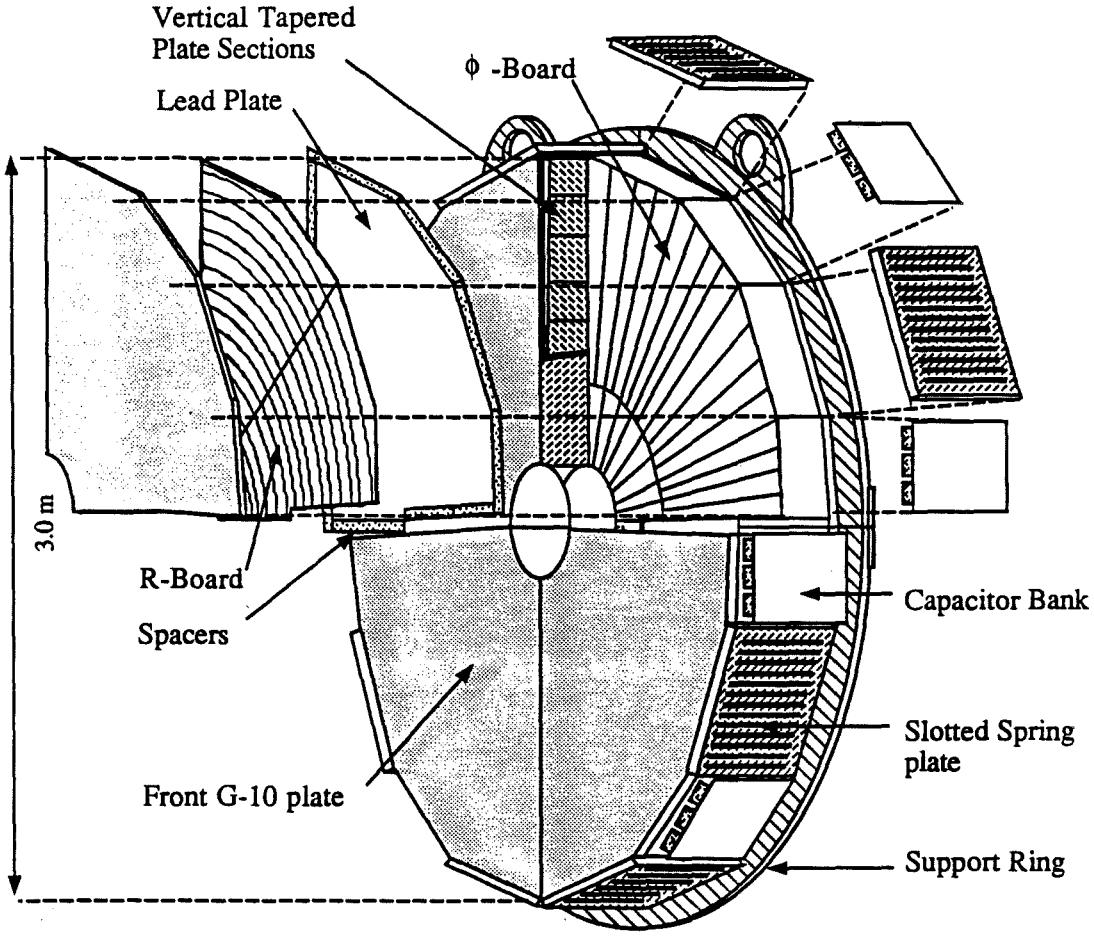

Figure 2.5 An exploded view of the EMLAC.

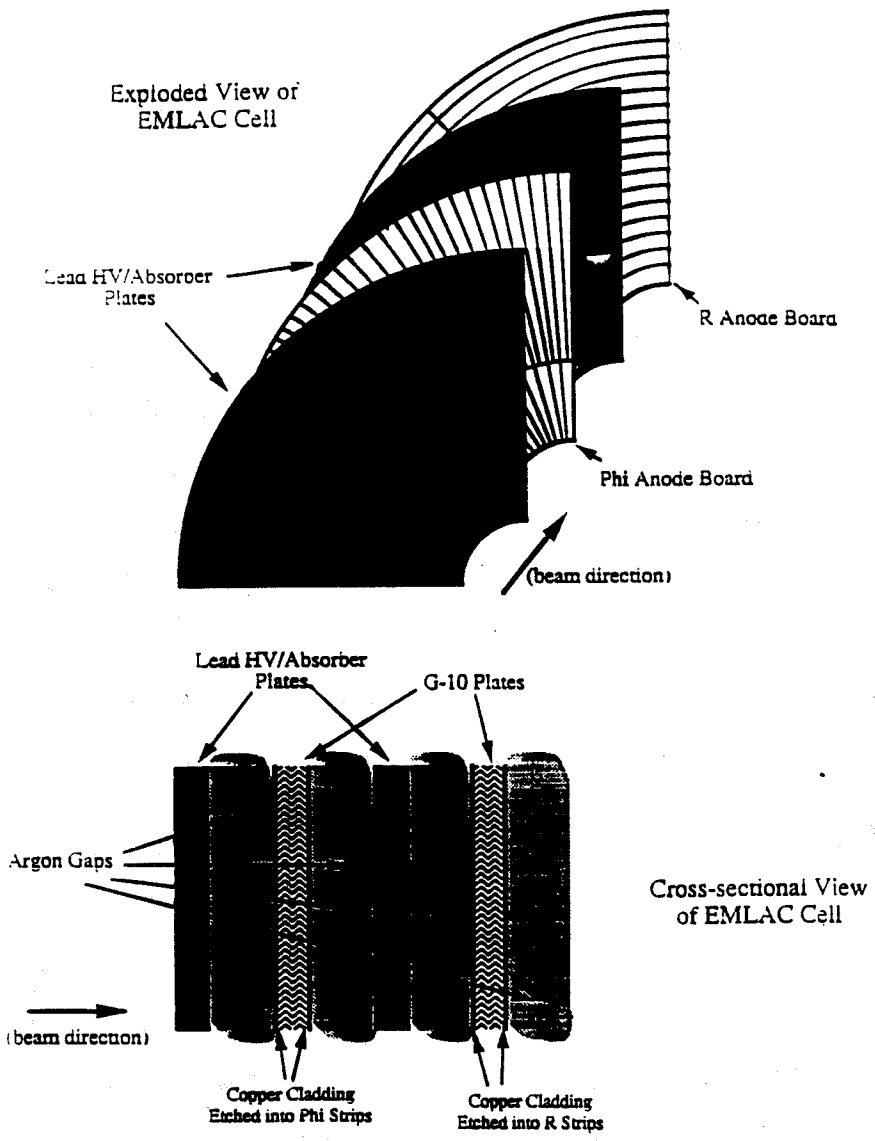

Figure 2.6 A single EMLAC cell.

View	Strip Numbering	Center Position Of Strip i
R	0 to 255	$20.22 + i * (.5466)$ cm
inner-ϕ	1 to 96	$\pi * (i - \frac{1}{2})/192$ rad
outer-ϕ	1 to 192	$\pi * (i - \frac{1}{2})/384$ rad

Table 2.4 The strip numbering within an EMLAC quadrant.

of 40 cm at the front of the EMLAC. This boundary was focussed in the same fashion as the strips in the radial view.

Corresponding R strips from each of the first 11 cells in the front section were "ganged" together into a front section for readout purposes using customized wires called connector strings. Similarly, the signals in cells 12 through 33 were also summed together into a back section for readout. Figure 2.7 illustrates how the summation was arranged. Signal summation was necessary for two reasons. First, the cost of the electronics and the data acquisition time required to read out each and every strip would have been prohibitive. Second, the signal on an individual strip would have been so small that it would have been dominated by the capacitance of the cables.

Connector strings were run along both edges of the quadrant to read out the radial strips of each corresponding octant R board. The inner ϕ strips were read out along the inner edge of the quadrant; the outer ϕ strips along the outer edge. These front (or back) section connector strings were attached to several readout boards at the front (or back) of the quadrant. Low impedance cables were attached to the readout boards via connectors which carried the signals from the device to the calorimeter feedthrough boxes located in the cap, where amplification and readout was performed.

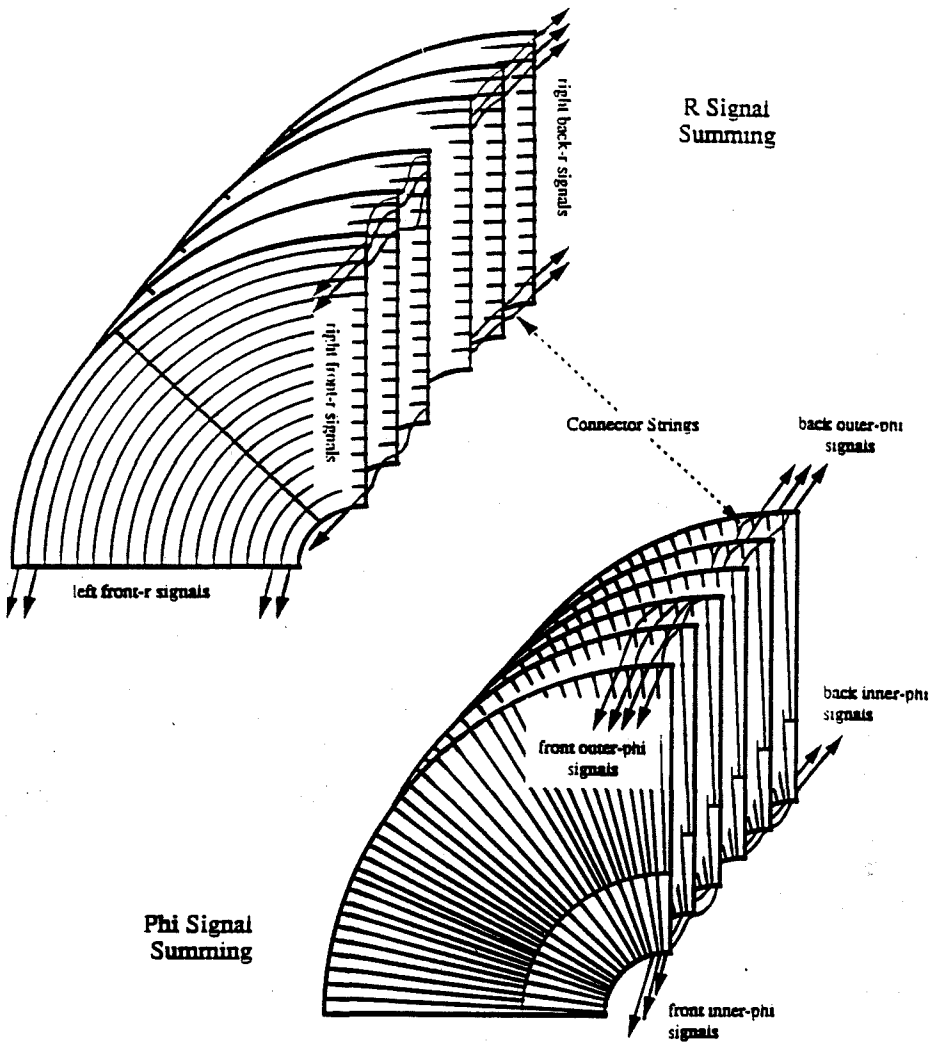

Figure 2.7 The EMLAC signal readout scheme. Within each octant and view, corresponding channels were connected together to form front and back section signals.

This division of the EMLAC readout into front and back sections improved the ability to resolve very close di-photons. For a further explanation and figure, see section 5.2. It also gave an indication of the longitudinal shower profile which could be used as a method of hadron discrimination. From a readout standpoint, each octant was considered to contain 2 sections – a front and back, and 4 views – left R, right R, inner ϕ, and outer ϕ. Strips were numbered such that a strip in the front section would line up with the identically numbered strip in the back section. See table 2.3 for further clarification of the numbering scheme of an EMLAC quadrant. Due to physical constraints, some numbered strips were missing near the edges.

2.4.6 Hadron Calorimeter

The hadron calorimeter (HALAC) [21], immediately downstream of the EMLAC, also utilized liquid argon as its active material. However, the HALAC employed stainless steel as the absorber material instead of lead. Since showers produced by hadrons are typically much broader than electromagnetic showers, a rather coarse pad geometry was selected for the readout of the HALAC. This pad geometry greatly simplified the software required to reconstruct the showering hadrons. Towers of pads do not require sophisticated energy correlation routines to match the energy deposited in two separate views (R and ϕ) as was done done for the reconstruction of showers in the EMLAC.

The HALAC had a focussed geometry as well. The pad sizes changed as one moved further from the target region to maintain the focussing on the target. The height of the pads ranged from 10 to 14 cm.

The HALAC consisted of 53 cells. Each cell was built from a 1 inch thick stainless steel plate, a sampling module commonly referred to as a "cookie", and argon gaps. The HALAC was longitudinally segmented with 14 cells in the

front section and 39 cells in the back. Each cookie consisted of seven layers of single sided copper clad G-10 glued together into an octagonal unit 4 m in diameter. The cookies contained high voltage planes, spacers, argon drift gaps, and detector pads.

Figure 2.8 illustrates an exploded view of a single cookie. At the center of the cookie in depth, two anode planes were positioned back to back. The sides of these anode planes that faced outward with respect to the cookie's center line were copper clad. The copper was scribed into rows of triangular pads which created electrically isolated areas of charge collection. Charge collected from the horizontal rows of triangles was channeled to the edge of the plane via signal traces that ran horizontally between the rows. The anode planes were aligned so that each row of triangular pads upstream shadowed a row of signal traces on the downstream plane and vice versa. When the stack was fully assembled and viewed from upstream, it presented an unbroken plane of triangles (Fig. 2.9). The anode planes faced the high voltage planes. The ionization gap between high voltage and charge collection planes was 3 mm. This gap width was maintained by G-10 spacers which ran horizontally along the boards and covered the signal trace lines. These spacers also displaced the liquid argon in front of the signal traces which inhibited those traces from collecting energy. The high voltage planes themselves were made of double sided copper clad G-10. The side of the HV plane facing the anode was held at HV while the other side was kept at ground.

2.4.7 Forward Calorimeter

A significant percentage of the energy from interactions escaped down the 40cm diameter hole in the EMLAC and HALAC. Most of this energy was carried by the fragmentation products of the non-interacting partons of the

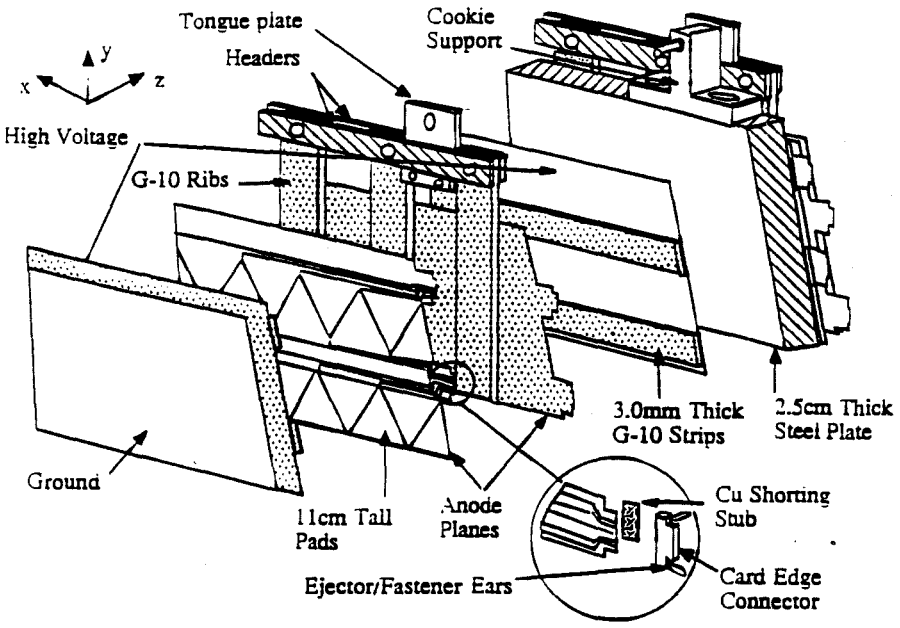

Figure 2.8 An exploded view of a HALAC "cookie" or single cell.

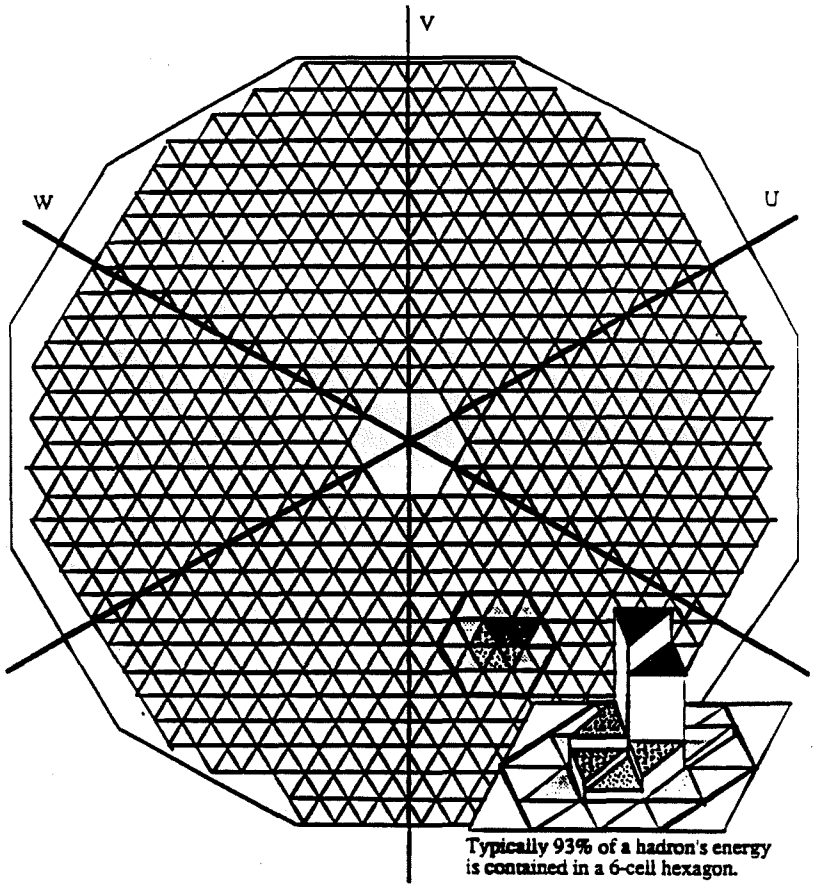

Figure 2.9 The pad geometry used in the HALAC. Each triangle represents an isolated copper pad. These pads are read out using small strips running from the bottom of the pad to the readout boards on the side of the detector.

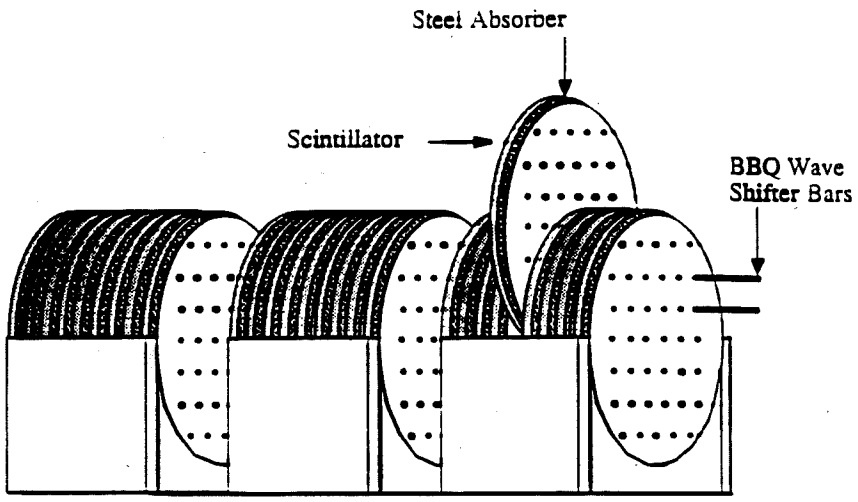

Figure 2.10 The forward calorimeter.

beam particle. A forward calorimeter (FCAL) was designed and positioned approximately 17 meters downstream of the LAC to measure particles in this region [22]. This device is shown in Fig. 2.10.

This calorimeter was divided into three separate but nearly identical modules. Each module contained 32 steel plates and 32 scintillator sheets measuring 45 inches in diameter. The steel plates were 3/4 inch thick while the scintillator sheets were 3/16 inch thick. A set of 76 holes were drilled on a 4.5 inch grid perpendicular to the flat face of both the steel and scintillator plates. Wave shifter rods were inserted into each hole. For the 1990/91 data run, only the inner 60 of the 76 possible holes were instrumented. These wave shifter rods were made from acrylic and doped with an organic dye (BBQ) that shifted the blue light created by the passage of charged particles through the scintillator sheets to green light which was more efficiently detected by the phototubes. The rods were doped to absorb UV light produced by particles passing down the bars, potentially creating anomalous signals. Phototubes were attached to the rod ends to collect the signal. Modules 1 and 2 had phototubes attached at both ends of the waveshifters, while module 3, the most downstream module, had phototubes attached to the upstream end of the rod only. A 1.25 inch diameter hole through the entire array of detector material allowed for the passage of non-interacting beam particles.

The FCAL was capable of operating at 10 megahertz. The signal from each wave shifter was flash digitized by custom CAMAC modules developed at the University of Minnesota. When the experimental trigger was received, a voltage history of the preceding 2.56 microseconds was available for each phototube.

Chapter 3 The Data Acquisition System

3.1 Overview

The E706 data acquisition system was complex. It was, however, based upon three relatively simple underlying design principles:

- Non-experts must be able to run the system effectively;
- Each piece of apparatus must be able to run by itself or integrated with the other sub-systems;
- Data must be merged into a single integrated output stream.

These principles were implemented using VAXONLINE, Fermilab's on-line data acquisition software package [23], and by subdividing the data acquisition tasks into four separate subsystems based on the experimental hardware. These four subsystems were implemented with three PDP/CAMAC based DA systems and one FASTBUS/RABBIT/VAX system (see Table 3.1).

System	Device to be Read Out
FASTBUS	LAC and Straw Tube Drift Chambers
PDP NEU	SSD's, PWC's, Trigger
PDP ROCH	FCAL
PDP MU	E672 Muon Chambers

Table 3.1 The devices included in each DA subsystem in the E706 DA.

VAXONLINE, running on a Micro VAX computer, was the main driver of the data acquisition system (DA). It was the glue that bound the individual components of the apparatus together. It consisted of four major components: Event Builder, Output, Buffer Manager and Run Control.

3.2 The Software (Event Builder, Output, and Run Control)

Event Builder executed the programs and lists necessary to read out the information from a particular piece (or several pieces) of apparatus. It checked each of the event headers (one from each subsystem above) to verify that they were in agreement before the records were merged (e.g., all records belonged to the same event). Assuming the event numbers for each piece of apparatus were identical, Event Builder concatenated the individual pieces into one large record. It attached its own header to that record. This record was then sent to a staging buffer pool. Output, a separate task, took the events from the staging pool and wrote them to some specified media: either disk, 9 track tape, or in our case, 8 mm cassette.

Run Control managed these processes as well as initiated begin run tasks, including hardware initialization, trigger setup, and calibration tasks. Figure 3.1 illustrates the basic layout of the readout of the apparatus.

The LAC DA system underwent a complete overhaul between the 1988 and 1990-1991 data runs. This change was imperative if the experiment was to meet its physics goals. The MX controllers, intelligent data collection devices designed by Fermilab as a lab standard, and used in the 1988 data run were no longer going to be supported by the lab in their E706 configuration. The MX (forerunner to the E706-designed ICBM) was crucial to the 1988 DA system. Each MX board, much of which was wire-wrapped, was responsible for the readout of a subset of LAC amplifiers. It was a complicated device with many idiosyncrasies. The experiment had few experts on these units, and few spare boards of the E706 configuration were available. Readout speed for the MX was slow, and thus overall experimental "live-time" was impacted. Two additional charged particle detectors (straw tube drift chambers) were to be incorporated into an

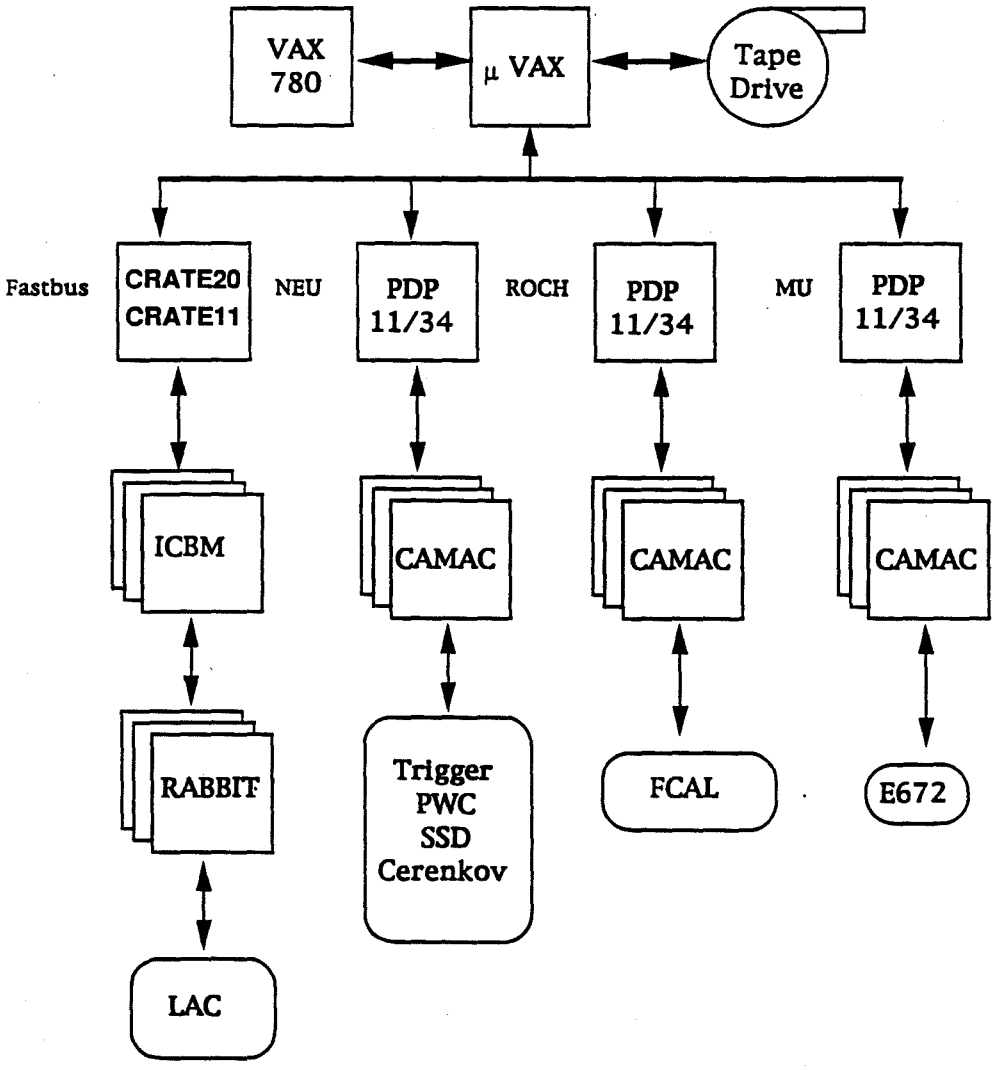

Figure 3.1 Schematic of the 1990-1991 DA architecture.

already crowded data concatenation scheme. Additionally, new FASTBUS [24] technology had been adopted as a standard by FNAL, and its implementation was advertised to be relatively straight forward. Since this author was one of the two principal architects of the new DA system, a detailed discussion of the 1990-1991 FASTBUS system will follow.

3.3 Hardware Overview

It is difficult to follow a detailed discussion of the inner workings of the DA system without having some understanding of the hardware involved. The hardware for collecting and receiving the data consisted of one or more of the following: a FASTBUS crate, MDB-DRV11W card, LeCroy 1821 FASTBUS segment interface, LeCroy 1892 memory module, Struck GPM crate master, 1821/ECL interface to the 1892, 1821/DEC card link to the VAX, the ICBM digital signal processor slave, its associated analog WOLF card, along with the entire RABBIT system and its associated modules. The key modules, their function, and their dominant characteristics are described below.

3.3.1 The RABBIT System

The RABBIT (Redundant Analog-Bus Based Information Transfer) system was responsible for the charge collection and digitization of the raw data from the electromagnetic and hadronic calorimeters. It was the link between the LAC and FASTBUS. This system was based on crates which have two, more or less redundant busses over which analog and/or digital data may be passed [25]. Each RABBIT crate contained up to 20 charge integrating amplifier cards (LACAMP), 2 digitizing units (EWE) and a Before-After Timing module (BAT). Each LACAMP card has 16 channels of amplifiers in addition to 8 channels of Time to Voltage Converters (TVC) to measure the time of arrival of energy depositions. The BAT module received and distributed the trigger signal that

latched the amplifier signals in the sample and hold capacitors. The BAT also supplied several crate wide timing and voltage signals and terminated both busses. The data stored in each LACAMP was digitized in the EWE under the control of a series of custom built FASTBUS digital signal processor (ICBM) units [26].

3.3.2 LeCroy 1821 SMI

The 1821 is a smart FASTBUS Master (crate controller) that executed microcode to perform readout and control functions [27]. The 1821 controlled the bus and could perform reads/writes to other modules within a segment (FASTBUS crate) as well as internally. This module was capable of executing one microcode instruction in 33 nsec and had 16 kilobytes of internal buffer memory. Furthermore, the 1821 was able to interface with a variety of personality cards that allowed the crate to interact with the outside world. Once the 1821 had been initialized and the programs loaded, this module acted as an independent, free running data acquisition processor.

3.3.3 LeCroy 1892 Memory Module

The LeCroy 1892 is a multiple record buffer memory slave module [28]. Its job was to accumulate and store data in a first in/first out (FIFO) manner. Each module contained 4 megabytes of memory and had 32 bits of ECL input. The modules can be used in a linear readout scheme or in circular mode. Our 1892's were modified so that multiple modules could be ganged together to look like one long linear buffer.

3.3.4 Struck GPM

The GPM (General Purpose Master) is a computer built on a FASTBUS board [29]. It was based on the Motorola 68000 and had 32 kilobytes of fast

memory. This module was extremely flexible. The programs it ran could be written in C or assembler. These programs resided on the VAX, and were downloaded into RAM on the GPM board. This module handled all of the decision making, error handling, etc., for the LAC DA system. Although this module was a master in its own right, it was directly controlled by the 1821 in our system. The version of GPM used in this experiment was incapable of handling DMA (Direct Memory Access) transfers to the VAX hence the need for an 1821 module as well.

3.3.5 ICBM

The ICBM is a FASTBUS slave module designed around the Motorola DSP56001 Digital Signal Processor (DSP). Its principal designer, Eric Prebys of the University of Rochester built this card specifically for this experiment. It has a total of 192000x24 bits of onboard memory, which was accessible both to the DSP and to FASTBUS. Some of these memory addresses were mapped to an internal register space to communicate with a second partner module (WOLF) and miscellaneous logic signals via the FASTBUS auxiliary connector. The WOLF was an interface between the ICBM (FASTBUS) and the EWE(RABBIT).

3.4 1990 DA System Overview

The readout of the LAC consisted of five functions:

- Amplifier readout
- Data buffering
- Data transfer to VAX
- LAC calibration
- Monitoring of the apparatus.

These functions were organized to take advantage of the accelerator cycle: 23 second beam spill, followed by 35 seconds of acceleration of beam. The increase in readout speed from what was achieved with the 1988 system was accomplished by buffering data during each step of the process and running the readout tasks in parallel. Buffering allowed the relatively fast LAC readout to proceed at high speed during the spill, while allowing the slower VAX transfer the full 58 seconds between the start of two successive spills to complete its task. Additionally, calibration and monitoring of the LAC RABBIT electronics was performed between spills in parallel to the data transfer process. Section 3.7.1 through section 3.7.3 will discuss the FASTBUS system, which controlled the 1990-1991 LAC and Straw Tube readout process.

3.5 The FASTBUS Readout Process – An example

The FASTBUS readout system was divided into two functional tasks that occurred in parallel. One task, running in Crate 11, was responsible for LACAMP readout and local event buffering. The other task, running in Crate 20, was responsible for event assembly and transfer to the VAX for bulk storage. To illustrate how this data acquisition system functioned, it is instructive to look at how one event made its way through the system. Figure 3.2 shows a schematic of the hardware involved.

3.5.1 Step 1 – Data Collection and Buffering

The first step was to collect the energy deposited in the LACAMPS from showers in the LAC. These LACAMPs were read out in a multi-step process controlled by the STRUCK GPM Crate master in FASTBUS Crate 11. A trigger, issued by the experiment, was fanned out to the three PDP's and to FASTBUS. In the FASTBUS system, the trigger was received by the GPM in Crate 11. The GPM, before receiving the trigger, was either transferring data to

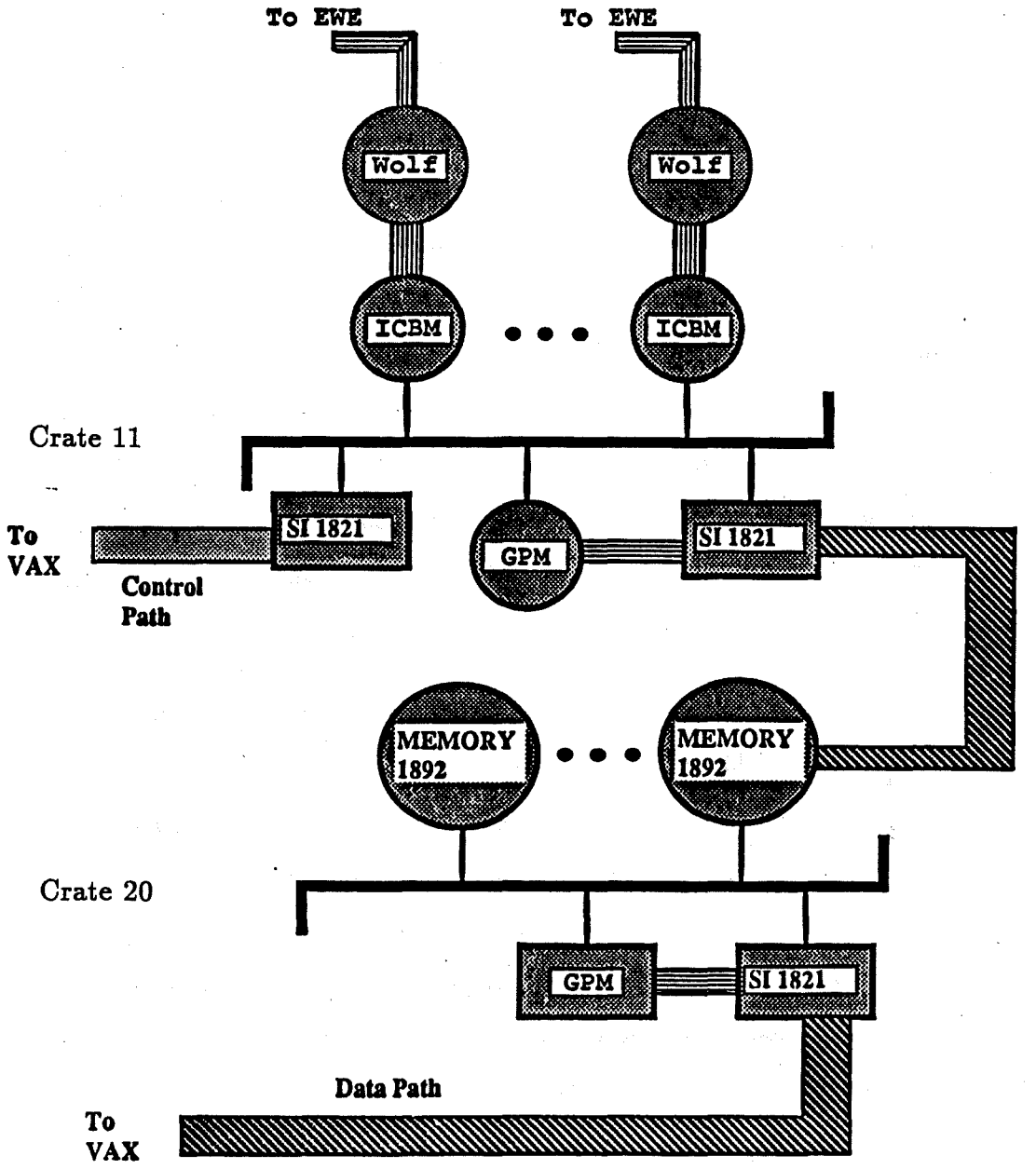

Figure 3.2 1990-1991 data acquisition hardware for the LAC.

the FASTBUS data buffer in Crate 20, or was waiting for the next trigger. If it was transferring data to Crate 20, then the GPM was allowed to finish reading out the ICBM it was currently servicing before initiating the readout of the LACAMPS. There was no conflict for space here since the ICBM's performing the readout had 4 separate buffers, each of which could contain a complete event.

To service the trigger, the GPM issued a FASTBUS broadcast to start all 15 ICBM modules simultaneously. Fourteen ICBM's were used to read the 28 Rabbit crates. The remaining ICBM was used to sequence the other 14 with the trigger. A typical RABBIT crate contained 20 amplifiers, each of which had 16 channels, so a single ICBM was responsible for a total of roughly 640 channels. The ICBM issued commands to the EWE to digitize the charge in the LACAMPS. The digitized data was transferred from the EWE register to an available buffer on each ICBM. The GPM also asserted a "busy" which prevents the trigger from initiating further data taking until the current event had been processed at the LACAMP level.

Upon completion of the readout of the energy detected by each LAC channel, the ICBM began the task of reading out the time to voltage converters (TVC). This occurred as a two-stage process. First, the ICBM scanned through the data it just read out and selected those channels with energy above a software threshold. Since one TVC channel corresponded to four analog signals, it was the sum of the 4 analog channels that was required to be above threshold in order for the TVC readout to occur. Then the ICBM issued the necessary commands to digitize those TVC channels whose signal exceeded the threshold.

Each ICBM set a "Done" level upon completion of its assigned readout task. These levels were put in coincidence. When all 15 ICBM's indicated completion, a reset signal was sent to the trigger and the GPM. The system was now ready

to accept a new event and to continue transferring data from its internal buffers to the large buffer memories in Crate 20. The trigger "busy" was lifted and the spectrometer was again "live", that is ready to accept another event.

3.5.2 Step 2. – Buffer Readout to Mass Storage

The second major step in the readout process was to move the data now buffered in Crate 20 up to the central DA computer where it was then concatenated with data from the other detectors to form a single complete readout of one interaction. This process occurred in parallel to the read out of the LACAMPS via Crate 11. Crate 20 housed six LeCroy 1892 buffer memory modules. Each of these memory modules had 4 megabytes of fast memory. Four of the six modules were daisy chained together to form one large linear buffer, and were used to temporarily hold the data from the LAC; the remaining two 1892's contained data from the STRAW's – each STRAW chamber had its own 1892. The readout of the 1892's was accomplished using a GPM in conjunction with an 1821 SMI. Logically, the GPM acted as a mini-Event Builder. It read data from multiple sources, verified the run and event numbers, concatenated the separate pieces of information into a single record, and attached its own header so that the data could be interpreted later. Details are provided below.

Step 2 of this readout process was under the control of the VAX. The VAX, through Event Builder, executed a list which communicated to the 1821 SMI through the 1821/DEC card that it was ready to receive data. The 1821 then, through a front panel signal, indicated to the GPM that it needed some data. The 1821 SMI could not proceed further until the GPM had the data it wanted and went into a "hibernation mode" until it received an interrupt from the GPM. Meanwhile, the GPM began to poll a specific location in the 1892 memory and checked for an indication that fresh data had been transferred. Once new

data arrived, a series of checks were performed on the data to insure that the individual data segments from the LAC and each of the STRAW Chambers all belonged to the same event. If it did not, then the data was not accepted into the GPM's memory and the GPM went on to read a new set of sub-events. If it did, then the GPM read in the data from the three 1892's in the order of LAC, upstream STRAW chamber, then downstream STRAW chamber. It was the GPM's responsibility to keep track of the data already read by each of the 1892's.

A header was then attached to this event in the GPM indicating the run and event number, the size of the event, and a pointer to the beginning of each of the three subevents with respect to the header location. The GPM repeated this process until its 32 kilobyte buffer was full with an integer number of events. During normal running, the GPM buffer would typically hold 4 events before it was full.

At this point, the GPM transferred control back to the hibernating 1821 SMI via an interrupt sent to its front panel. The 1821 shipped the data to the VAX through a 1821/DEC personality card and a DRV11W interface. The 1821 was not concerned with maintaining the integrity of single events. It shipped data to the VAX event pool in 4 kilobyte chunks. The GPM, at the time this system was designed and built, did not have the capability to perform direct memory access (DMA's) . Single word transfers from the GPM to the VAX was unacceptably slow. Hence, the 1821 was used for this DMA operation.

The above procedure constituted one cycle through the 1821 list. This cycle occurred repeatedly as Event Builder requested more data from each of the four data acquisition computers.

3.5.3 Calibration and Monitoring Tasks

Once FASTBUS Crate 11 had completed its readout tasks for a given spill, it then performed calibration and monitoring tasks on the RABBIT system. These tasks included:

- Continuity checks of all data cables
- Amplifier gain checks
- Amplifier pedestal checks
- Temperature measurements of each amplifier crate
- Voltage measurements of amplifier crate power supplies
- Inventory of RABBIT cards

These between spill calibration and monitoring tasks were controlled by the GPM in Crate 11. After each event was processed, the GPM checked the status of the accelerator spill. If the spill was still in progress, the GPM expected to see new triggers and continued the normal readout path described above. If the spill had completed, and the accelerator magnet currents were ramping back up, the GPM executed one of the between spill tasks from the above list. A different task was performed during each between spill period. Most of these tasks required a few seconds to complete. However, the gains task took most of the allotted 35 seconds to complete. The data acquired between spills was compared on-line with data taken during the previous calibration run. If there was a significant difference between the two sets of data, a warning message was printed on the status screen indicating a potential problem. With an alert operator, a problem in the LAC system could be detected within (at most) 6 spills of the failure.

3.6 Performance

The FASTBUS readout was tested to determine the maximum data rate that could be achieved. The buffer sizes, burst rates, and numbers of 8 mm tape drives were all tuned in order to obtain maximum throughput. To minimize the dead time due to the LAC readout, a maximum data taking rate of 100 events per second was set as the goal. With an expected data rate of 25-30 Hz, the dead time due to the LAC readout was comparable to that of the other components of the DA. The first step in the readout was the extraction of the data from the LACAMPS via the ICBM's. The ICBM program was written in assembly language to optimize its performance. The ICBM was capable of reading two RABBIT crates containing 20 LACAMPs (640 channels) each in 7.4 milliseconds. If all possible TVC channels were also read out, then this time increases to 9.2 milliseconds. The average readout speed during standard running was 8 milliseconds per event.

The read out of the ICBM's by the 1821 in Crate 11 proceeded in parallel to the readout of the LACAMPs. If a new trigger was received before the 1821 finished reading out an event, a small dead-time was introduced to finish reading out the current ICBM and save several pointers. With the ability to buffer up to four events in the ICBM, the next trigger was accepted with a minimum of dead time as long as a buffer was available. Tests showed that this configuration would leave at least one free buffer at all times.

The remainder of the system could use the entire accelerator cycle time to complete its task. Readout of the LAC and straw tube chambers in Crate 20 was limited by the bandwidth of the VAX backplane and the bandwidth of the particular device to which the output was written. To maximize throughput, we used a dual 8 mm tape drive system in which alternating events were spooled

to each drive. In this configuration, data could be read out at a rate of 320 kilobytes/sec. At this rate, the average time to read one 1892 was 12.8 seconds, and a typical spill of $\approx$ 500 events was completed in 56 seconds, 2 seconds ahead of schedule. Writing to disk could have increased the data throughput to 400 kilobytes/sec, but we would have quickly run out of space to store the data acquired.

3.7 Advantages of the New LAC Readout System

The new LAC readout system significantly improved the physics capabilities of E706. The readout speed was significantly faster which increased the experimental live time. This made possible the acquisition of higher statistics. More importantly, readout of the entire detector allowed us to study lower energy showers. During the 1988 data run, zero suppression was employed, and thus channels whose energy fell below 175 MeV were not read out. We were unable to analyze low energy showers with confidence. These showers are critical if one is to measure the low energy π^0 and η components of away-side jets.

Figure 3.3 illustrates the potential improvement in shower reconstruction as a result of the new readout system. These plots are pulse height distributions (in GeV) in R and ϕ strips of individual LAC quadrants for specific events recorded in 1990; the dashed line represents the readout cutoff employed in 1988. Figure 3.3a is characteristic of quadrants containing a triggering shower, and demonstrates that the reconstruction of large energy showers is not seriously compromised by the suppression of low pulse height channels. Figure 3.3b is more characteristic of quadrants containing showers produced by an away-side jet (non-triggered quadrants); here there are not only more showers but each is, on average, relatively low in energy. There obviously is a substantial

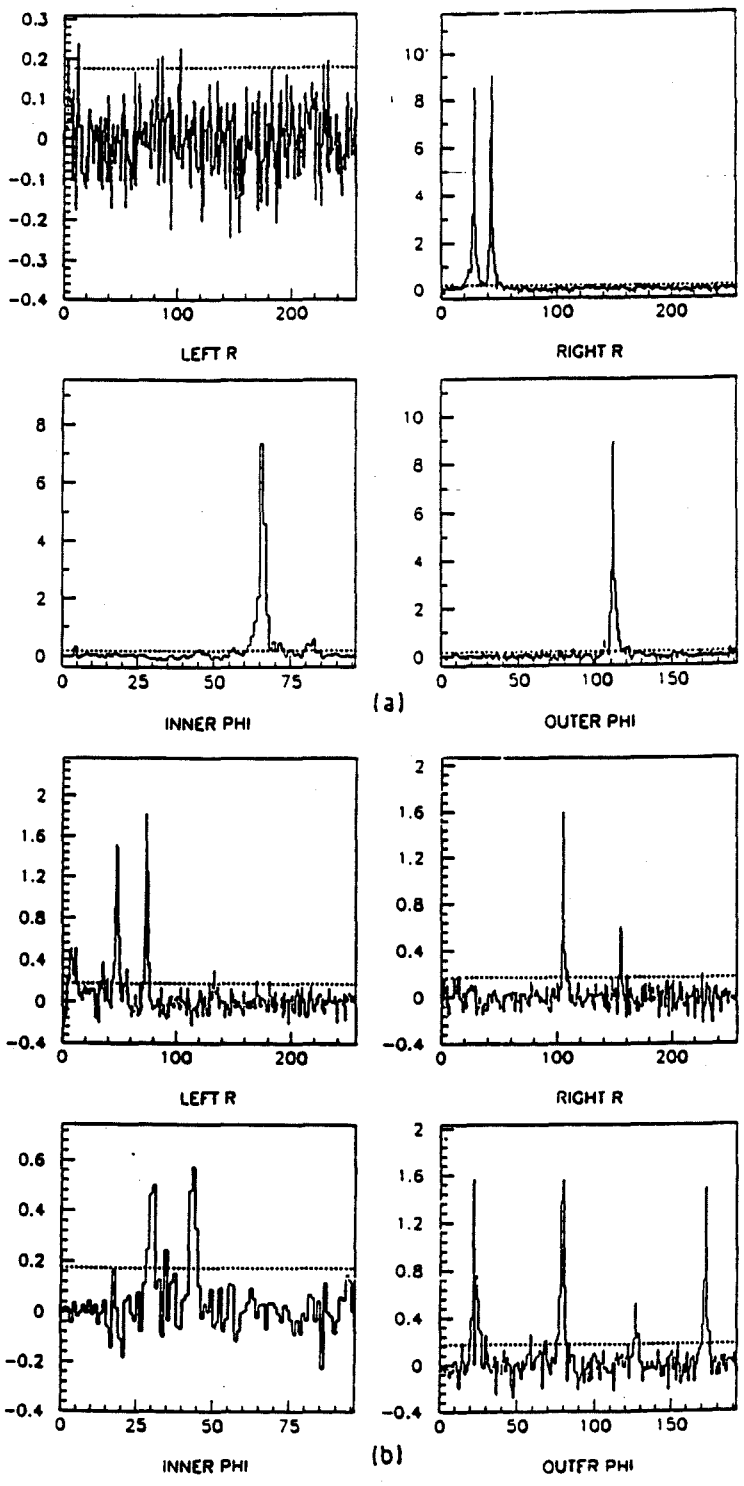

Figure 3.3 LAC pulse height distributions for the 4 subdivisions of a (a) triggering quadrant (b) and non-triggering quadrant. Vertical scale is in GeV, horizontal scale is in strip numbers.

amount of potentially valuable information gained by reading out the entire LAC, particularly in the non-triggering quadrants.

3.8 Zero Suppression

The issue of zero suppression merits further discussion. Each amplifier has an associated intrinsic value called a "pedestal". This pedestal is the value an amplifier reads from a specific channel of the detector when there is no external shower in the vicinity. Effective zero suppression depends on the ability to determine these pedestals a priori and also on the stability of these pedestal values over time. The 1987-1988 zero suppression routine was not very sophisticated. It did not make use of a separate pedestal for each channel. Rather, one nominal pedestal value was used. Any signal that was below this nominal value was not read out. In order for zero suppression to reduce the record size, and hence the amount of memory needed to buffer one spill, at least half of all available channels must be thrown away. This is because one has to map the data read out back to physical locations in the detector. If the entire detector is read out then this task is trivial, assuming a constant readout order. However, if the information from some channels is suppressed as they are read out, then each data word requires both the data value of that location and its channel address. Hence, when zero suppression is employed, the effective data word is two physical words long.

Chapter 4 The Trigger System

4.1 Introduction

In order to study rare phenomena such as high p_T particle production or direct-photon physics efficiently, one needs to be able to select and keep only those events which are of interest to this particular area of analysis. A trigger system was built to enhance our sample of rare, high p_T phenomena. Low p_T events were selectively rejected by the trigger so that they did not consume valuable data acquisition and data analysis resources. Furthermore, the trigger enabled the experiment to be "live" longer which increased the probability of recording high p_T events. A complete discussion of the trigger is given elsewhere [30]. What follows is an overview.

E706/E672 used six different classes of triggers: Beam, Interaction, Single_Local, Two_Gamma, Local•Global, and Di-Muon. Each trigger was designed to illuminate a certain class of physics or to aid in the understanding of the data and the detector. The Single_Local trigger, the principle trigger of the E706 analysis to date, was used to select on highly localized clusters of energy (effectively p_T). However, it is important to remember that there were a variety of other triggers which were designed to select lower energy, symmetric, $\pi^0, \eta, \omega, ...$ mesons which would not necessarily have satisfied the Single_Local requirement. Since many of these other triggers were set to lower thresholds than the Single_Local, they were prescaled so that the experiment could still illuminate the high p_T end of the spectrum, where its main physics goals lie.

The Single_Local is not the ideal trigger with which to study high p_T η production. An η with a p_T=4 GeV/c which decayed into two photons would have a typical photon separation of 25 cm at the LAC. This distance

is much larger than that of the Single_Local definition. Although there is a geometrical acceptance tradeoff, the behavior of the Single_Local trigger is the best understood trigger at this time, thus it will be the principal trigger employed in this analysis.

As stated above, the Single_Local trigger used in this analysis was designed to select events containing a high-p_T (greater than $\approx$ 4 GeV/c) photon or π^0. Experimentally, the signature for such events was a localized deposition of energy within the EMLAC, with a p_T determined by:

$$p_T = E \times \sin(\theta) \approx E * R/900. \qquad 4.1$$

where E is the amount of energy which was deposited in the EMLAC and θ is the angle between the beamline and a line from the interaction to the point of energy deposition (the production angle) and R is the radius in cm.

The R–ϕ geometry of the EMLAC was designed specifically for this trigger measurement of p_T. The amount of p_T in a given region of the detector was given by:

$$p_T = \sum_i (E_i \times \sin(\theta_i)) \approx \sum_i (E_i \times r_i/900.) \qquad 4.2$$

where the sum was over the front and back EMLAC strips within the region, E_i is the energy which was deposited in strip i and θ_i is the production angle to that strip. The p_T depositions were calculated by a dedicated system of electronics, the "p_T System".

4.2 The p_T System

The p_T system consisted of a set of custom made electronic modules designed in accordance with the RABBIT standard. Eight crates, each containing 20 p_T cards, were used to instrument the LAC, one crate for each octant. These crates were physically located in the Faraday room just under the Rabbit crates containing the LACAMPS.A single ICBM housed in FASTBUS crate 11 (located in the counting house) controlled the entire p_T system. This ICBM performed diagnostic checks and downloaded various trigger weighting and threshold schemes to each of the 8 p_T crates.

The p_T cards performed two basic operations on the energy pulses received from the fast output channels (fast-outs) of the R view LACAMPS. First, they summed neighboring pairs of channels and weighted them by $\sin(\theta)$ to produce an analog transverse momentum signal. Second, they then added these sums together to form a sum p_T signal for groups of 8 channels, referred to as the "sum_of_8" signal. (see Fig. 4.1) The advantage of the R–ϕ geometry was that with $\sin(\theta)$ weighting, the summed and weighted energy signals represented the p_T deposited in the EMLAC over a given R region.

4.3 Trigger Formation

The trigger system was made up of 4 components: a beam hodoscope, a hole counter, 4 interaction counters, and the EMLAC p_T system. Each of the components played a unique role in determining whether a given beam particle was tagged as having undergone an interaction in the target region that was of interest to the physics goals of E706. The following few sections describe how a LAC trigger was formed.

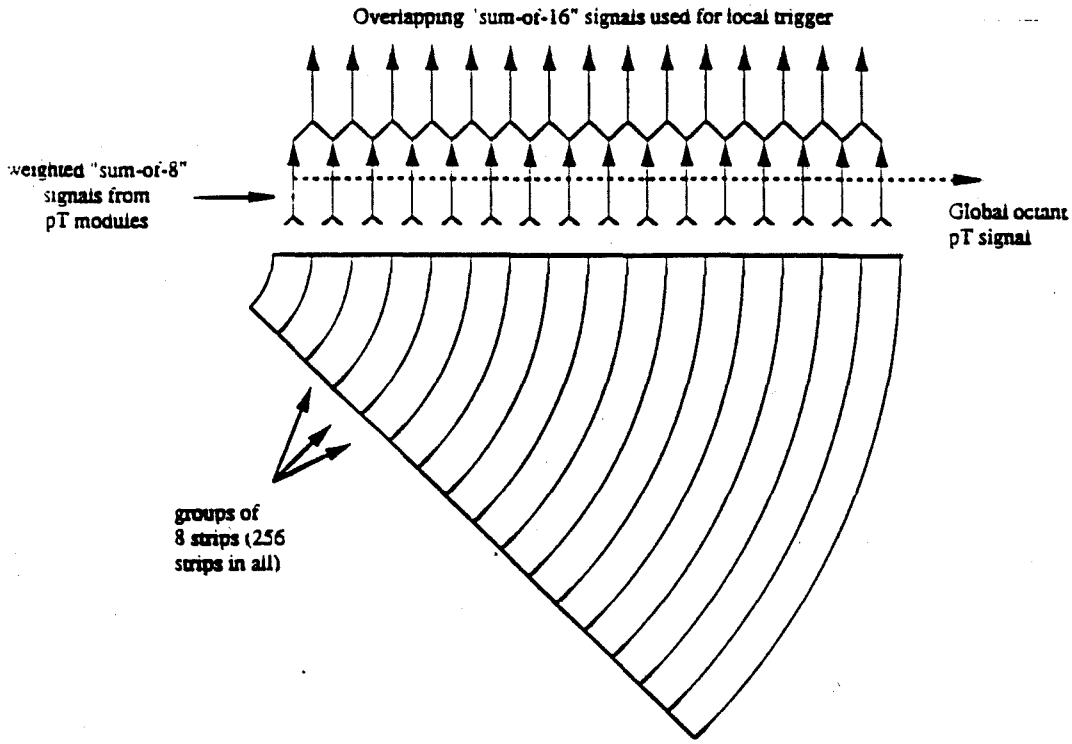

Figure 4.1 The summation scheme of the EMLAC R channels used to form the sum_of_8 signal, the backbone from which all trigger signals are formed.

The beam hodoscope served a dual purpose. It provided a beam profile that was used to center the beam on the experiment, and it was also the main component in the first stage of the trigger definition. The hodoscope determined whether a given RF bucket contained zero, one, or multiple beam particles. A single beam particle in a given RF bucket was defined by the requirement that one and only one contiguous group of hodoscope elements in two of the hodoscope's three planes have detected signals. This contiguous group of elements was commonly referred to as a cluster. If the hodoscope detected exactly one particle in the accelerator's RF bucket, it satisfied this portion of the trigger definition. Two clusters which fired simultaneously in at least two of the three planes of the hodoscope indicated the arrival of multiple beam particles in a single RF bucket. This class of events was rejected by the trigger and the hodoscope returned a FALSE logic signal.

A plastic scintillator counter located 2 cm downstream of the hodoscope was used to reject particles which came from the beam halo. These particles were capable of firing the hodoscope, but typically had trajectories which would have caused the particle to miss the target region. This counter was referred to as BH, or the hole counter since it had a hole drilled through its center. The counter was positioned so that the hole's center was aligned with the silicon strip detectors. Beam particles which passed through the hole did not register in the counter, and satisfied the trigger requirement. Beam particles which hit the counter were vetoed.

The interaction counters, located both on the upstream and downstream ends of the analysis magnet, were spatially oriented so that they shadowed the LAC. A trigger was satisfied if at least two interaction counters fired.

Using these three trigger devices, a clean interaction was defined as the logical AND of the following:

one cluster in at least two of the three planes in the hodoscope

•

at least 2 interaction counters fire

•

no hit in beam hole counter

•

no additional interaction within ± 3 buckets of the candidate trigger

4.3.1 The Pretrigger

Since the trigger p_T calculation could not be completed in time to latch all information associated with an event, a pretrigger was built to latch candidate events while the evaluation was completed by the trigger system. The pretrigger rejected the bulk of the very low p_T events. The pretrigger also provided a tight constraint on the timing of signals arriving from the LAC so that the trigger did not fire on p_T depositions from other interactions.

To instrument a pretrigger, a p_T card determined the single strip p_T values for an event from information from the fast-outs of the LACAMPs and then added these together to produce an analog "sum_of_8" p_T. These sum_of_8 signals were then sent to the p_T Adder card. The Adder cards summed up the total p_T signal for one half of each octant. The p_T signal for each half octant was then sent to a zero_crossing timing discriminator in order to match the timing of the p_T signals with the corresponding beam and interaction signals. A zero_crossing discriminator was used rather than a normal time over threshold discriminator because of the improved stability of the output signal. The width and leading edge of a pulse generated by a normal discriminator varies greatly depending upon the height and shape of the input signal. This effect

is minimized for a zero_crossing discriminator by producing two copies of the input signal. One copy is delayed by an external cable, inverted, and then added to the original signal. If the input signal is above the desired threshold at the zero crossing time, then the discriminator generates a fixed width logic output. The zero_crossing time is not terribly sensitive to moderate changes in the input pulse shape or in the pulse height, thus providing a more stable timing reference for the LAC signals.

The signals generated by the zero_cross discriminators were sent to a series of logic units where the timing was compared with the interaction signals. The pretrigger vetoes, early p_T, SCRKILL, and the veto wall requirement were applied. The final logic unit in the pretrigger determined whether or not there was enough p_T in the event to justify checking the trigger level. If there was, a PRETRIGGER strobe was issued. The PRETRIGGER strobe initiated the EVENT sequence, latching the data in both the tracking system and LAC electronics.

4.3.2 The Trigger

Finally, with all other signals satisfied, a trigger level still needed to be chosen. There were 3 different categories of triggers, low-level (heavily prescaled) beam and interaction triggers, local triggers, and global triggers. Local triggers were generated if the p_T within a preselected set of 16 strips in an octant was above a given threshold. The global triggers required the sum of all strips in a given octant be above some specified threshold. These thresholds were adjusted

throughout the run to give satisfactory trigger rates for various beam conditions. Table 4.1 below provides the trigger settings as they were at the end of the 1990 run.

Trigger	Trigger Fraction	Prescale Factor	Threshold
Single_Local_Hi	40%	1	3.5 GeV/c
Single_Local_Lo	18%	40	3. GeV/c
Local_Global_Hi	35%	1	3. GeV/c
Local_Global_Lo	20%	40	2.5 GeV/c
Two_Gamma	20%	1	2.8 GeV/c
Interaction	3.1%	15^5	none
Beam	2%	15^6	none
Prescaled Pre.	7%	15^5	none
Di-Muon (E672)	20%	1	$\approx$ 1 GeV/c

Table 4.1 Trigger thresholds used at the end of the 1990 run

Using the GLOBAL, LOCAL, and PRETRIGGER signals, a number of LAC based triggers were formed. E706 had nine distinct experimental triggers: Prescaled_Beam, Prescaled_Interaction, Prescaled_Pretrigger, Single_Local_High, Single_Local_Low, Two_Gamma, Local_Global_High, and Local_Global_Low. Below is a description of how the requirements for the principal triggers above were formed.

4.4 Trigger Types

Single_Local — Defined by the Local_Pt_High signal was the simplest trigger and the main staple of this experiment. This trigger indicated when a large amount of p_T had been deposited in a small region of R within a single octant. This trigger was very efficient in detecting single photons and π^0 decays.

Local_Global — Defined by a logical AND of the Global_Pt_High/Low and the Local_Pt_Low logic signals. This trigger indicated that a large amount of p_T had been deposited in an octant with at least some reasonable amount localized to a small radial region contained in that octant.

Two_Gamma — Defined by the logical AND of the Local_Pt_Low signal from one octant with the Local_Pt_Low signal from any of the three octants opposite it in the EMLAC. This trigger was designed to study massive two photon decays, ψ decay, Drell Yan production, as well as multiple π^0 production.

For diagnostic and alignment purposes, triggers were also defined using just the beam and interaction definitions. These triggers were heavily prescaled to prevent them from dominating the data rate. They provided an unbiased class of events with which to perform checks as well as to study low p_T particle production.

Once a trigger was satisfied, a signal was sent to the data acquisition system and the event was recorded to tape. Further triggers were blocked at this point until the data acquisition had completed its readout. If a PRETRIGGER signal

had been issued, but no trigger was satisfied, a reset signal was broadcast to all crates to re-enable the electronics for the LAC and tracking system.

Chapter 5 Event Reconstruction

5.1 Structure of MAGIC

The E706 software analysis package for event reconstruction was centered around MAGIC, a program written specifically for E706 by G. Alverson of Northeastern University. MAGIC provided the framework for event reconstruction. This program, as well as all of the individual reconstructors, employed the ZEBRA [31] memory management package developed at CERN.

MAGIC was a steering routine which controlled all of the data unpackers and event reconstructors. MAGIC's first task was to read the data. MAGIC was capable of reading in initial (raw) data, unpacked data, or fully reconstructed output. The data could have originated from the data acquisition system or have been generated by the Monte Carlo programs.

Once read in, the data was sorted and written to memory in a form that was both "logical" and meaningful. For instance, tracking data was converted into hits for a particular plane, while LAC data was stored as pulse heights for each EMLAC channel subdivided by quadrant, section, and view. A separate routine unpacked the data from each component of the spectrometer.

There were five principal reconstructors used in the first pass analysis package; one for the trigger and Cerenkov, one for the electromagnetic LAC, one for the hadronic LAC, one for the tracking system, and one for the forward

calorimeter. Each of the reconstructors operated on the data independent of one another. The electromagnetic shower reconstructor, for example, did not use any tracking information to aid in distinguishing photons from electrons or to assist in shower correlations. This decision was made primarily to simplify the coordination of the coding efforts.

The major routines used in this analysis were DLREC, EMREC and PLREC. DLREC was responsible for managing all of the bits encoded from various discrete logic units such as those involved with the latched trigger and Cerenkov counter. PLREC reconstructed track information from the SSD's and PWC's, and STRAW's. The results from this routine were the vertex position of the event, the momentum of each of the tracks in the event, and the respective charge of the particle associated with each each of the tracks. EMREC correlated single view "gammas" to form photons, evaluated their position and determined the energy of each shower in the electromagnetic calorimeter.

By design, MAGIC is a very flexible program. Through the use of various software "switches", routines within MAGIC could be "activated" or "deactivated". For example, if only electromagnetic shower information was desired, the tracking and trigger processing could be deactivated, saving considerable processing time. Entry points at logical breaks in the processing code allowed the user to quickly customize programs for specific needs. Furthermore, the data could also be unpacked but not reconstructed, a feature which was found to be very useful for hardware and calibration studies.

To reconstruct the data used in this analysis, the MAGIC package was run on several of the Fermilab parallel processing computing clusters located in the Feynman Computing Center. These computational sites were commonly referred to as "farms". The farms were a rather simple way to achieve large scale parallel processing. One computer on each farm was responsible for the input and output functions. This IO node read the input raw data from a tape and distributed ("farmed") single events to each of the processing ("worker") computers. A copy of the entire event analysis software resided on each worker node. Each local node processed its own events from unpacker to reconstruction. A worker node, when finished with an event, passed the reconstructed event back to the I/O node where the results were written out in final form, either to disk or to tape. The worker node would then be given a new event to be processed.

On E706, we had up to 6 computer farms at our disposal. Several of these farms utilized Silicon Graphics RISC based computer engines. These farms contained, on average, 10 worker nodes and one I/O node. The remaining farm contained IBM UNIX hardware and consisted of a single I/O node and 7 worker nodes. Although each of the farms had slightly different hardware configurations, they provided comparable performance. Experimental data was processed exclusively on the Silicon Graphics farms. The Monte Carlo event generation program had the flexibility to run on either hardware platforms. Typically, the Monte Carlo occupied 3 farms full time, and depending on the demands of the data reconstruction effort, was also run on the other farms to fully utilize the available resources.

5.2 Electromagnetic Reconstruction Program (EMREC)

The electromagnetic reconstruction program determined the energy and position of the incident photons in the EMLAC using the ADC values recorded from the various strips in the detector. Two major operations were required on the data in order to achieve the ultimate goal of photon identification. First, the raw data has to be unpacked and arranged in a way that is useful for the reconstructor to operate. Second, the EMREC reconstructor utilizes the energy distributions provided by the unpacker to identify showers and ultimately photons.

5.2.1 Unpacking

The data as provided from the data acquisition system was in raw form. The information arrived at the unpacker in the order of RABBIT crate, amplifier, and channel. The unpacker sorted this data and arranged it in an order that was more suitable for analysis. Each of the quadrants of the EMLAC was treated as an independent entity during the reconstruction process. A quadrant was organized into sections and views. The 4 views of a quadrant were left R, right R, inner ϕ and outer ϕ. Each view had 3 sections; front, back and sum. The sum section is just the sum of the front and back sections. The unpackers first job was to convert the raw datum from ADC counts into detected energy. This was done based on the formula:

$$e_i = A_{em} \times G_i \times (N_i - No_i) \qquad 5.1$$

- N_i was the digitized value of the pulse height in channel i.
- No_i was the pedestal for channel i.
- A_{em} was the normalization as determined by electron data.
- G_i was the gain of channel i.

A pedestal was the value a particular amplifier channel recorded for a specific detector location in the absence of a shower in that vicinity. A separate and unique pedestal value was determined for every channel in the LAC. These pedestal values were relatively stable over long periods of time. However, temperature changes in the Faraday room, spill intensity, and hardware changes caused the pedestals to shift by several counts. Great care was taken to determine the appropriate pedestal values. The initial pedestal values were determined approximately once every eight hours during the data acquisition process as part of the LAC calibration tasks. (see section 3.7) An EVENT sequence was sent from the ICBM's to each crate before run startup and between accelerator spills. Each amplifier channel was read 128 times and the resultant average was passed back to the ICBM where the values were stored in a pedestal file keyed by run number. These values, although a good starting point, were not entirely satisfactory. Minor channel to channel variations still needed to be removed.

To remove these channel to channel variations, beam triggers from data runs were examined off-line. Channels that contained showers were removed from this analysis and the remaining "on-line" pedestal readings were then

gathered and averaged over the course of a 60,000 event run. These average values were used off-line to correct the original pedestal files, and removed most of the channel to channel variations. These corrected pedestals provided a stable baseline for approximately 8 hours. Although time consuming, this process of off-line pedestal determination resulted in run to run pedestal variations of less than 2 ADC counts [32].

The gain term in equation 5.1 has two components. The first part was the actual channel gain determined by the gains calibration task as described in section 3.7. The second part was a multiplier used to adjust for the observed time dependent response of the LAC.

Figure 5.1 shows a plot of the uncorrected π^0 mass as a function of time. This energy scale change over time was substantial – the uncorrected π^0 mass changed by close to a factor of 2 over the 6 month 1990 data run. The time unit "beam days" used in this plot requires some explanation. Beam days were those days in which beam interacted in the experimental hall. For example, two adjacent data runs separated by a 5 physical day shutdown of the accelerator would be plotted as consecutive beam days. For intervals directly surrounding accelerator downtime, no change in the π^0 mass was observed. Hence this effect was directly associated with the particles striking the calorimeter. At this moment, no satisfactory explanation as to the cause of this dependence of the energy scale upon beam exposure has been identified.

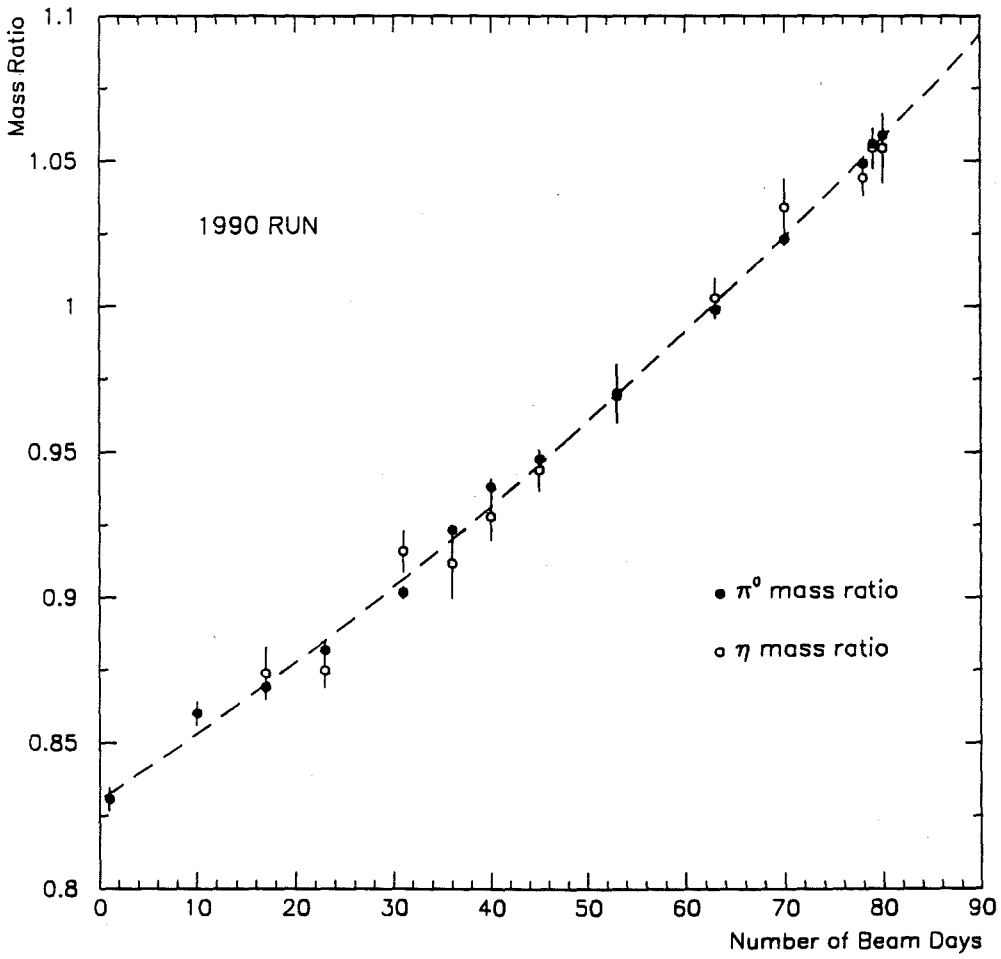

Figure 5.1 Uncorrected π^0 mass as a function of time for the 1990 run.

This mass dependence was parametrized and the final energy scale correction was modified appropriately through the gain term. This correction was evaluated on a run by run basis based on the start time of each data run. It should be noted that this correction to the gain term does not set the final energy scale. Its sole function was to eliminate the variation in the energy scale so that reconstruction thresholds would be nearly constant throughout the processing of this data. The final energy scale determination will be discussed at length in a later section.

5.2.2 FREDPED – Pedestal Adjustments on an Event by Event Basis

The underlying pedestal values for the EMLAC channels determined once every 8 hours or so were insufficient for determining the best estimate of the actual energy deposited in an event. Local variations in beam intensity created artificial "ramps" and "steps" in the R and ϕ views of the EMLAC for some fraction of events in a given run. The degree to which this was a problem varied depending on the instantaneous conditions in the Tevatron. Ignoring these event by event shifts in the pedestal values would have resulted in a small systematic misrepresentation of the energy in that event, miscorrelations of the R and ϕ "gammas", and either the creation or omission of other "gammas" altogether depending on the direction of the slope.

FREDPED, a subroutine called just prior to final event reconstruction, was written to address this issue. FREDPED identified all channels which were thought to contain information pertaining to showers. The remaining channels

were then fit to a function. The resulting fits could be of the form of a line, an overall offset, or else a step. A new set of pedestals for this event were calculated based on the above fit. The energy in each channel was then corrected accordingly.

5.2.3 Shower Reconstruction

The electromagnetic reconstruction routine searched for clusters of energy in the R and ϕ views separately. The first stage of reconstruction was to find all of the locations of energy deposition in each quadrant. These locations were called groups. A group was defined as at least three adjacent strips (two in outer ϕ) which contained energy above a constant specified threshold. These groups defined the locations in the EMLAC which potentially contained electromagnetic showers.

Next, the peaks were identified within each group in the summed section. A peak is the point at which the derivative of the energy distribution changes from positive to negative. Each peak was located between two valleys. Valleys were either the low point between two peaks or, in the case of single peak groups, the end strips of the group. The position of each peak was calculated using the three central strips, including the peak strip. Once a peak was identified in the sum section, the peak finding algorithm was then reapplied separately to the strips in the front and back sections. It is possible that what appeared as a single peak in the sum section could be the result of two nearly overlapping peaks as observed in the front section. If coalescence had occurred in the sum

section, then the energy of the original peak was divided among the two new peaks with the positions and relative energies determined by the peaks observed in the front section. (See Fig. 5.2.)

From these peaks, single view photons or "gammas" were then formed. For single peak groups, this was just a matter of fitting a parametrized shower shape to the peak and using the integral of this function to determine the energy of the "gamma". However, for multiple peak groups, it was not quite so simple. Here the energies of the partially overlapping gammas were determined by the minimization of χ^2.

$$\chi^2 = \sum_{i=1}^{m}(1/\sigma_i^2 \times (e_i - \sum_{k=1}^{n} E_k \times f_k)^2) \qquad 5.2$$

where f_k was the fraction of the energy from shower k that would be deposited in strip i based on the parametrized shower shape. The term σ_i is the error on the fit for each strip. This minimization was explicitly solved for the individual shower energies E_k. The energy distribution for each individual shower was then found by subtracting the contribution from all the other showers in the group. For R gammas, an attempt was made to find the position in both the front and back sections. This information was used to determine a particles incident direction, which will prove useful for muon rejection in this analysis. This technique of measuring a particles "directionality" was used in this analysis as one technique to eliminate the muon background. It will be discussed at length in Chapter 7.

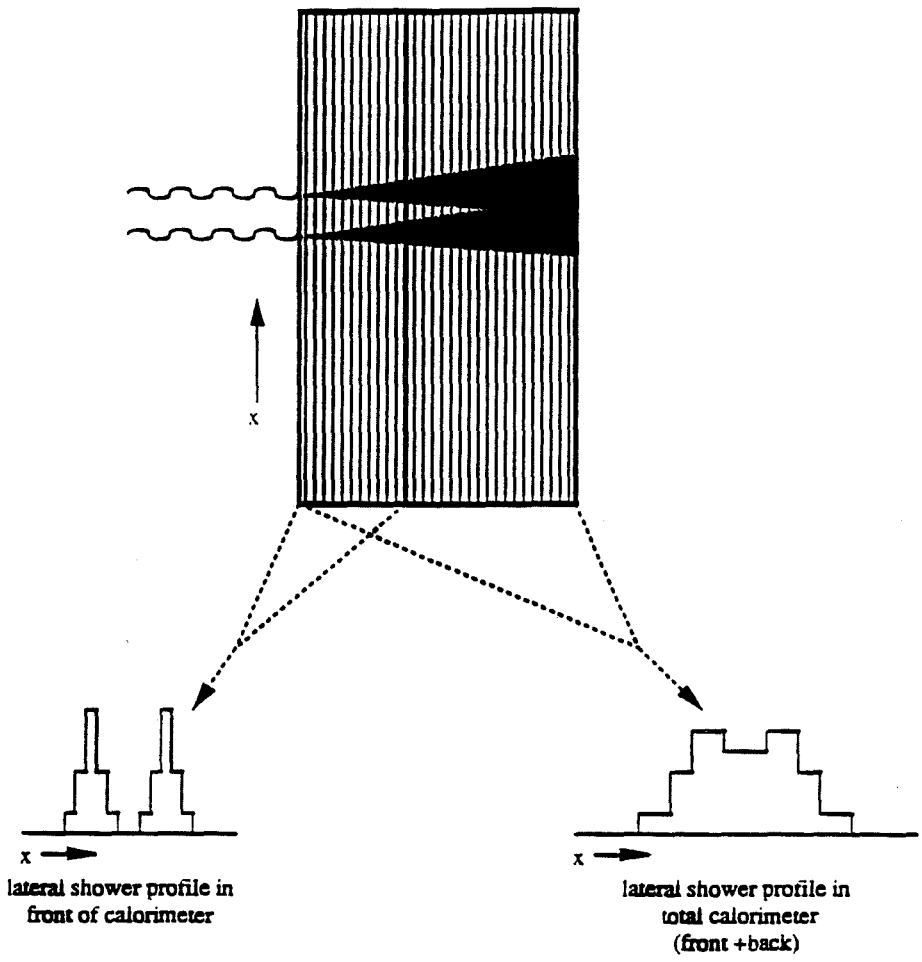

Figure 5.2 The front back separation was used to aid in di-photon separation. Showers in the front section will have a narrower profile than do those in the back. This can help resolve two closely spaced photons which would otherwise have coalesced.

5.2.4 Correlation of "Gammas"

The final stage of reconstruction correlated the "gammas" (single view showers) from R and ϕ views to reconstruct the final photons. Naively, this is done by matching "gammas" from each view based on energy. However, confusion may occur when there is more than one shower in the same view with similar energy. Complications also arise due to showers near the edges of views and to the cell structure of the LAC. The matching between "gammas" is done independently for the R and ϕ views in the front section and in the back section. The total energy and longitudinal energy profiles were similar for both the R and ϕ views in the sum section, but were not so similar in the separate front and back sections.

For electromagnetic showers, most of the energy was deposited in the front section. Therefore, in the back section, deposited energy monotonically decreased as a function of its depth in the calorimeter. This was not true in the front section. Here, the shower developed to a maximum energy before decaying as a function of depth in the calorimeter. The first readout board in the back section was an R board. Due to the decreasing energy distribution in the back, the first back R board generally collected more energy than the first back ϕ board. Hence, for the back section, $E_R - E_\phi > 0$. For the sum section, the two energies balanced so that $E_R - E_\phi \approx 0$. It then follows that for the front section $E_R - E_\phi < 0$. Thus, the correlation routines incorporate an adjustment to accommodate this difference in R and ϕ view energies observed in the front and back sections.

The correlation algorithm used, as matching criteria, the above weighted energies as well as E_{front}/E_{total} distributions. The process of correlation was conceptually simple but was complicated by the fact that the physical detector had boundaries and finite resolution. A shower which landed on the inner/outer ϕ boundary was often reconstructed as two separate gammas. These two gammas had to be reconciled if correlation was to proceed correctly. Similarly, a single shower which occurred near an octant boundary was not only split into two separate gammas but there was also a possibility of some energy loss as a result of the boundary. This lost energy had to be estimated and taken into account to insure proper correlation. About 80% of the electromagnetic showers were handled by 20% of the correlation routines [33]. The remaining routines were written to handle all of the special cases. It was these routines that determined the reconstructor's efficiency. The final photon energy was the unweighted sum of the fit energies of the R and ϕ "gammas".

5.3 Shower Shape

Shower shape information, as noted above, was needed to extract the position and energy of any single "gamma" from a group of several overlapping showers. The individual shower shapes were rederived for the 1990 data. It was unlikely that the shower shape changed between the 1988 and 1990 runs, but the readout system of the LAC did. With the elimination of zero suppression of the LAC data in 1990, the tail energies which were previously unknown could now be incorporated into these fits. The shower shape was fit to the form

$$E_{front}(r) = \frac{1}{r}\left(f_1 e^{-f_2 r} + f_3 e^{-f_4 r} + f_5 e^{-f_6 r}\right) \quad 5.3$$

for the front and

$$E_{back}(r) = b_1 e^{-b_2 r} + b_3 e^{-b_4 r} + b_5 e^{-b_6 r} \quad 5.4$$

for the back.

Here, r is the radial distance from the shower center. The fitted parameters f_{1-6} and b_{1-6} are listed in a Table 5.1. The factor of $1/r$ was used in the front section to fit the steep r-dependence of the shower. The shower was broader and more developed in the back section so that the $1/r$ term used to sharpen the front shower shape was unnecessary here. The parameters f_1, f_3, f_5, b_1, b_3, and b_5 were normalized at the initialization of EMREC such that the integral of the shower shape was equal to 1 GeV. The sum section shower shape was then determined by combining the front and back shower shapes as follows

$$E_{sum}(r) = E_{front}(r) + (1 - P_{52})E_{back}(r) \quad 5.5$$

where P_{52} is a front to back energy weighting whose value was 0.70.

It was found that the shower shape generated using a GEANT full shower simulation matched the shower shape derived from isolated photons in the data very well. A full shower in Monte Carlo terms means that the shower was allowed to develop and its constituent particles were allowed to undergo all physics processes until the energy loss was sufficient that that particle was stopped in

Front	
f_1	0.49298
f_2	1.2163
f_3	0.03141
f_4	0.30934
f_5	0.53628
f_6	10.0071

Back	
b_1	0.04257
b_2	0.43745
b_3	0.32951
b_4	1.3606
b_5	2.5412
b_6	5.8467

Table 5.1 The parameters used in EMREC to fit the 1990/1991 shower shape.

some material. Since the Monte Carlo offered a tool for a more controlled study, the fit to shower shape itself was determined using Monte Carlo data from single photons hitting the center of octant 1 at R=60cm. Care was taken in the Monte Carlo to insure that the photons striking the LAC were evenly distributed across several strips. The shower shape was sensitive to the position of the center of the shower with respect to the central strip in that shower.

The Monte Carlo shower shape used to determine the fit values was an average shower shape derived from approximately 2000 separate single photon events. This shape was determined by plotting the energy observed in each strip in a shower as a function of the distance of the center of that strip from the shower center. Using these 2000 events, an average shape emerged that was much smoother than the width of the physical readout strips.

The shower shape parameters shown in Table 5.1 were determined from 22 GeV showers. An average shape was determined in both the front and back

views separately. This shape was then fit using the above expressions. The parameter P_{52} was determined to be 0.70 by looking at the E_{front}/E_{total} ratio for these events.

A series of 1000 event Monte Carlo runs with photon energies of 4, 9, 17.5, 22, 35, 50, 70, and 120 GeV were generated to check for any dependence of the shower shape on photon energies. This sample struck the center of octant 1 near R=60 cm. The above shower shape was then used to calculate the fitted energy using EMREC. Figure 5.3 shows the ratio E_{fit}/E_{gen} as a function of the generated energy. E_{gen} is the input energy to the Monte Carlo. E_{fit} is the resultant energy determined using the above shower shape. The result is flat to within 1.3% over this wide energy spectrum and demonstrates that this shower shape is nearly independent of energy.

5.4 Photon Timing using TVC's

The response of the EMLAC was on the same timescale as the average time between interactions. It was therefore useful to establish the arrival time for showers so that out of time particles that hit the LAC either before or after a trigger signal could be identified and rejected. This was done using time to voltage converters (TVCs) within the LAC amplifier modules.

These TVC's worked by measuring a voltage proportional to the time between the beginning of a LAC pulse and the BEFORE pulse. Specifically, each TVC circuit was sensitive to the amount of charge deposited in four adjacent

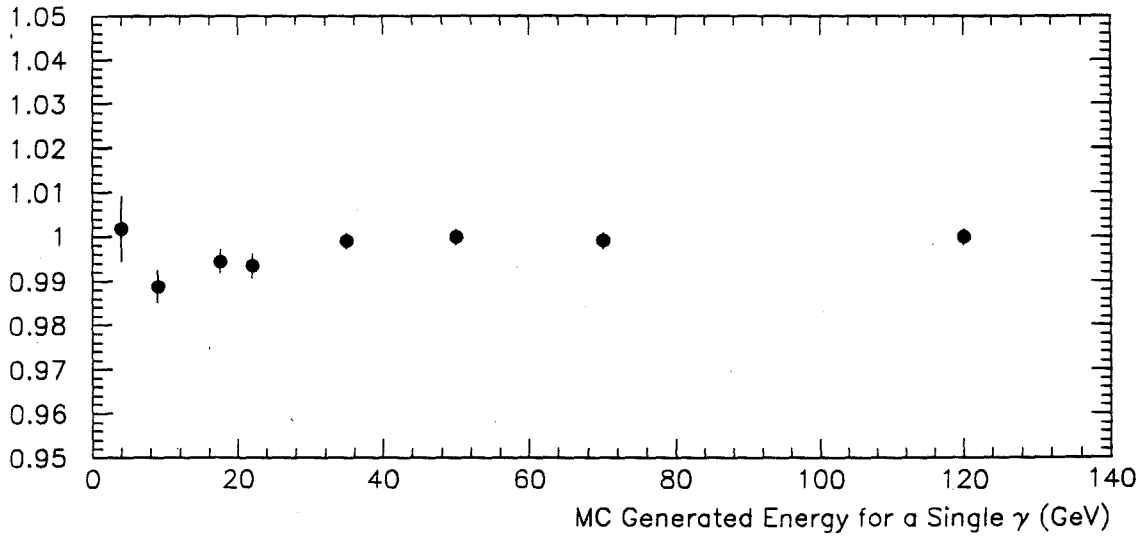

Figure 5.3 Stability of the shower shape to photon energy. The ratio of the reconstructed energy to the generated energy is plotted versus the generated spectrum. The flatness of the curve indicates that the shower shape does not change with the energy of the incident particle.

strips on a single amplifier. This signal was differentiated to reduce the effect of pickup noise, and then compared to a crate-wide threshold. If the signal was above threshold, then the resulting logic signal started a timing circuit. With the timing circuit open, charge from a current source was collected on a precision capacitor. The circuit was closed if, and when, the first latch signal (BEFORE) arrived. The time between a particles arrival at the calorimeter and the trigger signal then was simply proportional to the amount of charge collected on the capacitor.

The full scale time of the TVC was determined by fixing the value of the capacitor and the current flowing into it. A 1.5 μs ramp was selected to accommodate the 800 ns delay line inside the amplifier while allowing a sufficient window of time to check for the arrival of a data pulse before or after the triggered pulse. This ramp was long enough that there was a slight chance that a second pulse could arrive during the time in which the capacitor was ramping up. To minimize dead time, the timing circuit included a second collection circuit which was activated when the first circuit was busy. The first timing circuit was referred to as the "Master" and the second as the "Slave." The TVC circuit worked like an ordinary stop watch except that it was based on a common stop rather than the somewhat more intuitive common start method.

5.4.1 TVC Calibration

The goal of TVC calibration was to facilitate comparisons of TVC values from event to event among various locations in the LAC. Calibration allowed

each of these TVC circuits to be normalized to some standard by which comparisons could be made.

The calibration data consisted of a pedestal or "zero time" value as well as a gain measurement. The gains of each TVC was found to be extremely stable over time. The TVC pedestal measurements were less stable. A preliminary data base of TVC pedestal values was updated approximately once every eight hours during the data acquisition process as part of the LAC calibration tasks.

To accomplish the TVC calibration task, a timing curve for each TVC channel was produced. Two pulses, approximately 300 ns apart, were injected into each channel; one fired the Master TVC, the other the Slave. The position of the first latch, or BEFORE gate, was then varied relative to this signal, and the resultant TVC values were read out and stored locally on the ICBM handling each crate. These points were then fit to a line. The slope and zero time (Y intercept) were determined and stored in the run constants data base on a computer for each TVC. The pedestal was then determined from the summation of the Y-intercept value and the intrinsic ADC offset. The problem with this method was that the intrinsic ADC offset was different and unknown for each TVC. A single offset or an average offset per crate yielded unacceptable time resolution. An alternative method of using the data to determine the pedestal values off-line was thus employed.

Off-line Analysis Method

In this alternate approach, pedestals were determined by examining each individual TVC's behavior over the course of specially selected data collection runs. A series of cuts were placed on the data to insure a high probability that the energy depositions in the LAC were associated with the triggering particle and thus in-time (with the trigger).

The criteria for participation in TVC pedestal determination were:

1.) The energy in the 4 adjacent strips associated with the TVC circuit must be larger than 4 GeV to insure that the TVC was not reading some noise fluctuation.

2.) The TVC value must fall within two sigma of the nominal design value for in-time. Thus, the TVC must have a value between 30000 and 38000 ADC counts.

TVC values satisfying the above criteria were read out and averaged over the course of a 60,000 event run. These average values were then stored in a database as the new TVC pedestal values.

This off-line pedestal technique resulted in timing resolution of 7ns as illustrated in figure 5.4. This was well inside the 19 ns bucket structure of the accelerator. These TVC pedestals were found to be stable to within 0.5 ns over approximately 48 hours.

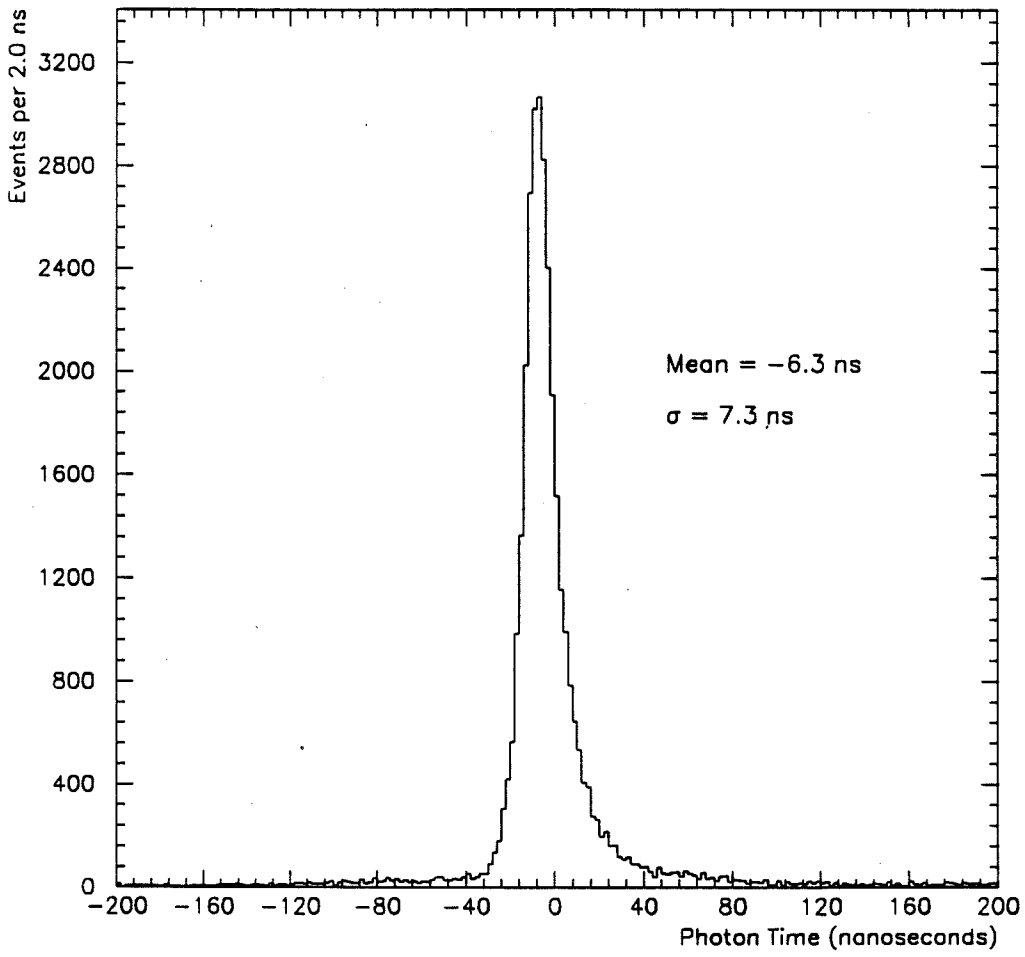

Figure 5.4 The timing resolution for photons.

5.4.2 Assigning Timing Information to the Photons

Timing information was assigned in EMREC at three separate stages; peaks, "gammas", and photons. At each level, timing information was derived from all the available data and not from the results of the previous reconstruction step. For example, the time of a photon was determined by going back to the all the raw TVC information that was pertinent to that photon. It was not found by averaging the time derived for the R and ϕ "gammas."

Timing information for a "gamma" was determined as follows. First the TVC reconstruction program determined the strip boundaries for a given "gamma" from EMREC. The TVC banks corresponding to those strips within the "gamma" were examined and a candidate list of possible Master and Slave times was generated. For instance, a "gamma" 20 strips wide for instance may have time measurements from 5 to 7 separate TVC timing circuits with each TVC circuit containing information in both the Master and Slave channels totalling 10 to 14 possible values.

Times within this candidate list were grouped into clusters of similar values. The time associated with a "gamma" was determined from the cluster with the largest number of similar time entries. The actual time assigned was an energy weighted average of the values contributing to this cluster. When there were two or more clusters with the same number of contributors, the cluster associated with the largest strip energy was selected. Again, the actual time

value associated with the cluster was an energy weighted average of the times inside the cluster.

A photon time was determined in exactly the same fashion as a "gammas" time discussed above. Rather than averaging the time found for the R and ϕ "gamma", the algorithm was rerun treating times associated with R and ϕ views equally. This was done in order to avoid problems which arise when one "gamma" had either no time assigned to it or else had a time which was triggered on electronic noise rather than signal. For each "gamma" and photon, the "best" or most common time value as well as the second most common value were stored. The TVC efficiency curve for photons shown in Fig. 5.5, indicates that the turn-on point for this device is 16 GeV and that the TVC's become fully efficient at photon energies exceeding 50 GeV.

A quality word associated with each derived time was also calculated and stored for both the "gammas" and photons. This quality word had three components, a Master/Slave indicator, the average energy of TVC groups that fired inside this cluster, and the number of TVC entries which participated in the cluster.

5.5 Discrete Logic Tracking Program (DLREC)

The trigger logic and Cerenkov detector information was reconstructed inside DLREC (Discrete Logic REConstructor). The trigger information consisted of bit-packed data containing information about whether a veto wall

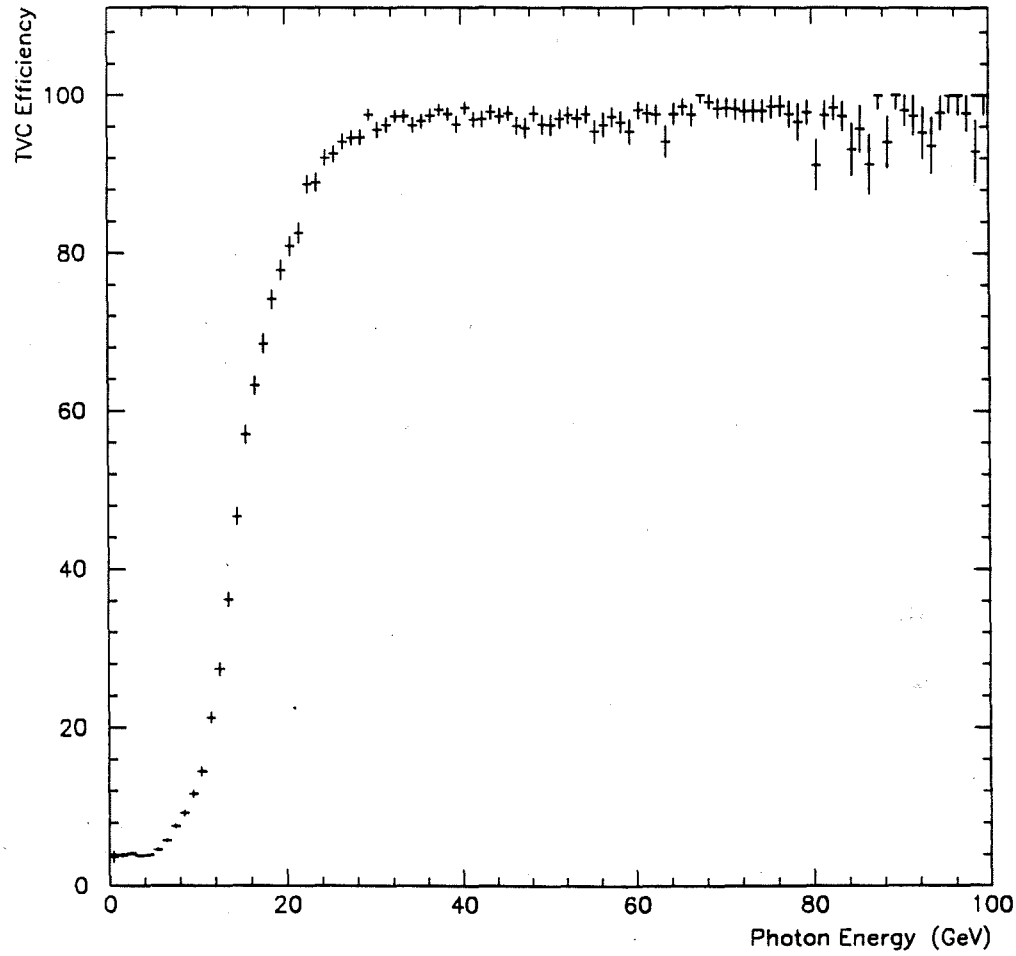

Figure 5.5 The TVC efficiency curve for photons.

element, hodoscope element or interaction counter fired for a particular time bucket as defined by the accelerator clock.

A local time history of the status of many counters in the experiment was latched and read out using a device known as the "Minnesota Latch". This device kept a time history of what happened for seven 19 ns buckets on either side of the trigger — a total of 15 buckets. The latched information included the status of beam counters, interaction counters, the hodoscope elements, the Cerenkov phototubes, the veto walls, and the hole counter. This information allowed us to reconstruct in the software details regarding the trigger scheme and what occurred in the devices just prior to and just after a trigger was accepted.

DLREC also kept track of which local p_T fired, which octant or octants satisfied the trigger requirement, and which trigger type was satisfied.

5.6 Planes Reconstruction Program (PLREC)

The tracking devices recorded a series of hits along the trajectory of a charged particle in response to that particle's passage through the system. The planes reconstructor, PLREC, used the hit information from the various planes of SSD's, PWC's, and Straw Tube Drift Chambers to reconstruct the particles path through this section of the spectrometer. The PLREC software package followed an 8 step process in order to untangle this hit information into useful tracks. These steps were, in order of their occurrence; beam tracking, downstream PWC tracking, straw tracking, upstream tracking, linking of the

upstream and downstream tracks, primary vertex reconstruction, relinking, and finally secondary vertex reconstruction. Using the magnetic field and the angle between the track upstream and downstream of the magnet, the momentum and sign of the charged particle were calculated. What is given here is merely an overview of how the planes reconstruction system works, the subject is treated extensively elsewhere [34].

5.6.1 Beam Tracking

Beam tracks in both the X and Y views were found using the SSD planes upstream of the target. The beam tracks record the incident beam particle's direction just prior to its passage through the target region. Beam tracking was done in two passes. First, identify the three hit beam tracks. Then, after removing from further consideration, the hits from those tracks, find the remaining two hit tracks. Three hit beam tracks were identified by connecting hits on the first and third planes in each view. The middle chamber was then examined for a hit within 75 microns of this projected line. If a hit was found in this plane and the χ^2_{NDF} (per number of degrees of freedom) value for this candidate track was less than 3.0, a three hit beam track was made and the corresponding hits were marked accordingly. Once this process exhausted all possible three hit combinations, two hit beam tracking was done using the remaining hits.

These beam tracks were used at various points in the tracking algorithm when certain difficult or ambiguous situations arose. For example, an event

with very low track multiplicity might contain a primary vertex with only two charged tracks. This candidate vertex was kept only if a beam track pointed to this vertex. Furthermore, a stiff track in the downstream SSD system was not used in the vertex determination if a beam track pointed towards that track.

5.6.2 Downstream PWC Tracking

The PWC system consisted of 4 chambers, each containing 4 separate views (X,Y,U,and V). The final downstream tracks were identified in PLREC through a multi-stage process. First, view tracks were identified in X,Y,U, and V independently. The X,Y view track pairs were then combined to determine candidate projections onto the U and V views. The U and V views of these candidate tracks were then searched for hits which lay within some small distance of the projection. If enough hits were found in the U and V view, then a "space track" candidate was identified. A space track is a correlated set of view tracks which define a particle trajectory in 3 dimensions. The space track candidates were then subjected to a set of cuts; those which survived uniquely identified the corresponding three dimensional trajectories.

The space tracking was carried out in PLREC in 3 distinct stages. The details of the space tracking follow.

Stage 1

All of the hits in the PWC system were examined to identify the tracks in each of the 4 views – X, Y, U, and V. In each view, lines were projected between

hits in the first and last plane. Then, for each line, the second and third planes were searched for hits within 1 wire space of the predicted position. A view track was stored if it contained a total of 3 or more hits. Once all 4 hit (and 3 hit with sharing cuts on 4 hit tracks) were identified in each of the four views, space tracking was attempted.

Space tracking was done by pairing each X-view track with a Y-view track and then searching the U and V planes for hits within 1.5 wire spaces of the position predicted by the X/Y pair. Space tracks which survived stage 1 contained 13 or more hits with a minimum of 2 hits in each view, and had a χ^2_{NDF} less than 3.0 for 14, 15, and 16 hit tracks, and a χ^2_{NDF} value less than 2.0 for 13 hit tracks. The identical procedure was also done at this stage where tracks were formed in the U and V planes, and candidate hits were searched for in the X and Y planes.

Stage 2

All of the hits from the high quality space tracks which were found in stage 1 were removed from the pool of candidate hits. Stage 2 was implemented to identify tracks which were missed as a result of sharing cuts, spectrometer acceptance, and low hit multiplicity. The procedure for finding tracks in stage 2 was the same as in stage 1. View tracks were formed using the remaining hits. Space tracking was then attempted with this new set of view tracks. The only difference in the algorithm from stage 1 was that the number of hits required to

form a space track was reduced to 10 hits for three modules and 11 hits for four modules.

Stage 3

This was the "clean up" stage which primarily handled two module tracking. This stage found the tracks that were clearly visible in the first two modules but had trajectories which left the acceptance of the spectrometer. The criteria for finding a space track in Stage 3 were: a minimum of 6 hits for a space track, the track must point back to the target in the Y view, and the space track had to be outside the acceptance of module 3 in the X view.

5.6.3 Straw Tracking

The second phase of the downstream tracking was to incorporate the straw tube information into the space track banks. The straw tracking algorithm was complicated. It consisted of four loops with three separate iterations per loop. The straw tracker made use of the PWC tracking information to "seed" its algorithm.

Step 1.

Each PWC space track was projected into both straw chambers. If enough straw hits were located within 3.5 mm of the PWC projection for both upstream and downstream straw chambers, there was a possibility of making a straw track. Those hits within this projection, along with their left/right ambiguous partners, were written out with the PWC track information to a temporary array. (The

left/right ambiguity stems from the fact that there is no a priori information to indicate on which side of the wire the ionized electrons originated.) There was no sharing of straw hits among different PWC tracks in any given loop – as soon as a straw hit was used, it could not be used a second time.

The temporary array derived above was examined. If there was a minimum of 4 hits in each straw chamber with at least 2 hits in each X and Y view associated with a given PWC track, then the straw hits alone were refitted and a χ^2 value for this fit calculated. The hits due to the left/right ambiguity were also tried in the fit and the points chosen for the final fit in this step were those which yielded the smallest χ^2 value. At first glance, this looks like rather stringent criteria, but it should be recalled that each straw chamber had 4 layers of X tubes and 4 layers of Y tubes.

Step 2.

This new fitted line was then projected into both straw chambers. The search window was reduced to 1.3 mm. The closest straw hits to the new projected line inside of this smaller window were once again loaded into an array along with their left/right ambiguous partners. The criteria of 4 hits in each module with a minimum of 2 hits in both X and Y view was again imposed. If this criteria was satisfied then these points were refit. The ambiguous partners were also incorporated and the final points selected minimized the χ^2 value for this fit.

Step 3.

This iteration was done a third and final time with a projection window size of .8 mm. The same 4 hit criteria was imposed with a minimum of 2 hits in both the X and Y views along with a χ^2_{NDF} cut of less than 3. At this point we expect to converge on the solution. If a set of straw hits survived the cuts in all 3 steps then the solution was declared a straw track and the first loop of the straw tracking algorithm was completed. Straw tracks which survived this first loop were tracks of the highest quality.

The hits which comprised the above high quality straw tracks were then removed from the list of candidate straw hits in preparation for loop two. Loop two proceeded with this reduced hits list and the same three steps as above but with one significant modification. Instead of requiring 2 hits in both the X and Y view as was done in the first loop, this loop required a minimum of 4 hits in each module, where one view could contain a single hit. Hits that survived the three iterations in this loop were also identified as straw tracks.

5.6.4 Upstream Tracking and Linking

View tracks were reconstructed based upon the hits detected by the X and Y view SSD wafers downstream of the target. Because there were no rotated planes in this system, there were no equivalent "space tracks" formed as was done in the downstream PWC system. Thus, the tracking in the SSD system consisted solely of finding tracks in the X and Y views.

First, all 5 and 4 hit X and Y view tracks were found by connecting hits in various pairs of planes. Each candidate track was projected into the remaining 3 planes. These planes were then examined for hits located within 75 microns of this projection. Those SSD view tracks which included 4 or 5 hits were then projected to the center of the magnet. The PWC/Straw tracks for this event were also projected to magnet center. An SSD track whose mid-magnet projection was within a momentum dependent window of the PWC/straw track was then "linked", or associated with that PWC/straw track. For a high momentum PWC track, the size of this linking window is about 4.4 mm and for a high momentum straw track the window is 2.0 mm. Up to five SSD tracks could be linked to a single PWC track. By using this technique of linking SSD view tracks to PWC/Straw space tracks, we were able to create effective "space tracks" in the upstream system. The closest SSD track to a PWC track was referred to as the "best linked" space track.

The list of available hits in the SSD system was then "cleaned." All of the hits from the linked SSD tracks were removed from the list of available SSD hits. The hits from isolated SSD tracks were also removed from the list of available hits. View tracking was then redone in both views, this time allowing three hit tracks. These additional view tracks were then linked to the PWC/straw tracks.

5.6.5 Primary Vertex Reconstruction

Vertices were reconstructed in each view using the SSD tracks. Initially, only the linked 3, 4, and 5 hit tracks were used as candidates to find the primary

vertex. Those tracks identified in the SSD system as "straight thrus" which travel parallel to the beam both before and after the target and whose slope and intercept matched in both systems, were ignored. A χ^2 was defined for a given vertex position by

$$\chi^2 = \sum_i b_i^2/\sigma_i^2 \qquad 5.6$$

where b_i is the impact parameter of the ith track relative to the vertex position, and σ_i is the uncertainty in the projection of the track. The vertex position was determined by minimizing this sum in each view. This minimization was first performed in the Y view. One by one, the worst track was removed and a χ^2_{NDF} contribution was recalculated until either the χ^2_{NDF} value for the vertex was less than 5 or the χ^2_{NDF} value of the worst remaining track was less than 9. Once either of these two conditions was satisfied, a vertex position was identified for this view. The identical process was then performed in the other (X) view. The overall vertex position in Z was taken as the weighted average of the Z positions of the vertex in each of the views.

All of the tracks used in reconstructing this vertex were then removed from consideration and the entire process was performed again using the remaining linked tracks to attempt to find another vertex. If a second vertex was found, which was matched in Z between X and Y views, the one labeled as the primary was the one most upstream in Z.

5.6.6 Secondary Vertex Reconstruction

Approximately 12% of all triggered events contained more than one vertex. This second vertex was the result of another beam particle in an event, or a secondary interaction in the target region, or a decay of a short lived particle. Secondary vertex code was implemented to find such vertices in events. The secondary vertex code only employed downstream tracks which were linked in both views. This code placed tighter constraints on the data by insisting that a downstream track be linked in both X and Y views and that those links point back to the same vicinity in space. This code was similar to the primary code in that both minimized the fitted χ^2_{NDF} values by removing tracks. In the secondary code, the primary vertex was defined as the most upstream vertex. A secondary vertex was then any vertex downstream of this primary which did not include any tracks from this primary vertex.

One further point, the vertex information used in this analysis came solely from the primary vertex algorithm. The discussion on secondary vertex reconstruction presented here is only for the sake of completeness.

Chapter 6 Monte Carlo Event Simulation

The relatively small cross section of direct-photon production makes its measurement particularly sensitive to backgrounds from decays of hadrons that yield photons in the final state. The largest of these backgrounds arise from geometrical losses due to the finite size of the EMLAC, failure to reconstruct low-energy photons from highly asymmetric π^0 or η decays, and coalescence of nearby photons from symmetric decays of high energy π^0's. Each of these sources provides single-photon backgrounds at a level which must be estimated by Monte Carlo (MC) simulation. In terms of the measurement of the inclusive meson cross sections, the Monte Carlo was essential in order to determine the reconstruction efficiency as well as the geometrical acceptance correction.

The Monte Carlo program used for this experiment is based on GEANT [35], a software program developed at CERN to simulate the passage of elementary particles through matter. GEANT provides a data base of standard geometrical shapes and material properties that can be used to model a wide variety of detectors. All essential physics processes that occur in the development of electromagnetic showers are also incorporated. The GEANT package can be tailored to specific experiments through a set of calls to user routines. These routines allow for complete specification of the experimental apparatus and the materials used in its construction. These routines also control the development of each "physics" event and ultimately the digitization and readout of each detector.

6.1 Philosophy

The philosophy behind the development of the E706 Monte Carlo was to produce a set of results which would represent the response of a "perfect" or "ideal" spectrometer. In the MC spectrometer, every channel was instrumented and fully efficient; the only source of background came from the interaction itself. Thus, for the tracking system, the Monte Carlo reported a set of space points for each of the charged particles at the location of each of the tracking devices. For the LAC, the MC stored the amount of energy each strip collected from the ionization in the liquid argon in the event. This ideal data was then processed through a separate software package which transformed these results into a more realistic representation of how the actual spectrometer behaved while taking data. In this separate routine, the detector efficiencies, pedestals, dead channels, gains, noise and resolution smearing were incorporated so that the final MC results more closely represented the actual data. With this procedure, one was able to separate the development of the actual Monte Carlo from the modeling of the performance of the spectrometer. Also, detector effects could be tuned without having to rerun the extremely time consuming and CPU intensive Monte Carlo event generation. The code for handling all of these detector effects was commonly referred to as the "Preprocessor" — a pre-processor to the standard MAGIC analysis package, but a post-processor of the Monte Carlo output.

The development of the Monte Carlo program proceeded in three distinct phases:

1.) Build a detailed Monte Carlo simulation which accurately represents the characteristics of the data.

2.) Develop a scheme to speed up the Monte Carlo without losing the agreement achieved in phase 1.

3.) Implement an event generator which simulates the event topology observed in the data.

6.2 Phase 1.

A detailed Monte Carlo program was developed and tested against a specific subset of data which was felt to be well understood. Very few assumptions were made early on as to what were the important elements which needed to be modeled. The Monte Carlo itself was used to "teach" us how sensitive the final results were to various parameters. In order to operate in this mode, GEANT was allowed to develop the electromagnetic showers in great detail. In the language of Monte Carlo experts, this is often referred to as "full electromagnetic showers". This simply means that GEANT tracked each and every particle inside a shower, calculating the probability of all known sources of energy loss and particle interaction step by step as each particle in the shower traversed the detector until the remaining energy fell below some preset threshold. On E706, the full shower cutoff threshold was set to 1 MeV.

The liquid argon calorimeter was modeled with great care inside GEANT. Where possible, measurements of each of the spectrometer's individual components and their locations were taken from the assembly logbooks, the assembly drawings, or from a run constants data base. All numbers used in the Monte Carlo were taken from measurements made at room temperature, not at liquid argon temperatures. No correction for thermal contraction was attempted.

The testing of the above Monte Carlo simulation was primarily done using Zero Mass Pairs or ZMPs. ZMPs are electron positron pairs resulting from photon conversions. This data sample was relatively plentiful, easy to identify, and both the momentum and energy of these particles could be separately determined. Successful agreement in E_{front}/E_{total}, width of E/P, and χ^2 distributions indicated that the response of the spectrometer was reasonably modeled in the Monte Carlo and that the various detector fluctuations and inefficiencies were also properly simulated in the Preprocessor.

If there were unlimited amounts of CPU, then phase 2 could be skipped all together. The problem with simply a phase 1 Monte Carlo is that it is very, very slow. It takes a tremendous amount of time to completely develop each electromagnetic shower. For example, to generate a single 70 GeV photon required 3 minutes of CPU time on an SGI 4100 computer. Remember that in the data, events contain on average $\approx$ 10 showers. It is hoped that the Monte Carlo effort will not be a statistical limitation for an experiment, an alternative approach was developed which improved the throughput of the Monte Carlo while perturbing the agreement found in phase 1 as little as possible.

For this experiment, approximately 1.6 million Monte Carlo events were generated in order to determine the proper γ/π^0 background as well as to determine the various reconstruction efficiencies for both π^0's and η's.

6.3 Phase 2.

This increase in speed, which was necessary to complete the 1.6 million events in a reasonable amount of time (1.5 months), was achieved in three steps. First, the representation of the LAC detector in the Monte Carlo was restructured to minimize the number of separate volumes a particle would have to traverse as it propagated through the detector. A "volume" in GEANT terminology is simply a region in space in which the physical properties remain constant. Every time GEANT encountered a new volume, it had to determine what the physical properties of the material in this new volume were and then perform a series of calculations to see how the particle being tracked would "react" while propagating in that material. Since these calculations take time, minimizing the number of volumes required to represent the LAC saved time. For instance, the representation of the copper cladding of the readout boards was removed from the MC, and its effective material was incorporated into the LAC by using a thicker and denser G-10 board. Similarly, the 12 separate layers of LAC dewar insulation were represented by one homogenized material whose properties, such as the density, were equivalent to the average properties of the individual layers. By this technique, over 200 volumes were eliminated relative to the phase 1 structure.

Second, an artificial cut was placed on all particles upon reaching the protective curtain, just upstream of the LAC. Particles whose energy was insufficient to reach the active region of the calorimeter were not tracked beyond this point.

Finally, the cutoff or threshold value for which a particle would continue to be tracked through the spectrometer was tuned. As stated above, full showers had a 1 MeV energy threshold for both photons and electrons. Substantial time savings could be gained by increasing this cutoff value for all particles. In order to achieve the speed required to complete the Monte Carlo pass in a reasonable amount of time, tests showed that this cutoff value had to be raised to at least 10 MeV. This presented a problem. Once the MC reached the cutoff value, the remaining energy was deposited at that point. This resulted in scattered 10 MeV "chunks" of energy which was a poor way of simulating the response of the LAC.

The solution to the tradeoff between scattered isolated chunks of energy in the spectrometer which were not proper simulation of physical showers and the need for substantial increases in speed was two fold. Allow GEANT to treat in full, all particles until they have reached their 10 MeV cutoff limit. Then a second piece of code, EMCHUNK would distribute this energy using a much simplified model of energy loss. To accomplish this, a temporary hits bank were written inside GEANT which uniquely described each showering particle at the point at which the particle's energy fell below threshold. Although this code

in principle could run stand-alone from the Monte Carlo, it was included and run as part of the MC package to make use of the UNIX farm's speed and to eliminate the storage of this very large hits bank.

6.3.1 Shower Parametrization – The Workings of EMCHUNK

EMCHUNK is nothing more than a simplified version of the GEANT MC program. Both programs track particles through matter and calculate the relative position, energy, and energy loss of each particle in a shower as that shower propagates through the spectrometer. The significant difference between the two is that EMCHUNK has a much simpler model of how a particle responds as it travels through matter than GEANT does. The procedure by which EMCHUNK operates is outlined below.

As the first step in the process, EMCHUNK has to read the hits bank information provided by GEANT, parse the information, and store it in an array. EMCHUNK then treats the various electromagnetic showers one particle at a time. The hits bank which GEANT wrote out has no particular order. Adjacent particles in the list may have come from separate electromagnetic showers in opposite quadrants of the calorimeter. It makes no difference. One by one, each particle is read in from the hits bank where the first branch point in the program occurs. EMCHUNK must determine whether this showering particle was a photon or an electron(positron). If this particle was an electron(positron), then the process of energy distribution began at precisely this point. If the particle was a photon, then based on the position and energy of this photon, a conversion

distance had to be calculated which indicated how far the photon would travel before it converted into an e^+e^- pair. This photon was then converted into an e^+e^- pair at a new position based upon the conversion length calculated in the previous step and a randomized distribution. The process of energy loss for this e^+e^- pair then began at this new location. For simplicity, the conversion length was calculated as the distance a photon would travel exclusively in lead before converting.

This electron (or positron) was then propagated through the detector one volume at a time. By knowing the location of the electron/positron, EMCHUNK was able to determine the type of material the particle was in and determine its relative position within the calorimeter (e.g. determine the position in terms of LAC variables such as Quadrant, Section, View, Strip, and Layer). The program sequentially stepped through each of the various volumes in the LAC along the trajectory of the showering particle. In each volume, the particle was allowed to undergo multiple scattering whereby its position and momentum vectors were adjusted accordingly.

The energy lost by the particle in each volume was also determined. The only allowed mechanism for energy loss in this simple model was ionization (dE/dX). The amount of loss due to ionization was found by a simple parametrization of some experimental results [36]. The amount of energy lost as a result of ionization in this volume was then subtracted from the total energy available to the showering particle.

If the volume in question was liquid argon, then things were a bit more complicated and one additional step was performed. The LAC, being a sampling calorimeter, only collected energy which was lost in the argon. Consequently, in this procedure of stepping through layers in the calorimeter, any energy lost as a result of ionization in the liquid argon was not only subtracted from the showering particle, it was also added to the LAC energy banks (in the appropriate Quadrant, Section, View, and Strip) which kept track of this digitized energy. The energy added to these banks was the energy lost in the liquid argon due to ionization weighted by a function. This function was determined empirically and was necessary in order to distribute the energy in such a fashion that the final shower matched the correct longitudinal shower shape observed in the data and reproduced in the full Monte Carlo. In other words, the simple model of multiple scattering and ionization was not sufficient to reproduce the longitudinal shower shape exactly.

This process of stepping through the layers in the LAC, calculating the impact of multiple scattering of the showering particle at each layer, determining the energy loss via dE/dX, and weighting the energy lost in the liquid argon by the aforementioned function was done for every particle in the hit banks. For a typical event containing a 3.5 GeV/c p_T π^0, this bank contained anywhere from 8,000 to 12,000 entries. The total energy deposited by EMCHUNK represented 50% of the shower's total energy.

The EMCHUNK parametrization in conjunction with the simplification of the spectrometer representation accomplished the goal of speeding up the full shower MC in excess of the factor of ten needed.

6.4 Phase 3.

With an accurate and relatively quick Monte Carlo program completed, the remaining task was to find an event generator which would provide a list of input particles to the GEANT Monte Carlo which accurately represented the event characteristics observed in the data. Two event generators were examined, PYTHIA [37] and HERWIG [7]. PYTHIA, written at CERN is one of the front end programs to JETSET which can be used to study hadronic processes. The emphasis of this program is on high p_T physics, but it covers the lower p_T domain as well. In our studies of an incident 530 GeV/c π^- beam on a hydrogen target, PYTHIA did quite poorly at matching event multiplicities both in the charged particle tracking system and in the electromagnetic calorimeter. We were unsuccessful in tuning the available parameters to get even a close agreement.

HERWIG is an alternative Monte Carlo event generator for high energy hadronic processes, with particular emphasis on the detailed simulation of QCD parton showers. The program had a reputation for doing a better job of matching event multiplicities than did JETSET. HERWIG indeed gave very good agreement in both charged track multiplicities (see Fig. 6.1) and photon multiplicities to the data for negative 520 GeV/c pions incident on a proton

target. Therefore, HERWIG was the event generator chosen to provide the necessary input to GEANT in order to calculate the direct-photon background as well as to calculate the vertex and reconstruction efficiencies.

6.5 Monte Carlo Operation

Upon successful completion of phases 1, 2, and 3, the Monte Carlo system was ready to go into production to generate a large statistical sample of events. The MC code was run in several different event selection ("trigger") modes for a variety of p_T ranges. Since π^0s are the dominant background in this direct-photon experiment, the thrust of the MC was placed on the generation of events containing high p_T π^0's.

For this MC production pass, the event selection criteria used in order to determine which HERWIG events were propagated through GEANT and which ones were rejected was quite simple. A HERWIG event was processed in GEANT if one of the particles in the event contained a generated p_T above a given threshold and if this high p_T particle was one of the particles contributing to the direct-photon background. That list of particles included the $\pi^0, \eta, \omega, K^0, e^+, e^-, \gamma$, and neutron.

Not all particles were allowed to decay in HERWIG. A π^0, for instance, would decay immediately into two photons if it were allowed. Once this occurred, then the simple selection routine outlined above which searched for π^0's would never see any. Consequently, the π^0 was held stable until it reached GEANT.

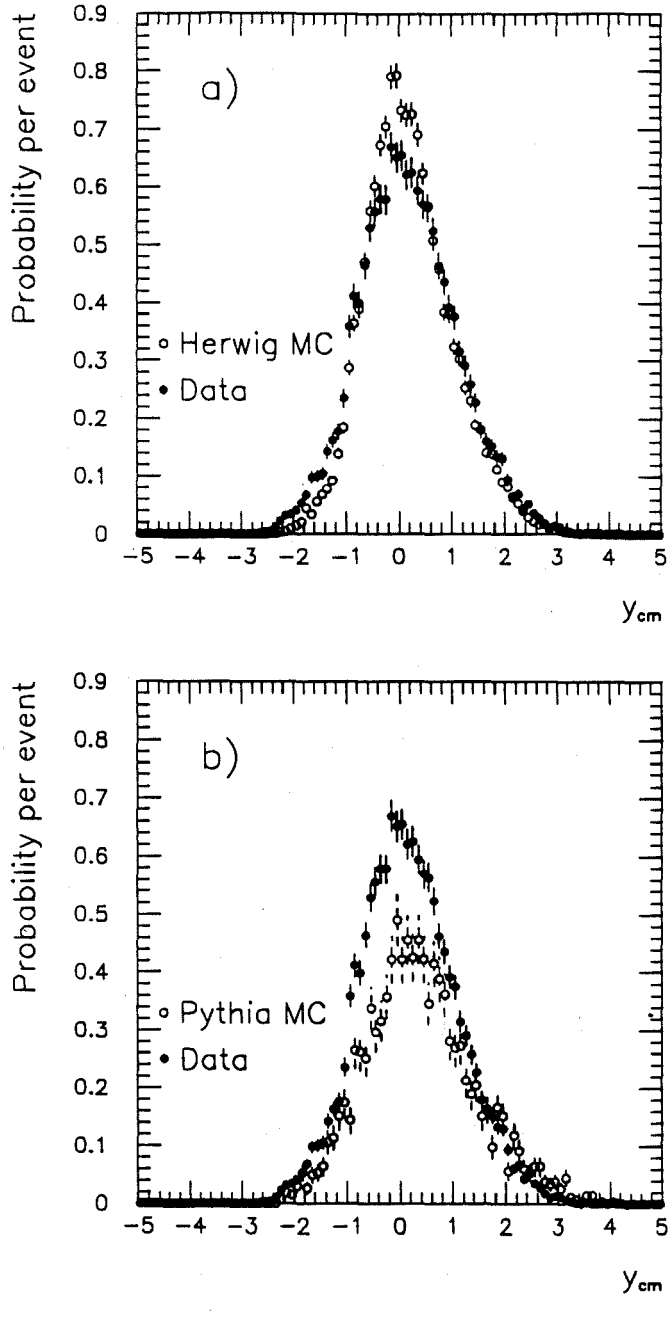

Figure 6.1 A comparison of the number of reconstructed tracks per event in data(open circles) for π^0 triggered events with a $p_T \geq 5.5$ GeV/c to the number of reconstructed Monte Carlo tracks (solid circles) where PYTHIA (a) or HERWIG (b) was used as the event generator. HERWIG does a better job of characterizing the underlying event than does PYTHIA.

As a general rule, short life time particles ($< 10^{-16}$ seconds) were allowed to decay in HERWIG. The longer life-time particles were held stable and forced to decay only in GEANT, that way the relative vertex positions of their decays were consistent with what was seen in data rather than artificially lumped at the primary vertex.

There were 7 different p_T thresholds used in this pass; they were 1.5, 3.0, 5.0, 6.5, 7.5, 8.0, and 9.5 GeV/c. There were also two different event selection criteria used. For the bulk of the statistics, the π^0 was held stable and used as a "trigger". This was referred to as the π^0 pass. The π^0 pass, as it was implemented, did not select η's, these particles were allowed to decay immediately and were only selected in this sample in the case of highly asymmetric decays in which one photon in the decay was sufficient to satisfy the selection criteria. In order to find the reconstruction efficiency for the η's, a second set of data was run with the η held stable. Here, the η was the principle particle in the selection criteria — only events containing a high p_T η were processed for this stream.

The advantage of the above selection criteria was that it was straight forward to implement. The problem with this selection technique was that the resulting events in the MC did not have the same characteristics as did the data. Recall that the data was primarily triggered by local depositions of energy. The processed MC events were selected solely on the p_T of a single particle. This discrepancy between triggering mechanisms had to be accounted

for when calculating the appropriate sample size to be generated. Approximately one half of all MC events generated through GEANT did not contribute to the reconstructed sample used in this analysis because either one of the photons from the π^0 or η landed outside of the fiducial regions of the LAC or else the two photons spanned two octants.

Besides being inefficient, this selection technique resulted in significant differences between the shapes of the reconstructed particle's energy asymmetry distribution in the uncorrected MC sample and in the data. This was most evident in the η sample where typical photon separations were on the order of tens of centimeters, wider than the definition of a local trigger. This resulted in an η signal in the data which was most often satisfied by highly asymmetric decays where one photon was sufficient to satisfy the local criteria for a trigger. Whereas, in the MC, the events were selected based on generated p_T and thus there was no bias based on relative energy of the two photons. The correction for this effect will be discussed at length in the analysis chapter.

Once all of the events have been generated, they were reconstructed in such a way that the end result could be fed seamlessly into the various E706 analysis packages. This MC reconstruction phase involved three separate steps.

- For each event, a run number had to be assigned to the MC data. These run numbers were weighted in such a way so that the relative number of events for any given run number was proportional to the number of events which were used in the final data analysis.

- The MC results were then adjusted using the Preprocessor. Based on the run number, this program transformed the "perfect" data so that it approximated how the spectrometer performed during that run.
- The "massaged" events were then fed into the same analysis path as was the data – a summary of those results were placed on a data summary tape (DST) in the same format as the experimental data. However, there was one difference between how the MC and data samples were treated at this juncture. FREDPED, which was applied to the data to accommodate event to event pedestal variations, was not used on the MC data. FREDPED was designed to remove shifts in the pedestal values thought to be the result of localized high intensity beam. Since this effect was not modeled in the MC, the systematic impact FREDPED had on the data was not represented in this sample.

Table 6.1 details the number of events that were generated at each of the p_T thresholds for each of the two MC event selection criteria.

6.6 Monte Carlo Energy Scale

An initial approximation of the MC energy scale was found using events containing a single 100 GeV photon which hit the center of Octant 1 of the LAC at a radius of 60 cm. These isolated showers were reconstructed and the resulting

Generated p_T in GeV/c	Number of π^0 Events Generated	Number of η Events Generated
1.5	100,000	0
3.0	750,000	125,000
5.0	210,000	32,000
6.5	110,000	22,000
7.5	0	12,000
8.0	40,000	0
9.5	10,000	0

Table 6.1 The Number of Monte Carlo events generated in various p_T bins.

energy was compared to the generated value. A scale factor was adjusted inside the preprocessor until this ratio was approximately unity.

The energy scale for the MC events, as in the data events was dependent upon the energy of the particle. In order to correct this, the ratio of reconstructed to generated energy, E_{rec}/E_{gen}, was plotted as a function of E_{rec}. The reconstructed energy here was corrected to account for any energy loss prior to reaching the active region in the calorimeter. The η sample was chosen to make this measurement because the resulting two photons from the decay were separated widely enough that each one could essentially be treated as an isolated shower. This also avoided the complication of evaluating how well EMREC was able to properly assign the individual energies of overlapping showers. This

curve was then fit as shown in Fig. 6.2 and the parametrization was found to be:

$$E_{rec}/E_{gen} = .991 - \frac{1.0}{-5.313 + 5.205 * E_{rec} + .1125 * E_{rec}^2} \qquad 6.1$$

where E_{rec} is the reconstructed energy and E_{gen} is the generated energy fed into GEANT. The final MC energy scale corrections were applied during the creation of the data summary files.

This MC energy scale was then checked by looking at the mass of the reconstructed di-photon pairs in both the π^0 and η sample as a function of energy for each of the various p_T runs. The mass of both particles was found to be stable to within $\approx 0.5\%$.

6.7 Monte Carlo verses Data Comparisons

To verify that the Monte Carlo simulations agree with the data, a set of criteria was used to compare the results of the Monte Carlo simulations with data. These comparisons are discussed below.

Partially reconstructed or misidentified π^0's account for approximately 80% of the total direct-photon background. An indication of the loss of π^0's can be obtained from the two-photon energy asymmetry distribution shown in Fig. 6.3. Energy asymmetry is defined as

$$A = \frac{|E_1 - E_2|}{(E_1 + E_2)} \qquad 6.2$$

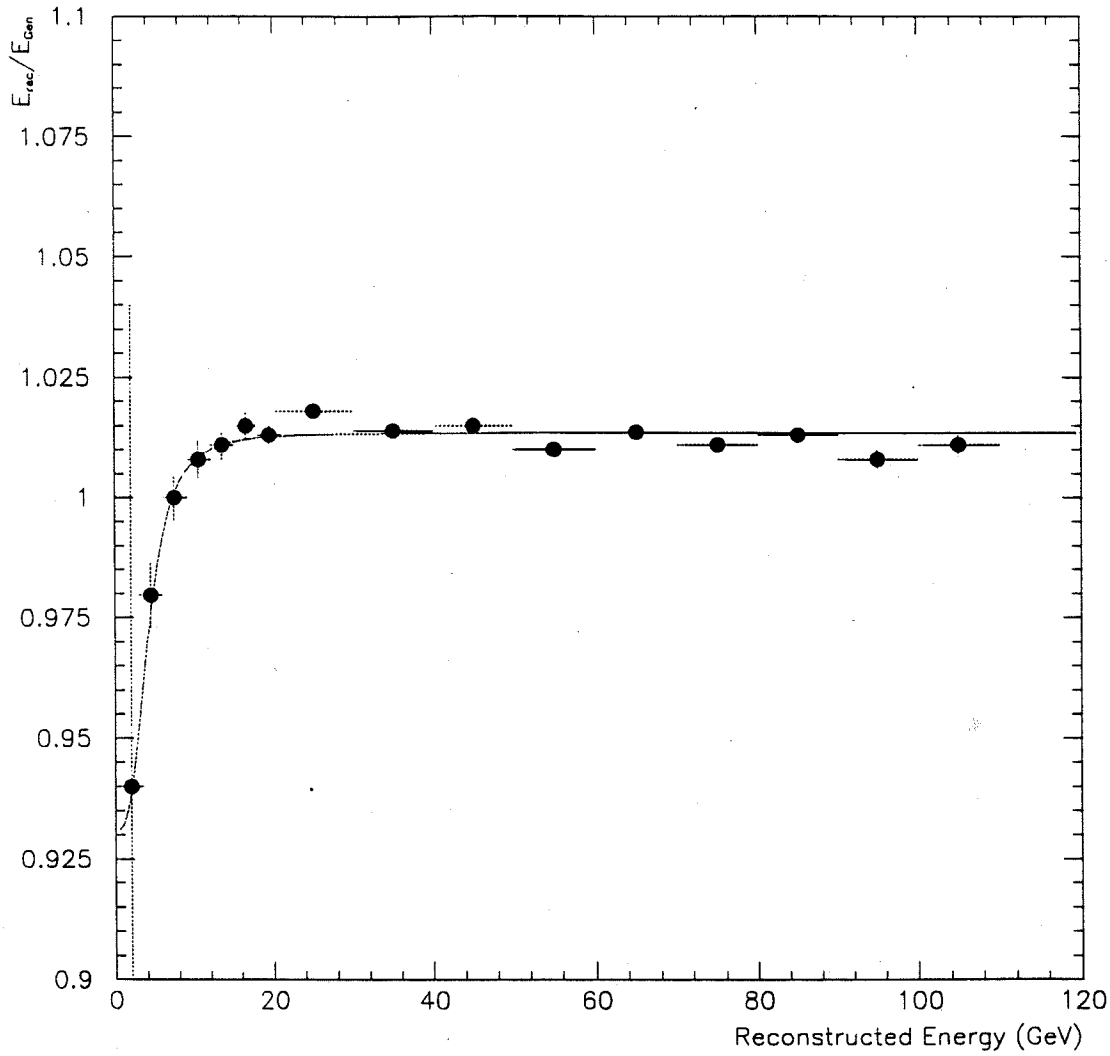

Figure 6.2 E_{rec}/E_{gen} vs E_{rec} for eta's with $p_T > 4.0 GeV/c$

and E_1 and E_2 are the energies of the photons from the π^0 decay. The fall off at large asymmetry values is attributed to losses of low energy photons. The agreement between Monte Carlo simulation and data indicates that the π^0 loss is properly simulated and that this dominant source of background to the direct-photon signal can be adequately accounted for based upon the Monte Carlo.

Another important comparison involves the ratio of reconstructed energy in the front of the LAC relative to the total (E_{front}/E_{total}). This ratio can influence the reconstruction of photons and thereby the identification of π^0's or η's. Figure 6.4 shows the E_{front}/E_{total} ratio for π^0's for different photon energies. The agreement between the MC and the data is excellent over the entire range. This ratio is very sensitive to the amount of material in front of the calorimeter and such good agreement indicates that the spectrometer was modeled correctly in the MC.

Another measure is provided by the comparison of the two photon invariant mass distributions. Figure 6.5 shows that the agreement between the MC and data is excellent in this projection, indicating that combinatorial background is well approximated and that the resolution of the EMLAC is well modeled.

χ^2_{NDF} comparisons for fitting photons to assumed shower shapes offer yet another indication of the performance of the MC simulation. Large differences between the two would indicate that the shower shape approximation in the fast MC was not a very good approximation of the data. While the agreement shown

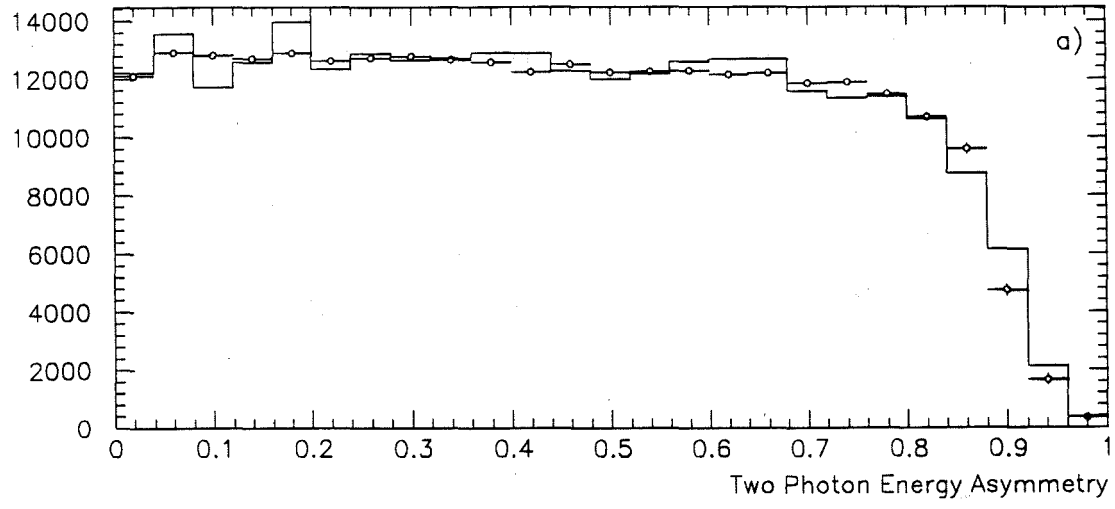

Figure 6.3 Background subtracted two-photon energy asymmetry distribution for photon pairs in the π^0 mass range for $p_T > 4.0$ GeV/c. The open circles are the data and the Monte Carlo distribution is shown as the histogram. The Monte Carlo curve was normalized to the data.

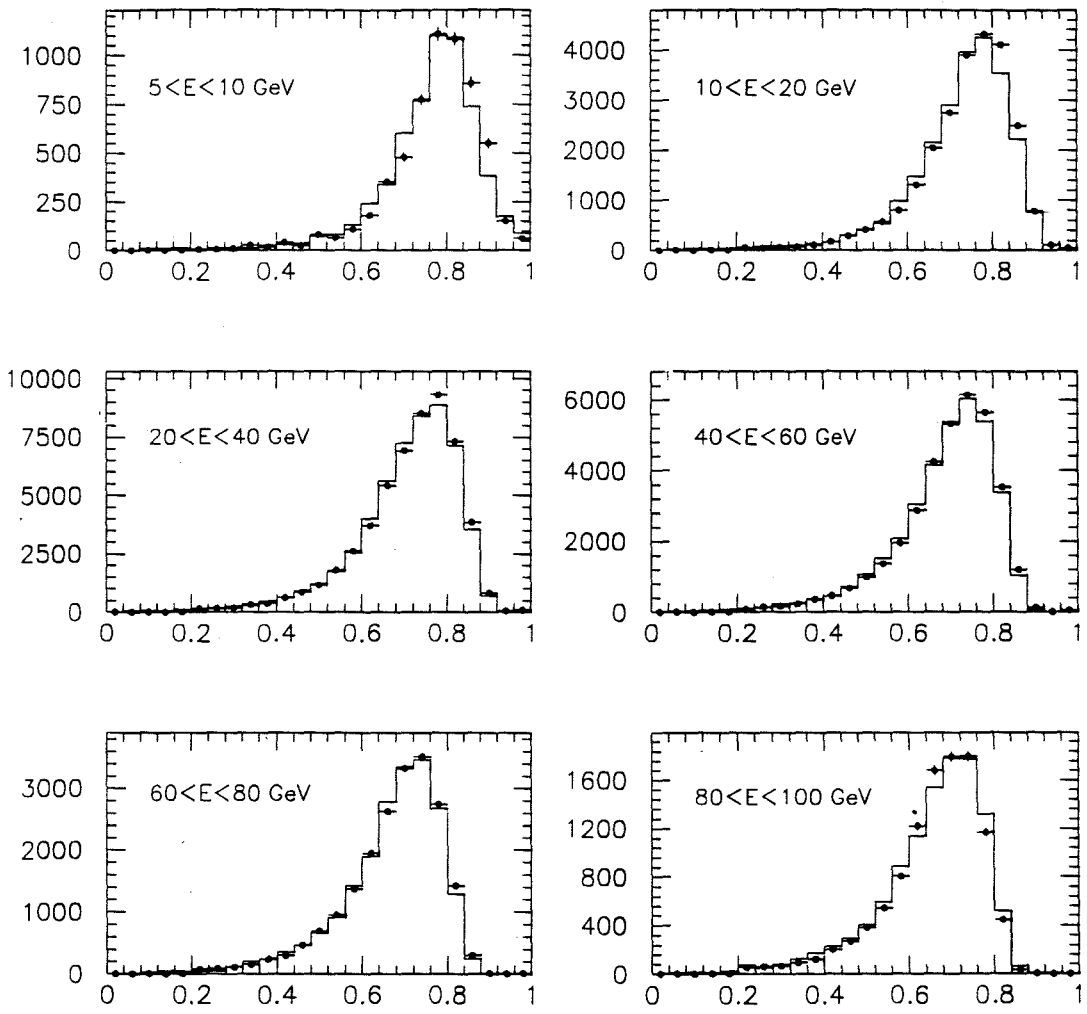

Figure 6.4 Ratio of the energy deposited in the front section of the EMLAC to the total energy deposited for MC simulations (histogram) and data (black dots) for various values of photon energies. The MC histograms have been normalized to the number of data events. The excellent agreement builds confidence that the spectrometer was properly modeled in the MC.

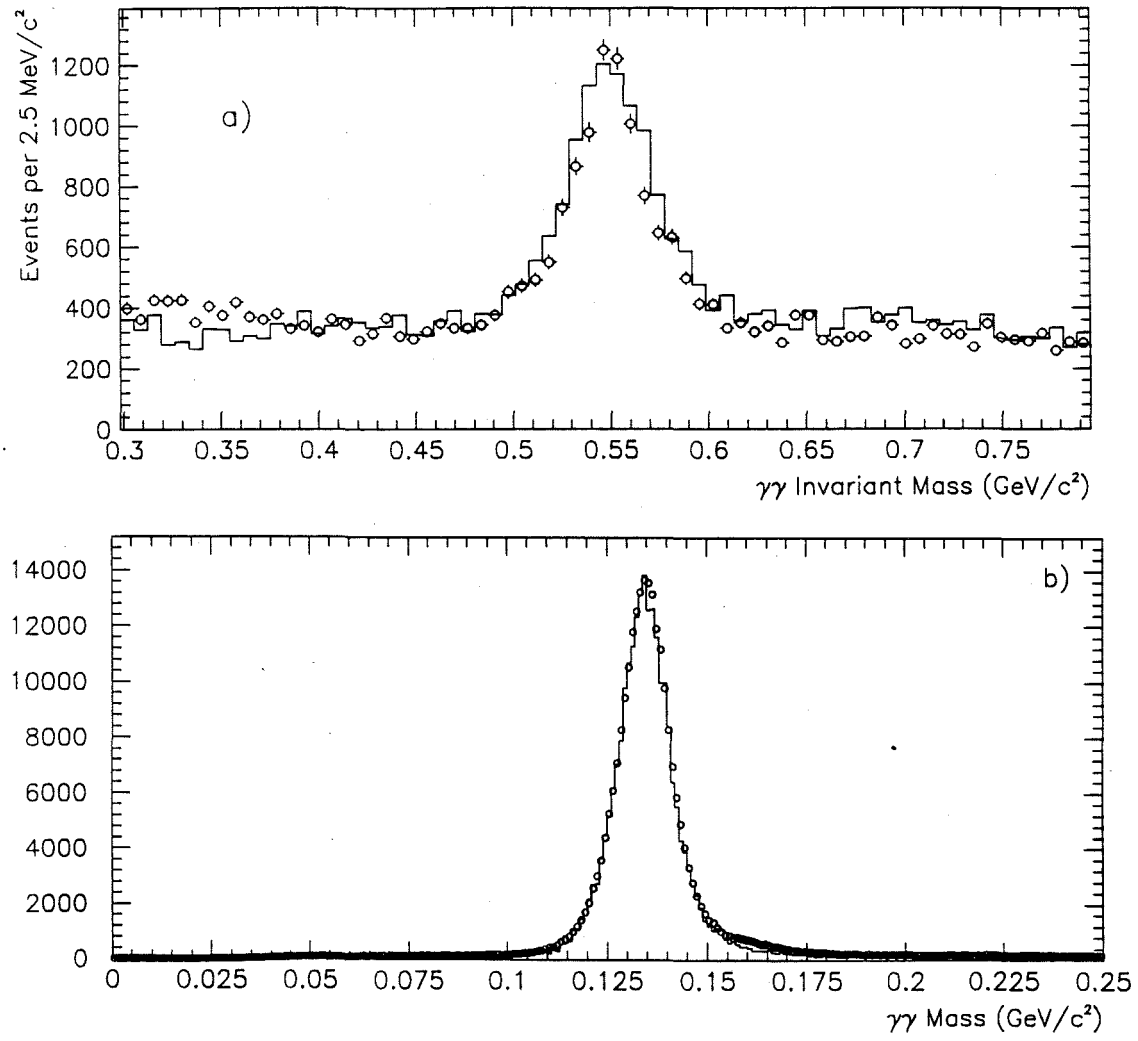

Figure 6.5 The two-photon invariant mass distributions for Monte Carlo simulations (histograms) and data (open circles) in both the η (a) and π^0 (b) mass range for $p_T > 4.0$ GeV/c and energy asymmetry $A < 0.75$. The MC simulation was normalized to the data at the peak.

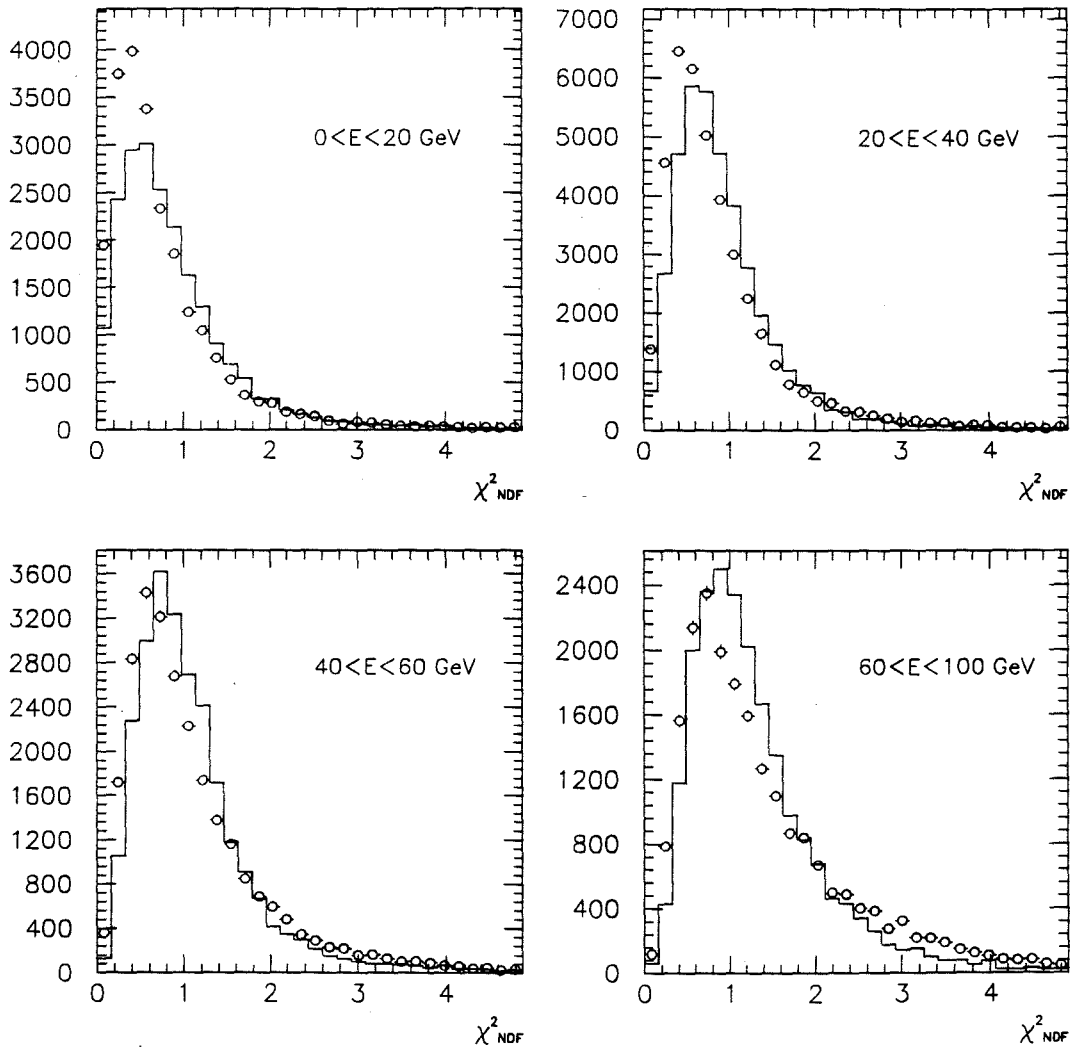

Figure 6.6 χ^2_{NDF} distributions for Monte Carlo showers (histograms) and data showers (open circles) over a wide range of photon energies. The MC histograms were normalized to the data.

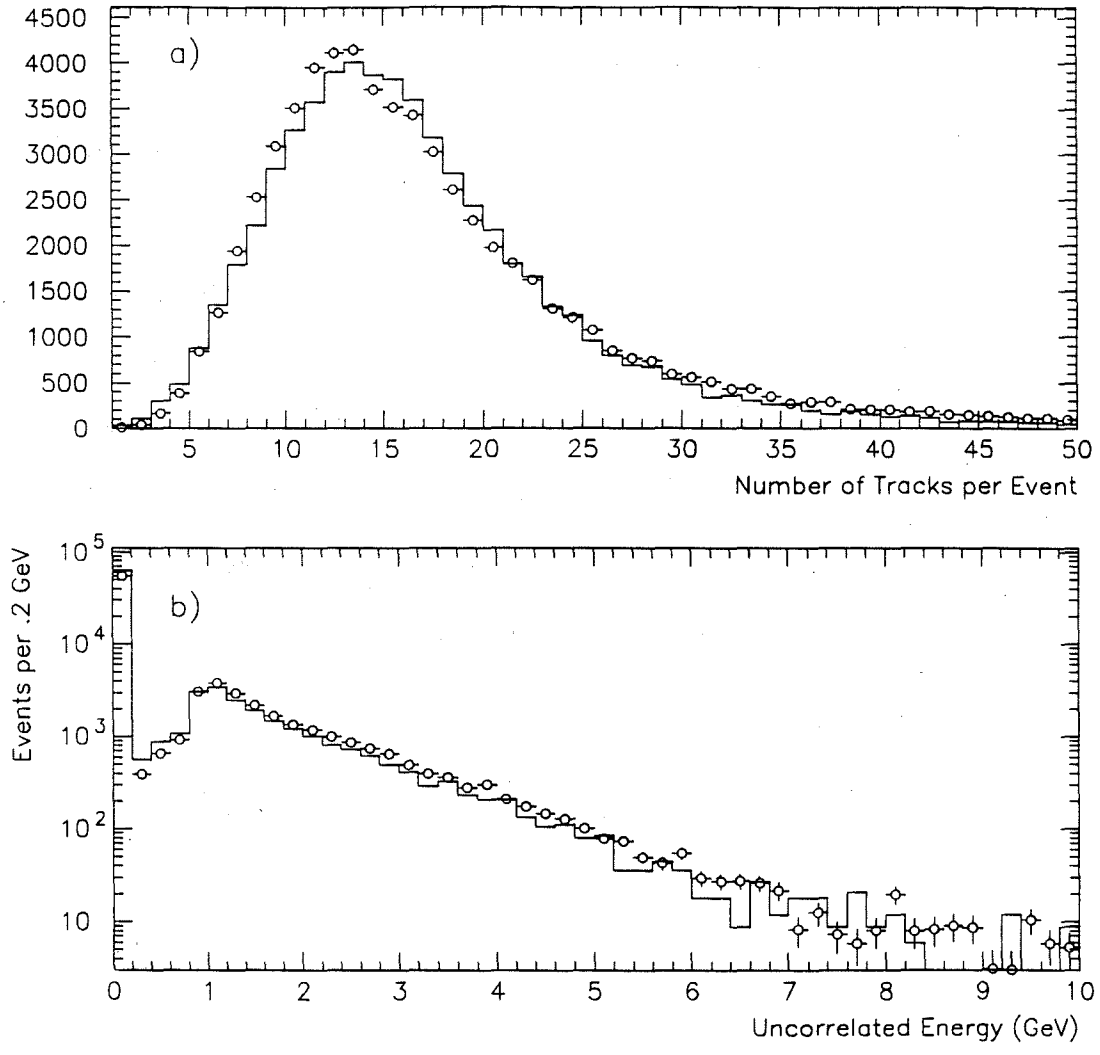

Figure 6.7 The number of charged tracks (fig. 6.7a) in an event is plotted for both Monte Carlo simulation (histogram) and data (open circles) to gauge the complexity of the event in the charged particle spectrometer. A comparison of MC (histogram) and data (open circles) distributions of uncorrelated energy is shown in Fig. 6.7b. Uncorrelated energy is the energy remaining in the form of single view "gammas" after the event has been fully reconstructed. The agreement in both (a) and (b) build confidence that the generator models the proper level of complexity in an event.

in Fig. 6.6 is not great, this level of agreement suggests that there are no major differences between the MC and data in this projection.

Another important set of checks is how well the event generator simulates the underlying characteristics of the event observed in the data. Figure 6.7(a) shows the average number of charged tracks for both MC and data. The agreement is very good indicating that the event generator is simulating the correct level of event complexity. To look at event complexity in the EMLAC, the amount of uncorrelated energy per event is plotted in Fig. 6.7(b). Uncorrelated energy is the amount of energy in an octant remaining in uncorrelated "gammas" after the reconstruction is complete. Much of the uncorrelated energy comes from either small showers or showers around boundaries. The agreement here indicates that amount of energy left uncorrelated is comparable in MC and data events.

Chapter 7 Analysis

7.1 Data Selection

The data used in this analysis were collected during the 1990 Fermilab fixed target run. For the 1990 run, almost all data were taken with a 520 GeV/c π^- beam incident on a combination of copper and beryllium targets. For ease in discussing analysis issues, these data have been subdivided into 6 distinct subsets. Each subset was collected under specific trigger conditions for which trigger thresholds, prescale factors, and hardware remained constant. Table 7.1 summarizes the number of reconstructed E706 events written to DST format for each trigger set.

Trigger Set	Run Number Range	Number of Events Processed on Farm
1	9181 - 9434	5,904,433
2	8989 - 9180	4,051,049
3	8629 - 8988	5,839,137
4	8240 - 8628	3,931,743
5	8055 - 8239	2,864,491
6	7594 - 8054	4,966,478
Total		27,557,331

Table 7.1 1990 Data Subdivided into Trigger Sets

Trigger sets 1, 2, and 3 were the only data used in this analysis, and correspond to $\approx$ 60% of the total 1990 sample. The trigger corrections for the other sets, which were recorded early in the run, are still being studied.

Not all of the reconstructed triggers in sets 1, 2, and 3 were used in this analysis. From Table 4.1, only 40% of all events taken satisfied the Single_Local trigger. Of the events in which the Single_Local trigger was satisfied, a significant number had a p_T value which was below the analysis cut-off threshold. This event sample also contained events triggered by beam associated muons which were also rejected in the analysis. Specific rapidity regions in various octants were excluded because there was either an inefficiency in the trigger, or else the trigger corrections for these areas were believed to be unreliable. π^0's and η's from these problematic rapidity regions were omitted and events from the corresponding regions in other octants were weighted appropriately to account for these excluded regions.

From the 16 million events available in trigger sets 1, 2, and 3, $\approx$ 11,300 η's were extracted with a $p_T > 4$ GeV/c for the purposes of this analysis. This chapter describes the various cuts made during the analysis, the motivation for these cuts, and the corrections made to account for various losses and biases.

7.2 Muon Bremsstrahlung

Muons represent one of the main sources of background to the measurement of direct photons and π^0's in E706. The principal source of these muons was

hadronic interactions in the beam dump downstream of the primary target. For a typical spill in the 1990 run, 3×10^{12} protons struck the primary target. This resulted in roughly 10^8 π^- incident on our target. The remaining particles produced in the primary target occasionally decayed into muons. Although this process was relatively rare, so too was the production of high p_T direct photons, π^0's and η's. These muons traveled roughly parallel to the beam, but were typically several feet away from it. What made these muons potentially troublesome was that they could interact inside the calorimeter and produce showers through the process of bremsstrahlung [38]. Because these muons were frequently incident at large radii, the resulting showers mimicked high p_T photons.

Care was taken during the design and data collection phases of E706 to minimize this problem. Muon spoilers were installed in the beamline to deflect muons away from the spectrometer. Three veto walls were also erected which shadowed the calorimeter. An event was not allowed to trigger the spectrometer if it occurred in coincidence with a signal from the veto wall logic. However, due to various inefficiencies, muons did sneak through thereby increasing the background to the two photon mass signal, as well as to direct photons. The following subsections discuss cuts devised to further reduce this muon background.

7.2.1 Veto Wall

Minnesota latches (see Chapter 5) were used to record the time history for each of the veto wall (VW) elements on an event by event basis. Offline, a detailed study was done of these time profiles. A software veto wall cut was imposed on the data using the latched time information. In this analysis, the logical variable VW_{123} is defined as

$$VW_{123} = (VW_1 .or. VW_2) \bullet VW_3 \qquad 7.1$$

where VW_1, VW_2, VW_3 are the individual veto walls. This off-line logic signal was evaluated independently for each of the four veto wall quadrants. The logical VW_{123} was set to TRUE for a particular veto wall quadrant if the above coincidence between elements in the same quadrant of VW_3 and the or of elements in VW_1 and VW_2 was satisfied within $\pm$ 1 RF bucket. For example, if VW_1 fired in quadrant 1 in time bucket 3, then VW_{123} would be considered TRUE if VW_3 in quadrant 1 also fired in either time bucket 2, 3, or 4. This offline VW requirement covered a larger time range than the online veto.

If VW_{123} was satisfied for a given veto wall quadrant, then no photon combinations in the corresponding LAC quadrant were included in the analysis. Figure 7.1 shows the spatial distribution for high p_T π^0 candidates before and after the software veto wall cut was applied. The population of high p_T showers at larger radii is dramatically reduced by the software veto wall cut.

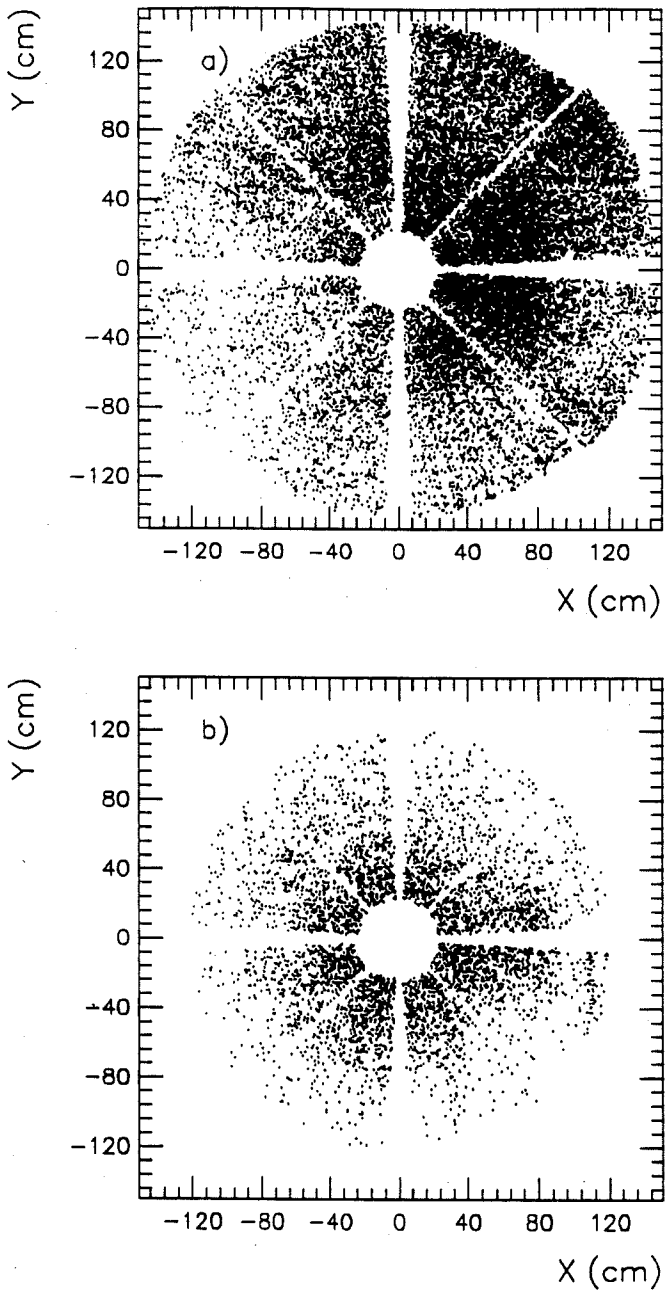

Figure 7.1 Position of π^0 candidates with $p_T > 4$ GeV/c for events in which the veto wall fired in the quadrant corresponding to the trigger quadrant of the EMLAC (a) and the same distribution when the there was no signal in the veto wall (b).

7.2.2 Directionality

The fact that muons from the primary beam dump travelled nearly parallel to the beam could be used to discriminate against them. Directionality was defined to assess the direction of an incident shower on the LAC as illustrated in Fig. 7.2. Directionality was defined as

$$\begin{aligned} Directionality &= R_{front} - Z^{LAC}_{front}/Z^{LAC}_{back} \times R_{back} \\ &= R_{front} - (900/918.5) \times R_{back} \end{aligned} \tag{7.2}$$

where R_{front} is the reconstructed radial position of the shower in the front section of the EMLAC and R_{back} is the radial position of the shower in the back section. Z^{LAC}_{front} and Z^{LAC}_{back} are the distances from the E706 target to the upstream faces of the front and back sections of the EMLAC, respectively; these values were 900 cm and 918.5 cm. For objects which originated in the target, the directionality would be approximately equal to zero. For objects which entered the LAC parallel to the beam, the directionality would be positive.

The directionality cut was not applied to all photons, but only to those photons which had $p_T > 5.5$ GeV/c, and intersected the LAC at $R > 40$ cm. Directionality was not used for $R < 40$ cm because it was not as well determined in this region. For p_T values less than 5.5 GeV/c, the veto wall cut alone was sufficient to render the impact of the muons negligible because of the larger cross section for genuine events, and so the directionality cut was not applied. High p_T objects which struck the outside of the LAC were considered potential muons

and hence cut if the measured directionality was greater than DIRCUT where DIRCUT is defined as

$$DIRCUT = .3456 + .00156 * R \qquad 7.3$$

The directionality spectrum for high p_T di-photon pairs is shown in Fig. 7.3.

7.2.3 Longitudinal Shower Profile

The interaction length for muons is much larger than the longitudinal thickness of the EMLAC. Hence, the probability of a high energy muon interaction is essentially independent of depth in the calorimeter. Since the EMLAC was segmented such that 1/3 of its material was in the front section and 2/3 in the back, these muons will more frequently deposit a substantial amount of energy in the back section of the calorimeter. Conversely, photons tend to deposit a large percentage of their energy in the front section of the EMLAC. Therefore, the ratio of front to total energy in the EMLAC (E_{front}/E_{total}) was used as an additional tool to discriminate photons from muons (as well as from hadrons). A shower was excluded from further consideration if (E_{front}/E_{total}) $<$ 0.2.

7.2.4 Balanced p_T ($BAPT/p_T$)

Another way to identify muons from the primary beam dump was to investigate the global characteristics of the event. Since the total amount of p_T in an event should balance, the p_T of the particle which triggered the event

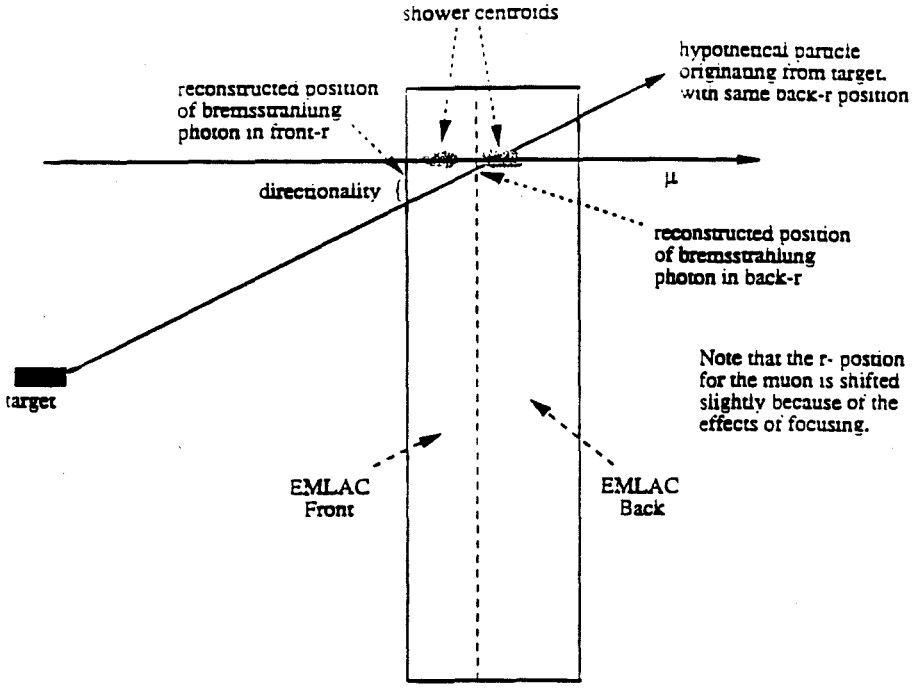

Figure 7.2 An illustration of the concept of photon "directionality". The relative R positions of showers in the front and back of the EMLAC are used to assess the direction of incident photons.

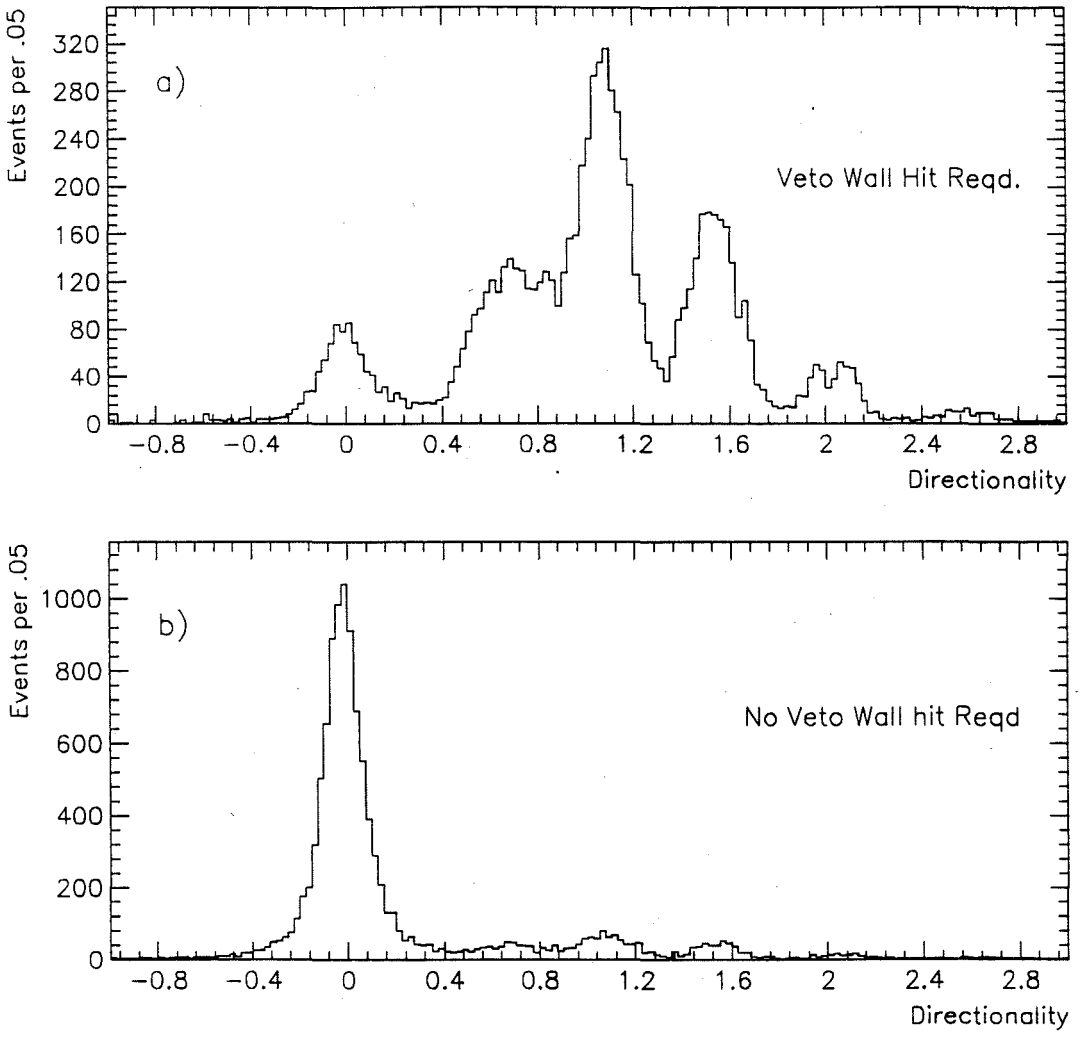

Figure 7.3 Directionality spectrum of the highest energy shower from (a) two photon pairs in the π^0 mass region when the veto wall fired in the triggering octant and p_T of the di-photon pair is greater than 5.5 GeV/c. The peak at 0 corresponds to photons from the target direction. The series of peaks at positive directionality come from muons travelling nearly parallel to the beam. The lower plot (b) has the same criteria as in (a) except that the VW in the triggering octant did not fire.

should be approximately equal to the combined p_T of all the particles in the associated away-side jet. Since muons were produced in random coincidence with typical events, the away-side of these types of events will generally contain relatively small amounts of p_T.

To quantify this argument, a variable BAPT was created. BAPT is the sum of the components of momentum of all the charged tracks and photons inside a 120 degree cone on the away-side from the triggered particle. As in the directionality cut, this balanced p_T cut was only needed and hence applied for those events with a $p_T \geq 5.5$ GeV/c. Based on the $BAPT/p_T$ spectrum for high p_T di-photons shown in figure 7.4, events were considered muon-like if the ratio of $BAPT/p_T \leq 0.3$.

7.2.5 Summary of Muon Cuts

A list of the cuts used to reduce the muon background are as follows:

- The logical $(VW_1.or.VW_2) \bullet VW_3$ in the quadrant corresponding to the trigger must not be satisfied.
- For those photons whose radius is larger than the EMLAC inner/outer boundary, the directionality of the largest photon in the $\gamma\gamma$ pair must be less than DIRCUT if the p_T of the $\gamma\gamma$ pair is greater than or equal to 5.5 GeV/c.
- The ratio of Balanced p_T to p_T (BAPT/p_T) must be $> .3$ if the p_T of the $\gamma\gamma$ pair is greater than 5.5 GeV/c.
- E_{front}/E_{total} must be $> .2$ for each photon in the $\gamma\gamma$ pair.

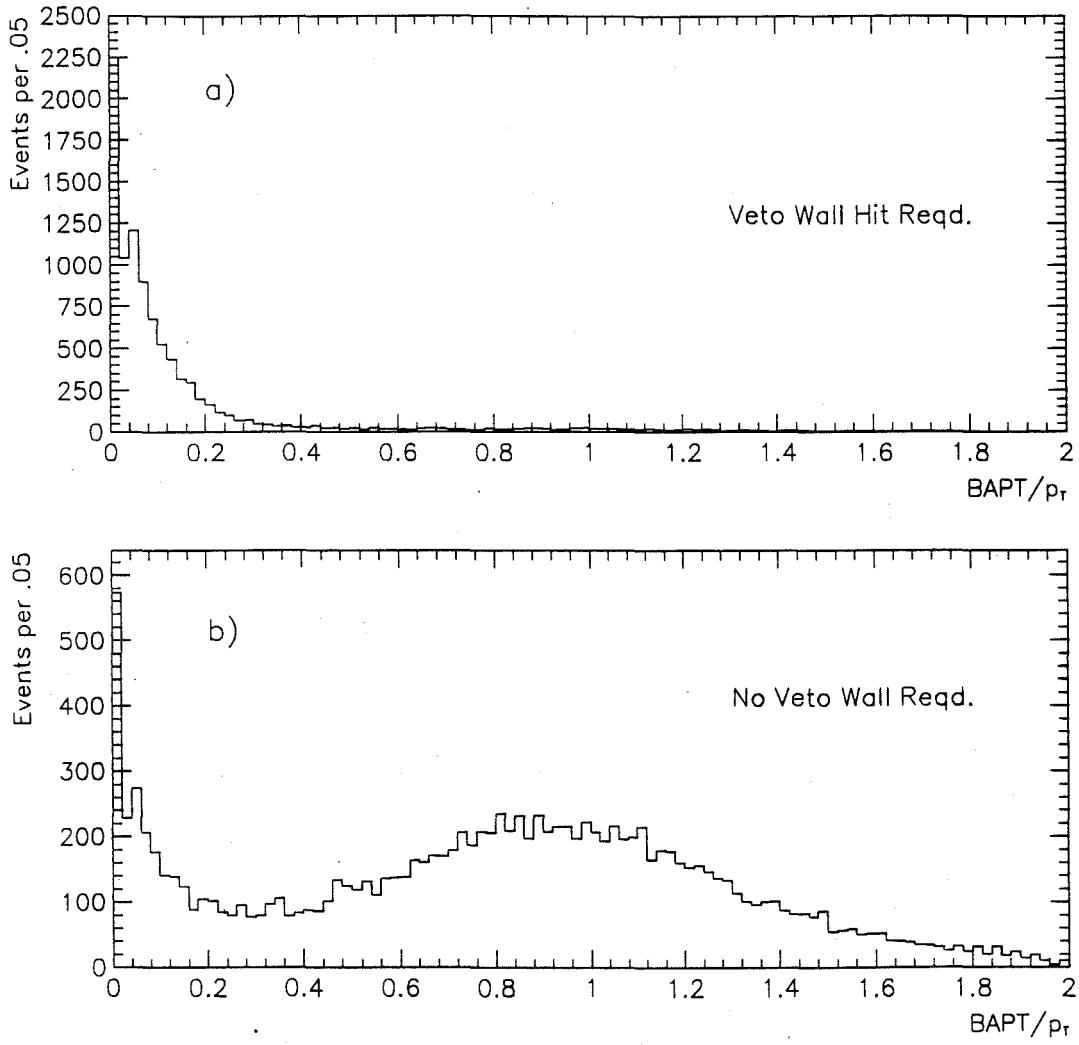

Figure 7.4 BAPT/p_T distribution where BAPT/p_T is the ratio of p_T on the opposite side of the triggering event divided by the p_T of the triggered particle. This ratio is used to quantify the overall characteristics of an event in order to discriminate against bremsstrahlung muons. The p_T deposition due to muons was generally uncorrelated with the interaction in the target which hence had small amounts of p_T on the away side, while high p_T events due to interactions in the target tend to have a more balanced ratio. Figure (a) shows photon pairs in the π^0 mass range with $p_T > 5.5$ GeV/c when the veto wall fired while in figure (b), the veto wall did not fire.

The muon cuts were less essential to this analysis than to the analysis of π^0 production. Muons frequently contribute to di-photon pairs whose mass is near the π^0 mass range, but less so near the η mass. However, as shown in Fig. 7.5, by applying these cuts to a high p_T sample of η's, the size of the signal remained essentially unchanged but the ratio of signal to background was increased by approximately a factor of three. (Requiring the same muon cuts in the η analysis as in the π^0 analysis is also of value in comparing π^0 and η production.)

7.3 Target Fiducial Cuts

For the 1990 data run, the experimental target was made up of two separate materials. The principal target consisted of two separate blocks of beryllium. The other target material was two thin wafers of copper located just upstream of the beryllium. This target was sandwiched between the beam and the downstream SSD planes. (See Table 2.3 for the exact dimensions and locations of the target.) An uncorrected vertex distribution for interactions that included a high p_T π^0 is shown in Fig. 7.6. Cuts were made in the appropriate valleys of this vertex distribution along Z in order to reliably identify the target material for each interaction. Target fiducial cuts were employed in X and Y, as illustrated in Fig. 7.7, to exclude interactions in the target holder. Each scatter plot shows the vertex position in X and Y for π^0's which interacted in the vicinity of the beryllium and copper targets. The square region, common in both plots, maps out the active region of the beam hodoscope that defined beam in the

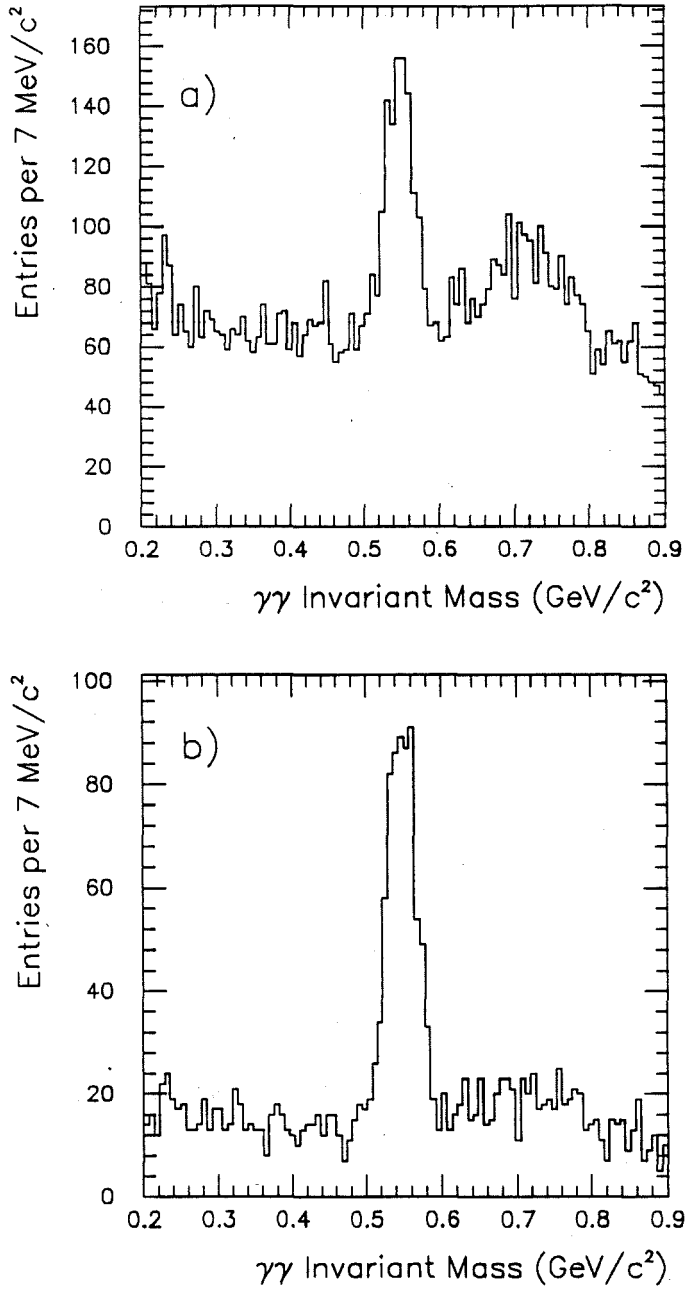

Figure 7.5 A two photon mass plot for those combinations with $6 < p_T < 8$ GeV/c without (a) and with (b) muon cuts. The number of events in the peak above background is approximately the same for both spectra but there is a dramatic improvement in the ratio of signal to background when the muon cuts are applied.

experiment. The circle in (7.7a) is an outline of the beryllium target location. The truncated circle in (7.7b) is the outline of the copper target. From these plots, it is clear that the beam was centered on the hodoscope while the targets were not.

To estimate the fraction of the beam intersecting the fiducial region of the target, the ratio of the number of vertices contained inside this target fiducial region to the number of vertices reconstructed in the SSD's within the hodoscope's shadow was calculated. This ratio was determined separately for the silicon SSD wafers just upstream and downstream of the target. The ratio of vertices for the upstream silicon and the downstream silicon agreed to within 2%. For trigger sets 1, 2, and 3, 70% of the beam illuminated the fiducial region of the target.

7.4 Vertex Reconstruction Efficiency

The vertex reconstruction efficiency was determined using the HERWIG π^0 Monte Carlo sample. The preprocessor was used to modify the ideal hit bank distributions written out by the MC in order to take into account noise hits, double and triple hits, plane efficiencies, etc. in order to simulate the same level of tracking confusion in the MC as observed in the data. The vertex efficiency was determined by taking the ratio of the number of reconstructed vertices to the number of generated vertices as a function of Z. This efficiency was found to be uniform in Z with a value of 0.996%.

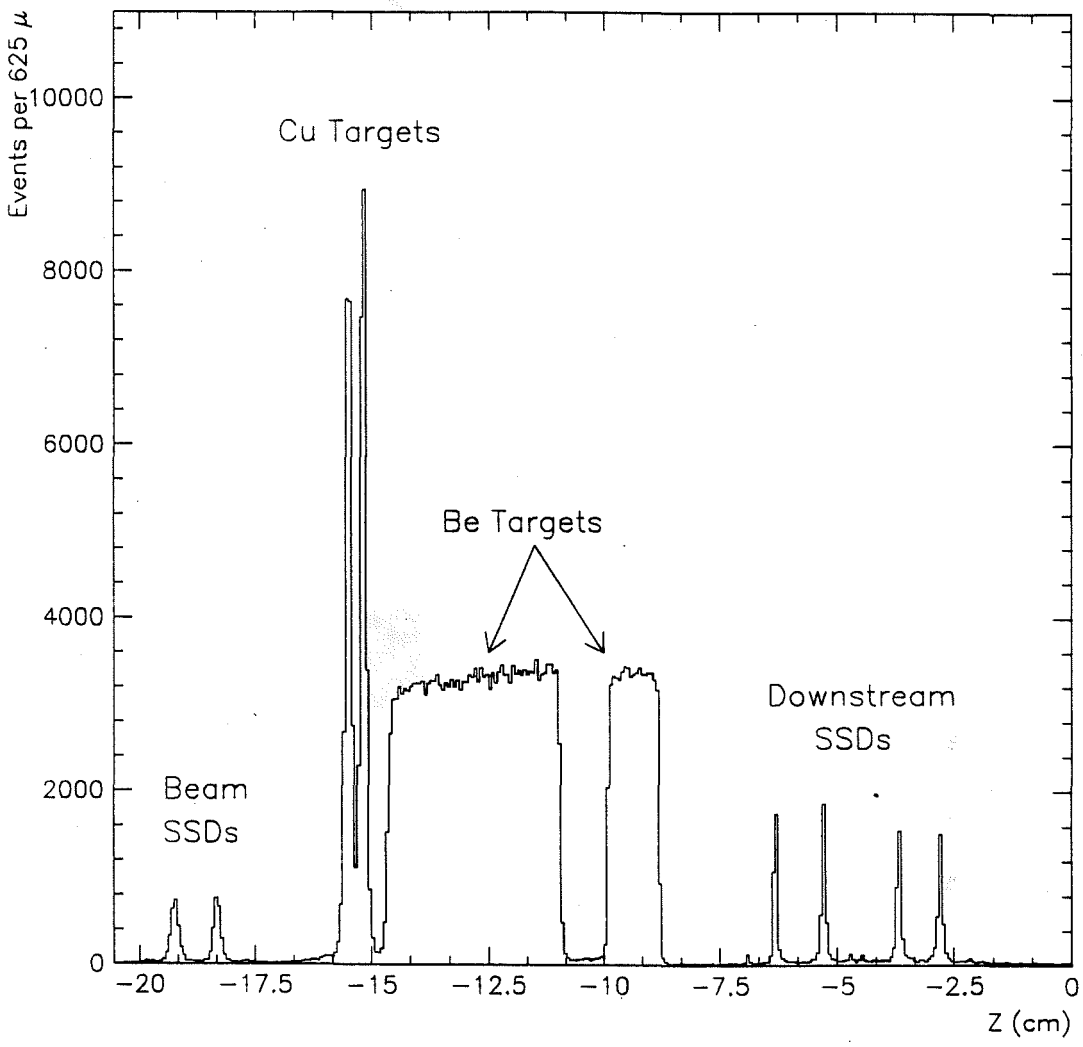

Figure 7.6 Vertex position in Z for those interactions which generated a high p_T π^0 in the target region.

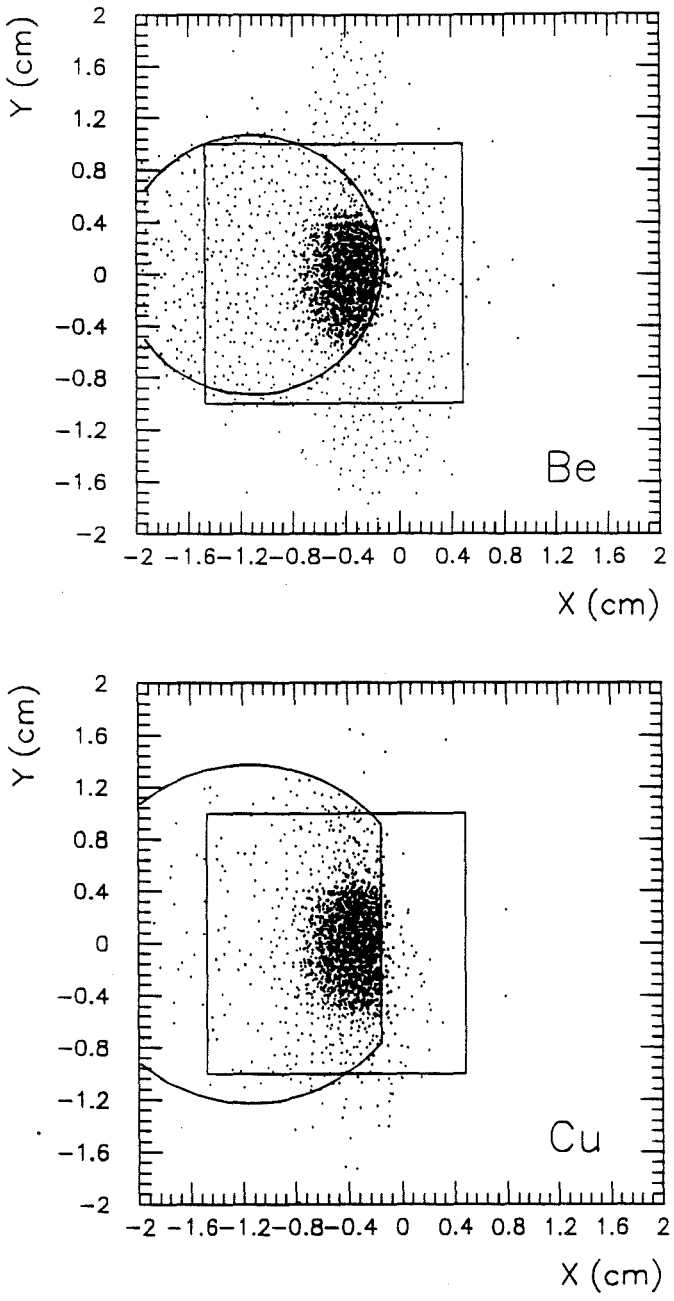

Figure 7.7 Vertex distribution in X and Y for events triggered by a high p_T π^0 which interacted in the Be (top) and Cu (bottom) target locations. The square region which is approximately centered around the central cluster of points maps out the sensitive area of the beam hodoscope. The circle in (a) is the physical location of the beryllium. In (b), the truncated circle is the physical shape and location of the copper target. The beam is centered on the hodoscope but not on either target.

7.5 Definition of the η Signal

Figure 7.8 shows the two photon mass distribution in the region around the η mass for photon pairs used in this analysis. An η candidate was defined as a $\gamma\gamma$ pair for which both photons hit the same octant, and whose two photon mass was determined to be in the range between 450 to 650 MeV/c^2. The amount of signal above background was calculated using two different methods. The two methods discussed below gave answers which were consistent to within 1%.

In method 1, the background adjacent to either side of the η mass peak was parametrized. Specifically, the data contained within 300 to 450 MeV/c^2 and 650 to 800 MeV/c^2 were fit by a function that was either linear or quadratic depending upon the p_T bin. The η signal was the difference between the number of all mass pairs inside the signal region and the area under the estimated background curve in that region.

Method 2 involved a technique known as "side-band subtraction." This technique assumed that the background inside the signal region could be approximated by a linear interpolation between the background regions on either side of the signal. The two side-band regions were between 350 to 450 MeV/c^2 and 650 to 750 MeV/c^2. Note that the combined width of both side bands is 200 MeV/c^2 wide, exactly the same as the width of the signal region. The calculated signal above background was just the total number of entries found in the signal region minus the total number of combinations in both side-band

regions. Except where explicitly stated, all plots shown for this analysis were done using this side-band subtraction technique.

7.6 Energy Scale

Precisely determining the energy scale for a sampling calorimeter is a difficult task. There are a large number of corrections which must be taken into account. A detailed discussion of the subtleties involved in setting the energy scale can be found elsewhere [32]. What is presented here is merely an outline of the procedure employed to set the energy scale for the 1990 data.

The first step in setting the energy scale, as mentioned in section 5.2, was to account for the time dependent behavior of the reconstructed π^0 mass. This was done by plotting the mass of the π^0 as a function of beam days and then parametrizing this curve as illustrated in Fig. 5.1. Currently, there is no satisfactory explanation as to the cause of this time dependence. The energy scale of the data was adjusted based upon the curve shown in Fig. 5.1.

To insure that the $\gamma\gamma$ mass pairs contributing to the energy scale determination came from well measured electromagnetic showers, the following four conditions were employed: $E_{front}/E_{total} > 0.2$, χ^2/DOF for each photon < 5.0, a two photon energy asymmetry < 0.5, and the elimination of any photon in which the veto wall fired in the quadrant of relevance. With these cuts applied, the steps in the energy scale determination were made in the following order.

- Determine the octant to octant scale correction. This was done

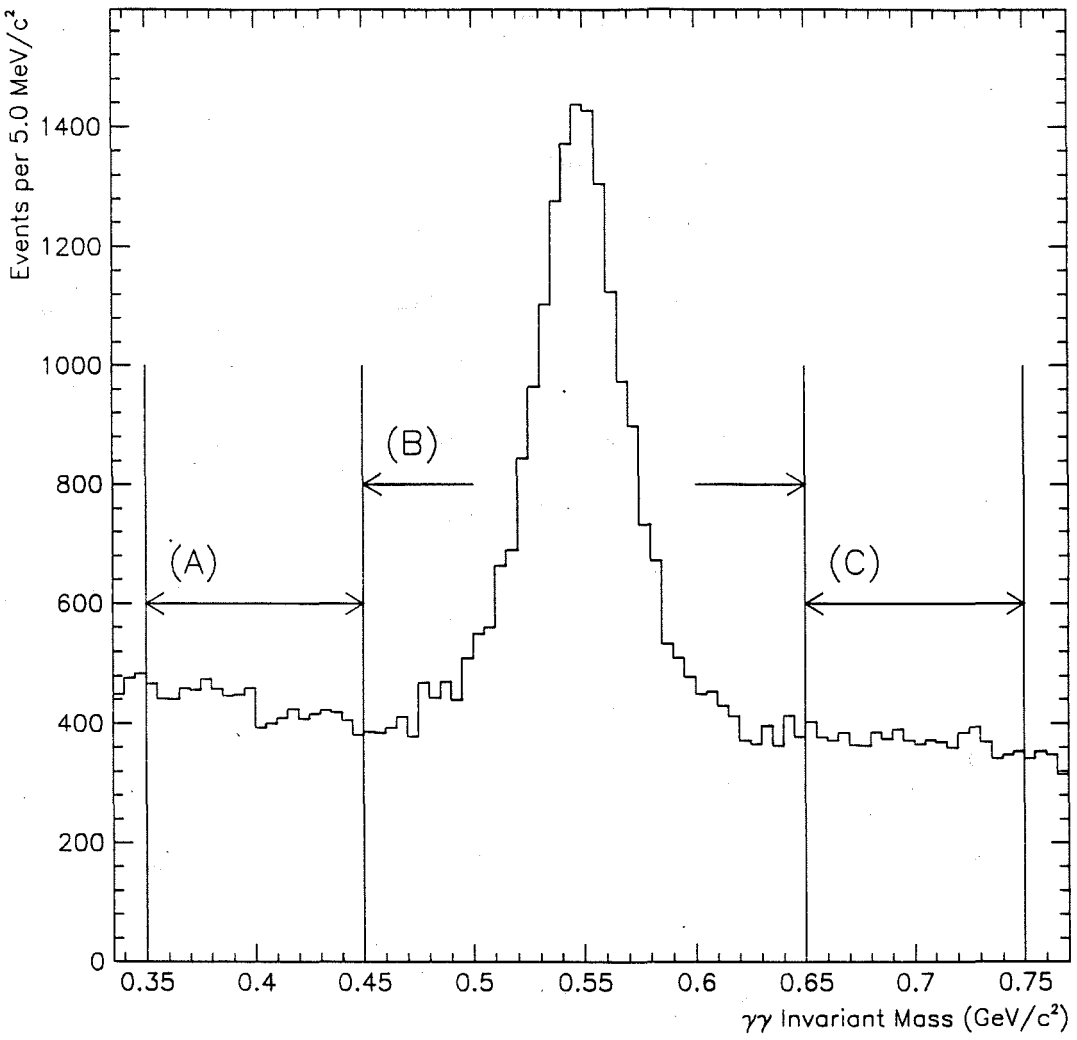

Figure 7.8 Uncorrected $\gamma\gamma$ mass plot in the region of the η mass for all runs used in this analysis which have two photon $p_T > 4.0$ GeV/c. Regions (A) and (C) are the side-band regions used to estimate the size of the background under the peak. Region (B) is the signal region.

using π^0's with $p_T > 4.0$ GeV/c. This correction was only approximate and was fine tuned at a later stage in the procedure.

- If a photon was within $\pm$ 5 cm of the EMLAC inner/outer boundary at 40.175 cm, then the energy of the photon was calculated based upon twice the energy reconstructed in the R view rather than the sum of the R view and ϕ view energies since the ϕ view energies of showers on this boundary are compromised.
- Apply the ELOSS correction to account for the mean loss of energy as the photon traveled from the center of the magnet until it reached the first active region in the EMLAC. The active region was defined as the location of the first radial readout board ($\approx$ 900 cm). This function was determined using MC data.
- Correct for the radial dependence of the energy scale for each octant. In order to determine this correction, two samples were investigated – the π^0's accumulated via the Two_Gamma triggers with $p_T > 2$ GeV/c, and η's selected by the Single_Local trigger with $p_T > 4$ GeV/c. Both samples provided widely separated showers and the radial dependence on the energy scale was consistent between them. The π^0 sample was chosen for determining this correction due to its larger statistics which allowed a scan in smaller radial bins.
- Fine tune the octant dependent energy scale using high p_T η's.

- Check the γe^+e^-sample to see if there were any residual correction; there were none.

The energy scale for electrons was determined via the same procedure except that a residual E/P correction was applied to the electrons as a function of energy. This correction was determined using the MC data and was necessary to account for the difference in shower shape between photons and electrons.

After all of the corrections were applied, the uncertainty in the energy scale was found to be 0.5% [32]. Figures 7.9 and 7.10 show the energy corrected π^0 and η mass plots. Figure 7.11 shows the π^0 and η mass dependence as a function of octant. The variation between octants is within 0.2%.

7.7 Energy Asymmetry Cut

The π^0 and η mesons are both pseudo-scaler particles. Therefore they decay with a flat distribution in $cos\theta^*$, where θ^* is the angle between one of the decay photons and either the π^0 or η direction, in the π^0 or η rest frame, respectively. In the lab frame, this distribution is approximately equal to the energy asymmetry A, where

$$A = \frac{|E_1 - E_2|}{(E_1 + E_2)} \tag{7.4}$$

with E_1 and E_2 representing the energies of the two photons. Specifically,

$$A = \beta cos\theta_{cm} \tag{7.5}$$

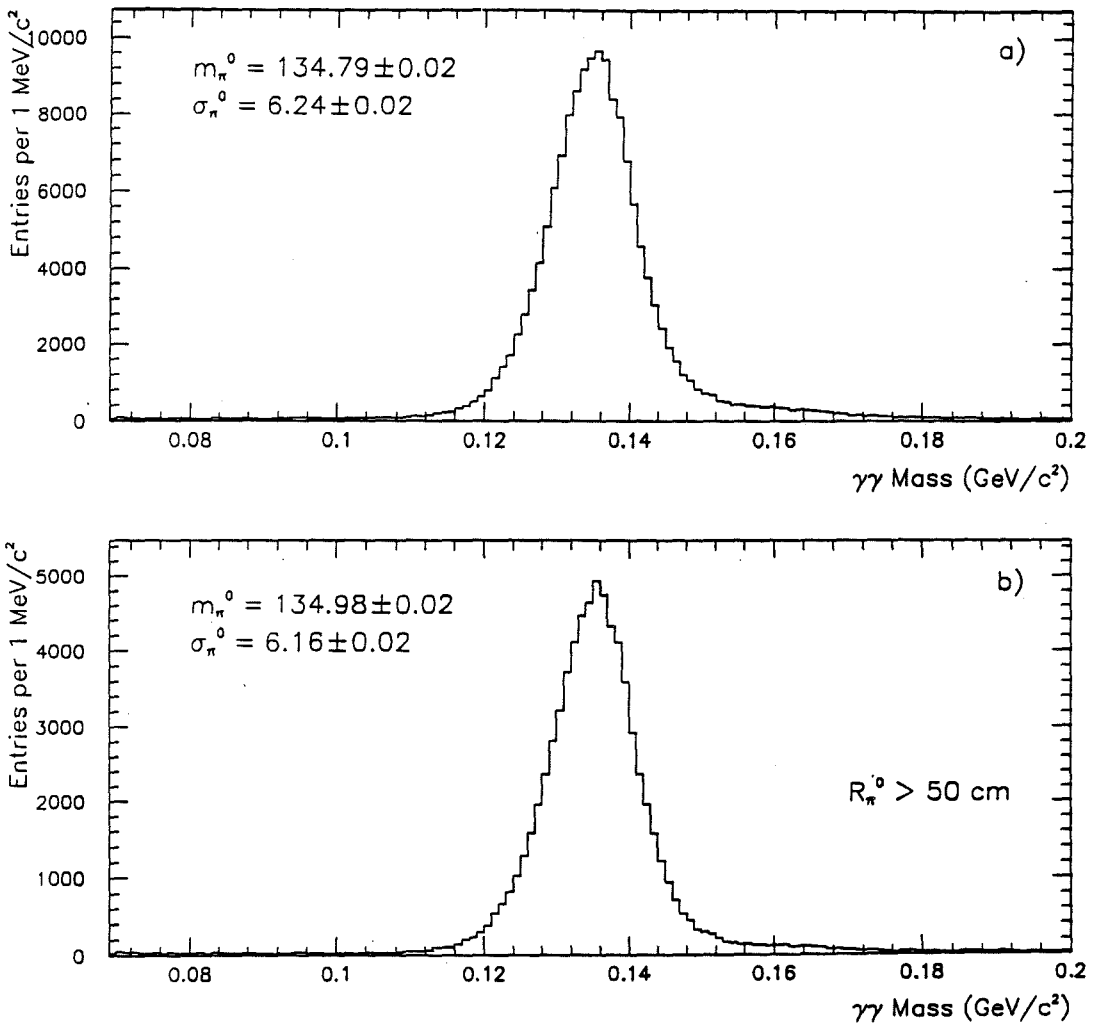

Figure 7.9 Two photon mass plot in the π^0 region for $p_T > 4.0$ GeV/c. The cuts used here were the ones discussed in section 7.5 after the energy scale corrections have been applied.

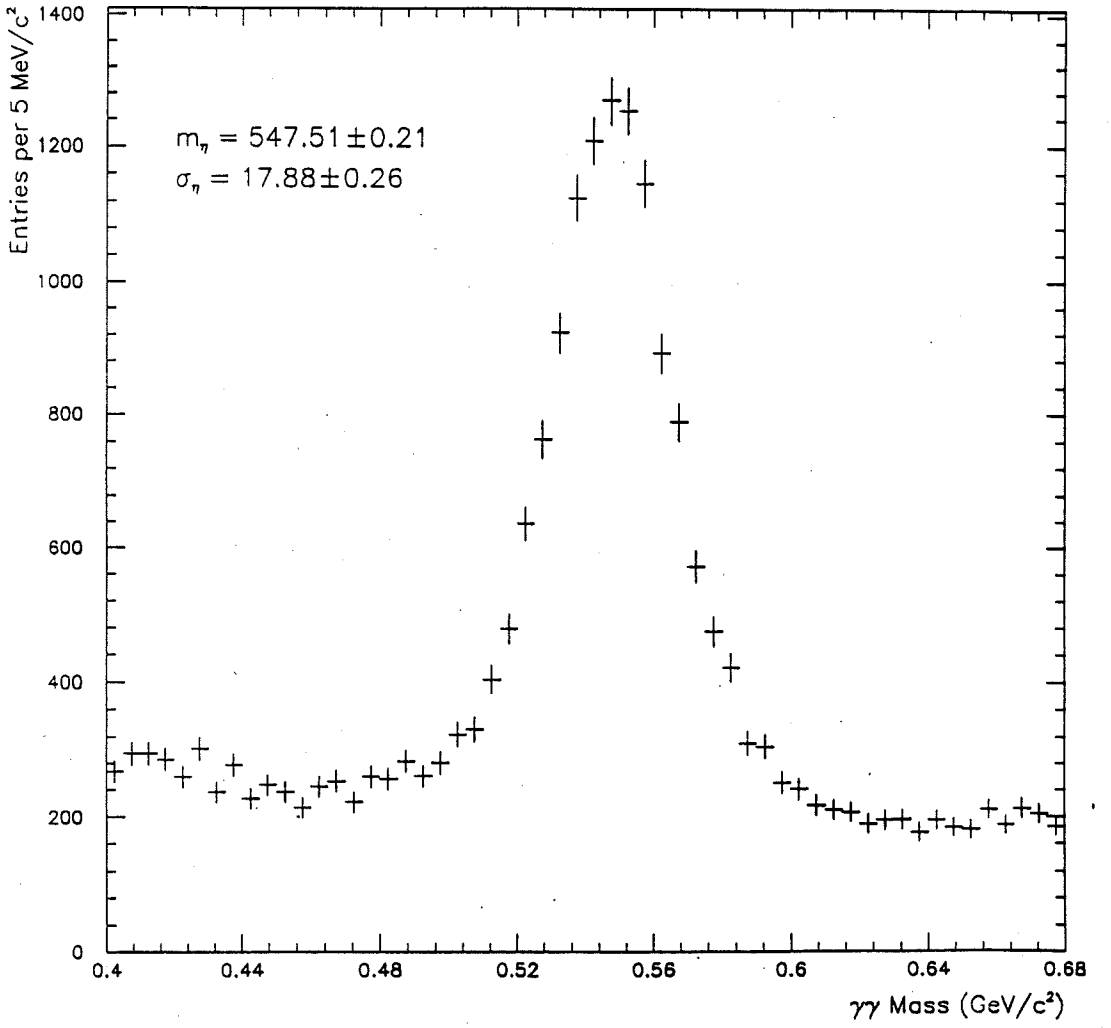

Figure 7.10 Two photon mass plot in the η region for $p_T > 4.0$ GeV/c. The cuts used here were the ones discussed in section 7.5 after the energy scale corrections have been applied.

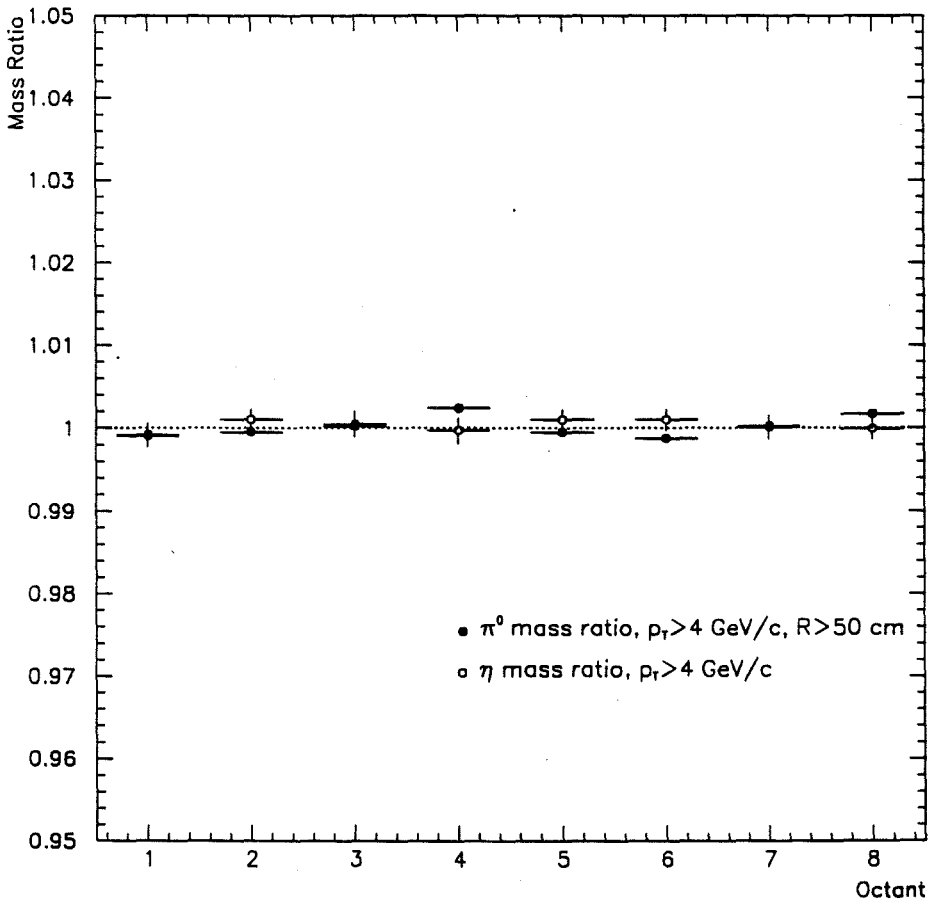

Figure 7.11 Corrected mean η mass for each octant.

For high energy showers $\beta = P/E \approx 1$. Since for spin 0 particles, the $cos\theta_{cm}$ distribution is flat, so the energy asymmetry distribution should also be flat.

However, the energy asymmetry distribution of background combinations of two photons tends to be peaked at larger asymmetries. Consequently, an upper limit on A can preferentially eliminate background.

Figure 7.12 shows the two photon mass spectra in the η mass vicinity for several different ranges of energy asymmetry. Above an energy asymmetry value of 0.75, the ratio of signal to background is degrading and above A of 0.85, there is no discernable signal.

Figure 7.13 shows an energy asymmetry plot of background subtracted η's. The agreement between MC and data is excellent. Nevertheless, an energy asymmetry cut of 0.75 is applied in this analysis to make use of the larger signal to background in that domain. Since the energy asymmetry of the generated η's is flat over the full range, the correction for this cut is straightforward.

7.8 Fiducial Cuts

A fiducial cut was employed to exclude showers near the inner and outer edges of the LAC. Showers near the quadrant boundaries were also eliminated by this cut. A significant fraction of the energy of such showers goes undetected resulting in substantial uncertainties for photons near these edges. Photons near a boundary between octants in the same quadrant were also excluded due to larger uncertainties in the reconstructed energies of such photons as well as

in the associated trigger corrections; when photons from the decay of an η or π^0 were near the octant boundary, they had a reduced probability of triggering since the p_T of the photon on the boundary is shared between octants.

7.9 Geometrical Acceptance

Geometric acceptance corrections for π^0's and η's were calculated using a simple Monte Carlo program which simulated two photon decays of both particles and took into account the physical geometry of the spectrometer. (This purely geometric program was independent of the MC used for the rest of this analysis.) For this measurement, the actual showers in the LAC were unimportant. What was of significance was whether a given photon pair intersected the LAC in an area that was sufficiently instrumented so that EMREC could reconstruct the event. To determine the geometric acceptance, π^0's and η's were generated at various locations inside the target volume. These mesons were forced to decay with asymmetry less than 0.75, the same value used in the data analysis. The photons resulting from these decays were then projected to the face of the LAC. The fiducial cuts discussed in section 7.7 were applied to these projected photons. The geometric acceptance is the ratio of the number of photon pairs which hit the active region of the LAC in a single octant divided by all candidates. This acceptance was determined as a function of the transverse position of the interaction, and the pseudorapidity and p_T of the π^0 or η. Pseudorapidity was chosen rather than rapidity to eliminate beam energy dependence from the calculation. Figure 7.14 shows the acceptance for

η's in various p_T bins as a function of rapidity. Based on these plots, a rapidity cut of ± 0.75 was placed on the cross section calculations to avoid regions with small geometric acceptance.

7.10 Trigger Weights

The E706 trigger which has been subjected to the closest scrutiny to date is the Single_Local, and for this reason it was used in this analysis. To correct for the losses due to inefficiencies in the trigger, a trigger weight was calculated for each event based on the probability that the octant containing the high p_T η or π^0 would have been triggered by the event.

To rapidly and reliably estimate the p_T of showers in the EMLAC, the trigger employed individually adjusted electronics channels for each group of 8 R-strips (sum_of_eight) in the EMLAC. The trigger turn-on curves for each sum_of_8, for each octant, had to be calculated for each trigger set prior to calculating the trigger weight associated with each event. Then, based on the event topology in a given octant for a given interaction, and using the database of turn-on curves, a trigger probability was calculated. The trigger weight applied to the cross section was the inverse of this probability.

To determine the turn-on curves for each trigger set, all of the events contained within these sets were utilized. As shown in Fig. 7.15, the turn-on curves are generally quite sharp when measured in trigger p_T. The procedure used to find these curves is as follows. Determine which octant or octants

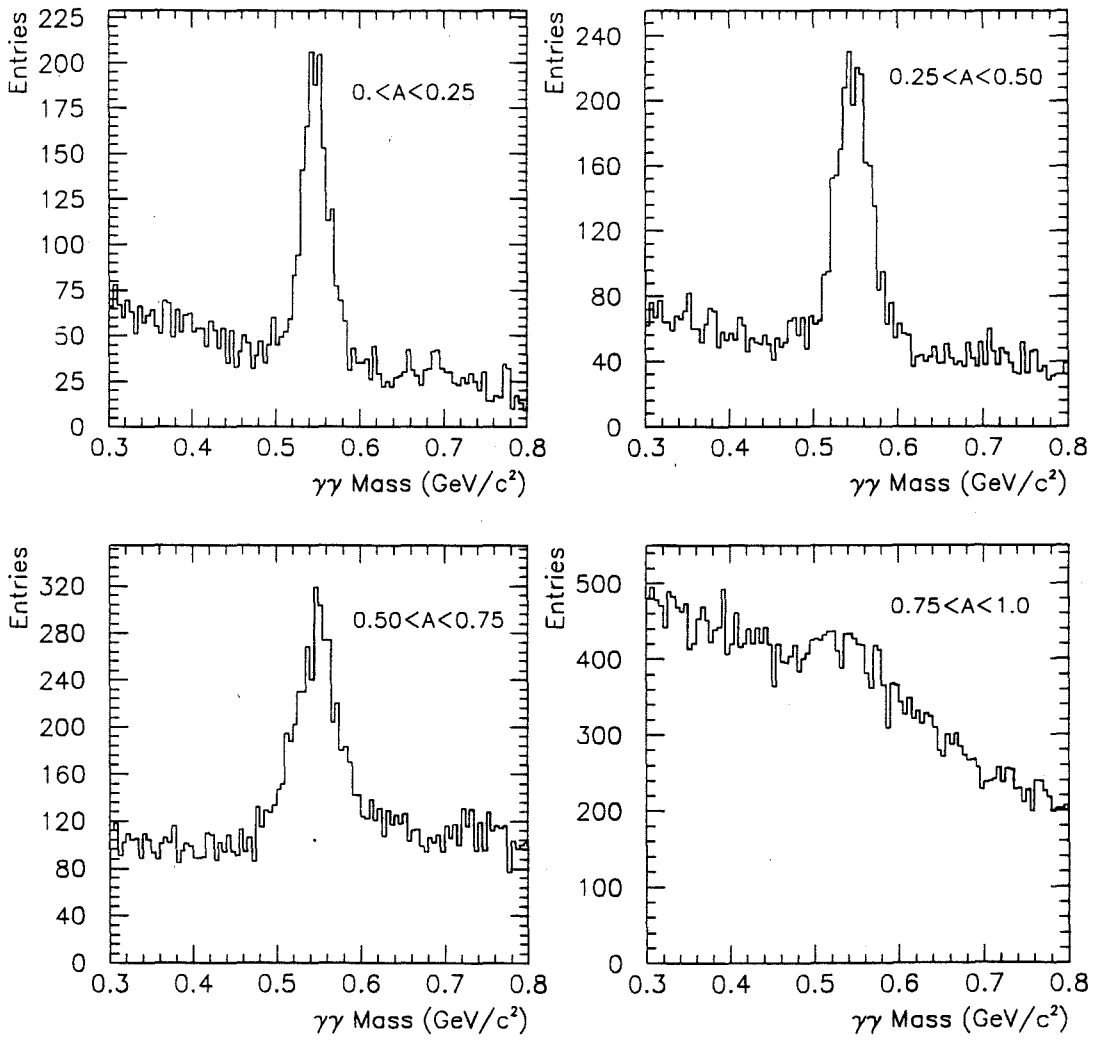

Figure 7.12 Four mass plots of the η region in various energy asymmetry bins for p_T's greater than 4.0 GeV/c.

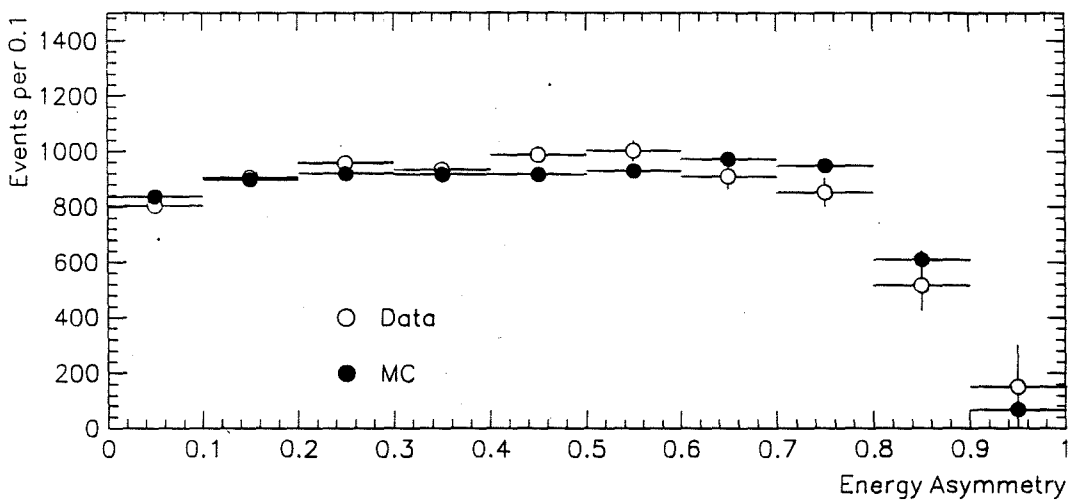

Figure 7.13 The η energy asymmetry distribution for MC (solid) and data (open) for p_T's greater than 4.0 GeV/c.

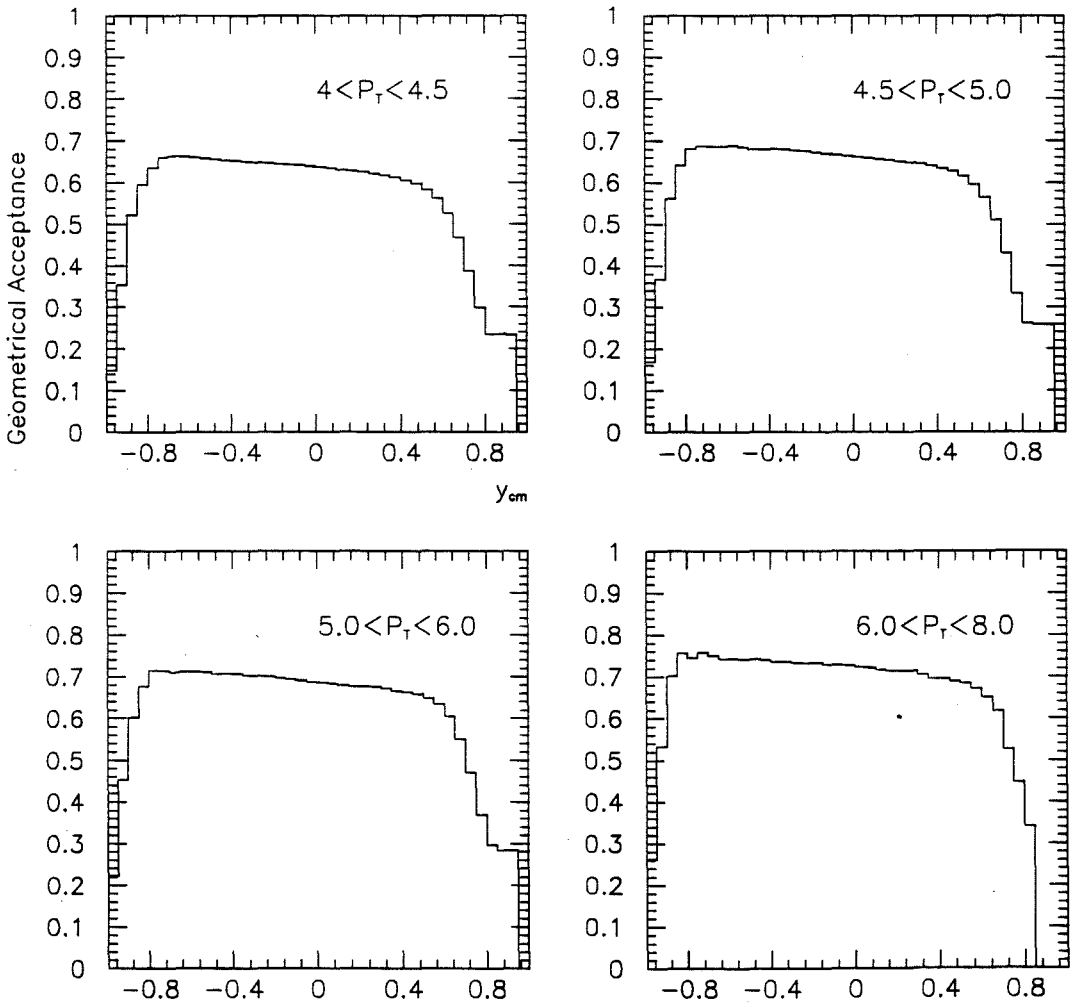

Figure 7.14 Geometric acceptance for η's with an $A \leq 0.75$ in four p_T bins as a function of center of mass rapidity.

triggered an event. Assuming that one octant fired the trigger, examine the remaining 7 octants to calculate the trigger p_T for each of the 31 sections (pairs of sum_of_8 channels). Next, examine the Nanometric trigger banks which were latched to see whether that particular section of the trigger was turned on for that event. The turn-on curve is the ratio of two plots — the numerator contained the trigger p_T for those sections in which the Nanometric [39] trigger banks indicated that the corresponding trigger section fired for that octant and the denominator contained all trigger p_T entries, independent of status of the Nanometric trigger banks.

Based on these turn-on curves, the trigger probability was calculated on an event by event basis using all 31 individual trigger probabilities from all pairs of sums_of_8's in the octant based on the energy distribution in that octant. Mathematically, this can be written as

$$P_{octant} = 1 - [\prod_{i=1}^{31}(1 - P_i)] \qquad 7.6$$

where P_i is the trigger probability for any given section (adjacent sums_of_8 channels). P_i is found for section i using the trigger p_T for that section and the appropriate turn-on curve. For events whose p_T were far above the trigger threshold, the trigger weight (the inverse of the trigger probability) was nearly unity. However, around threshold these weights could be sizeable.

An analysis very similar to the one outlined above can also be carried out for the pretrigger. However, based on the pretrigger turn-on curves shown in Fig.

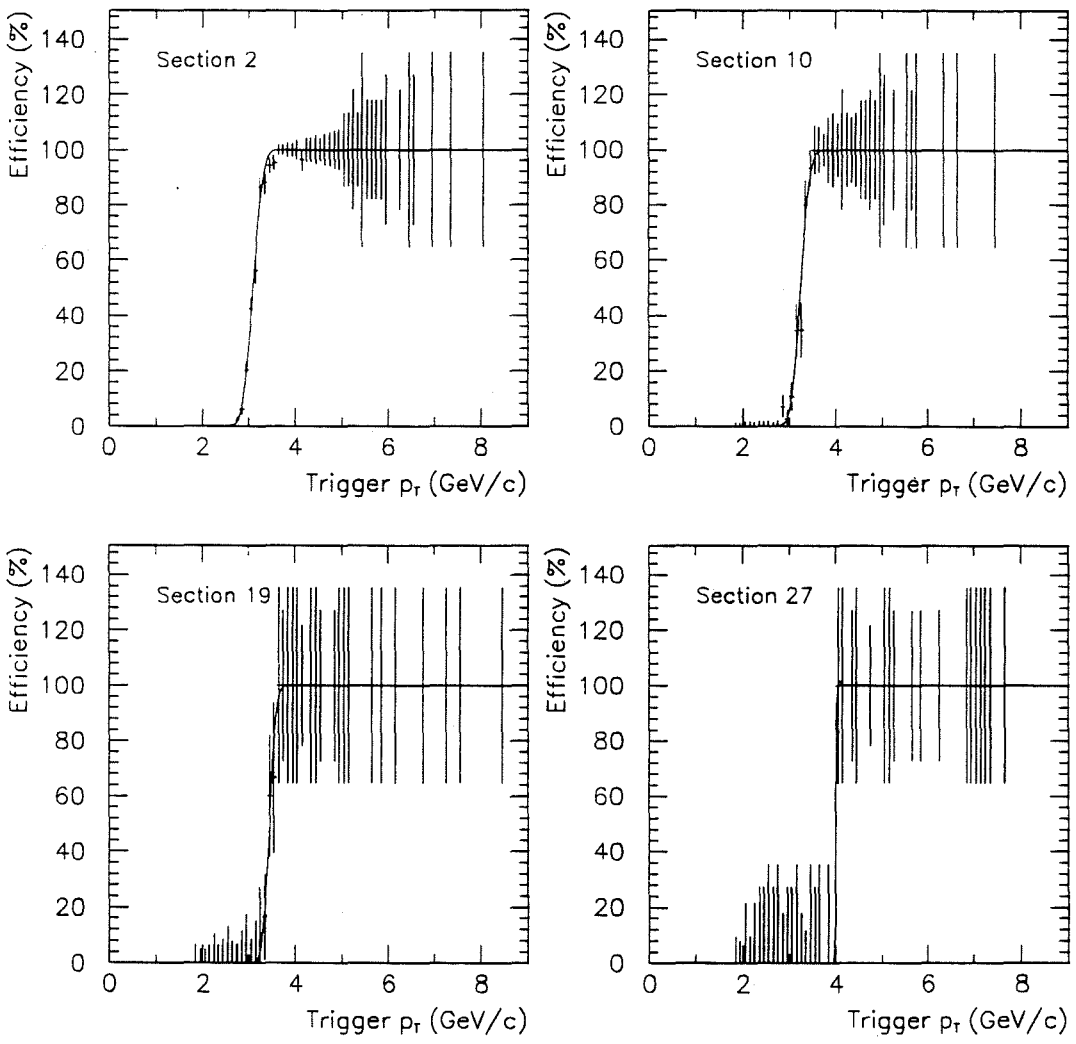

Figure 7.15 Single_Local trigger turn-on curve for four different regions of a typical octant in the EMLAC as a function of trigger p_T.

7.16 for a typical octant, the pretrigger turn-on threshold is very much lower than the p_T range studied in this analysis and thus this correction is negligible.

An event weighting scheme cannot account for classes of events which are never included in the data sample being weighted, and the geometry of the Single_Local trigger generates such a class of events in the case of high p_T η's. This was not a significant issue for π^0's since the separation between the two photons was generally small when compared to the segmentation of the Single_Local trigger definition. However, for η's, with typical photon separations of 20 to 30 cm, this was not the case.

To illustrate this issue, a variable α is displayed in Fig. 7.18a, where α is the angle formed between a line drawn perpendicular to the radial vector drawn from the center of the LAC to the position of the reconstructed meson and the line connecting the two decayed photons. See Fig. 7.17 for a pictorial definition of the angle α. When $\alpha = 0$, the two photons have the same radial value, but different ϕ values. When $\alpha = \frac{\pi}{2}$, the two photons have the same ϕ value, but different radial values. In the data, one expects to see more η's when $\alpha \rightarrow 0$ than when $\alpha \rightarrow \frac{\pi}{2}$ because the Single_Local trigger preferentially selected this class of events. However, in the generated MC event sample, all values of α were equally populated — since the event selection in this case was based solely upon the p_T of the η.

An analysis of the η candidates with $p_T > 3.5$ GeV/c observed in the MC sample generated with a $p_T > 3.0$ GeV/c results in the α distribution shown as

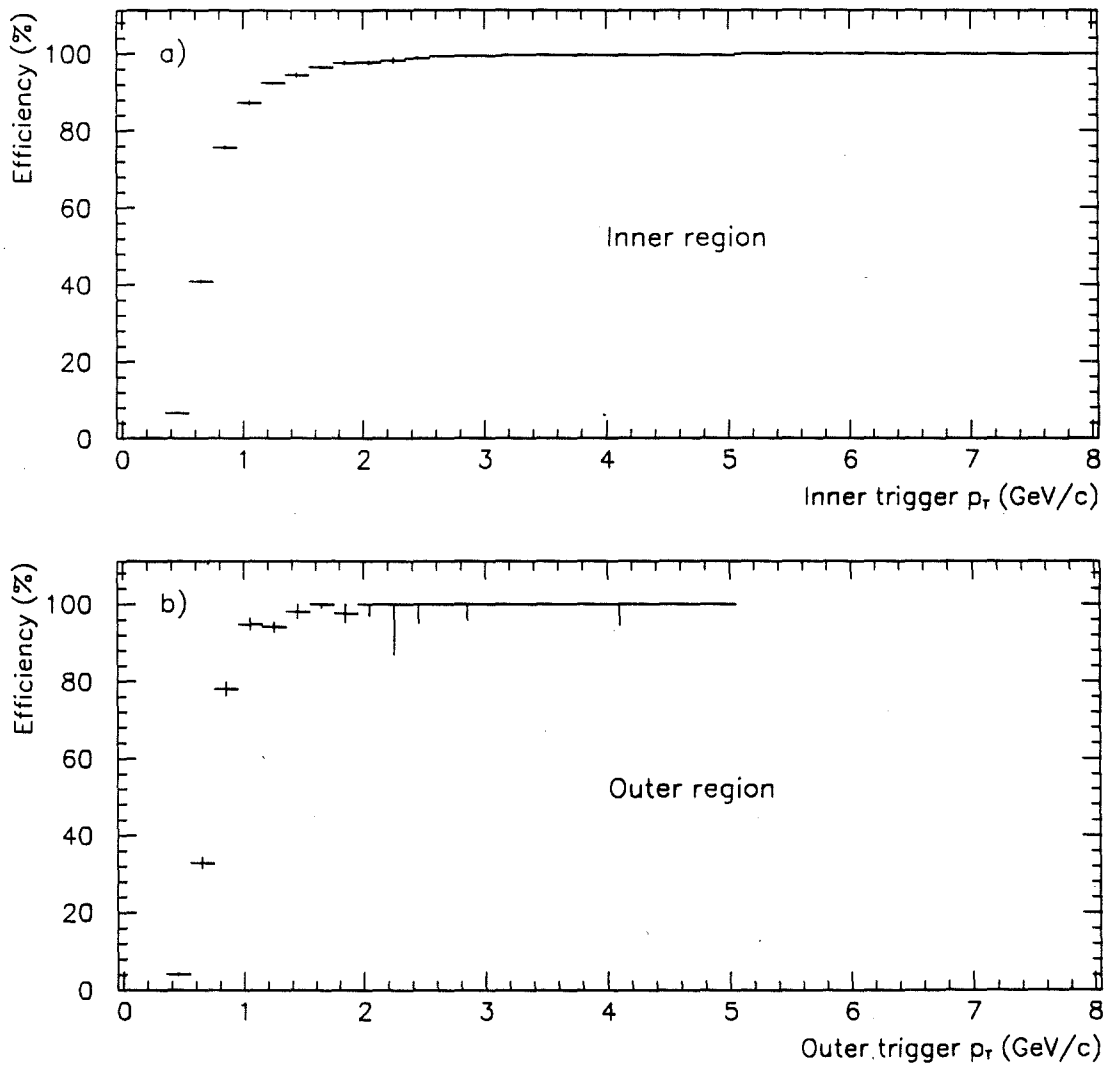

Figure 7.16 Pretrigger turn-on curve for the inner and outer 128 strips of a typical octant in the EMLAC as a function of trigger p_T.

the solid points in Fig. 7.18a. The solid line in Fig. 7.18a shows the distribution of α for η candidates with $p_T \geq 3.5$ GeV/c observed in the data. The entries are weighted by the inverse of the trigger probability and no entry is made for combinations with trigger probability less than the cutoff value of 0.05. (This cutoff value insured that abnormally large event weights were not applied.) The striking difference between these MC and data distributions is attributed to events which satisfy the MC event selection criteria but not the Single_Local trigger. To account for this, the local trigger definition was simulated in the MC preprocessor. Sums_of_8 banks were created and filled with the MC data. Trigger probabilities were determined for each event based upon the trigger efficiencies determined from the data. The MC α distribution was then calculated for only those events whose trigger probabilities were greater than the cutoff threshold used for the data. Comparison between the α distribution from data and the corresponding MC distribution with the trigger cutoff threshold applied is shown in Fig. 7.18b. The agreement between MC and data is a good indication that the trigger has been modeled correctly in the MC.

Another way to study this is to compare the trigger probability curves for MC and data as in Fig. 7.19. For MC, one expects a large excess of η's which have a near zero trigger probability. Those are the events which could not have satisfied the local trigger requirement. These two curves were normalized to each other neglecting the bin at zero. The shape of the trigger probabilities for those events which could be seen in the detector agree, confirming that the impact of the local trigger on the data is simulated properly in the MC.

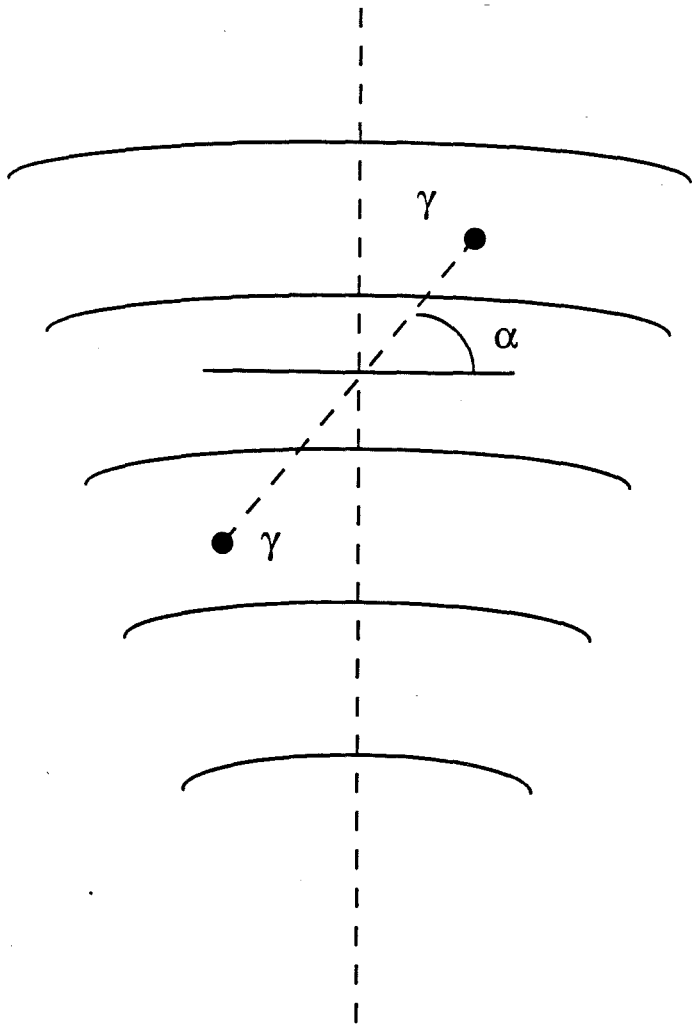

Figure 7.17 A diagram defining the angle α. The two dots represent photons from a π^0 or η decay. The solid curved lines represent the boundaries between R strips in the EMLAC.

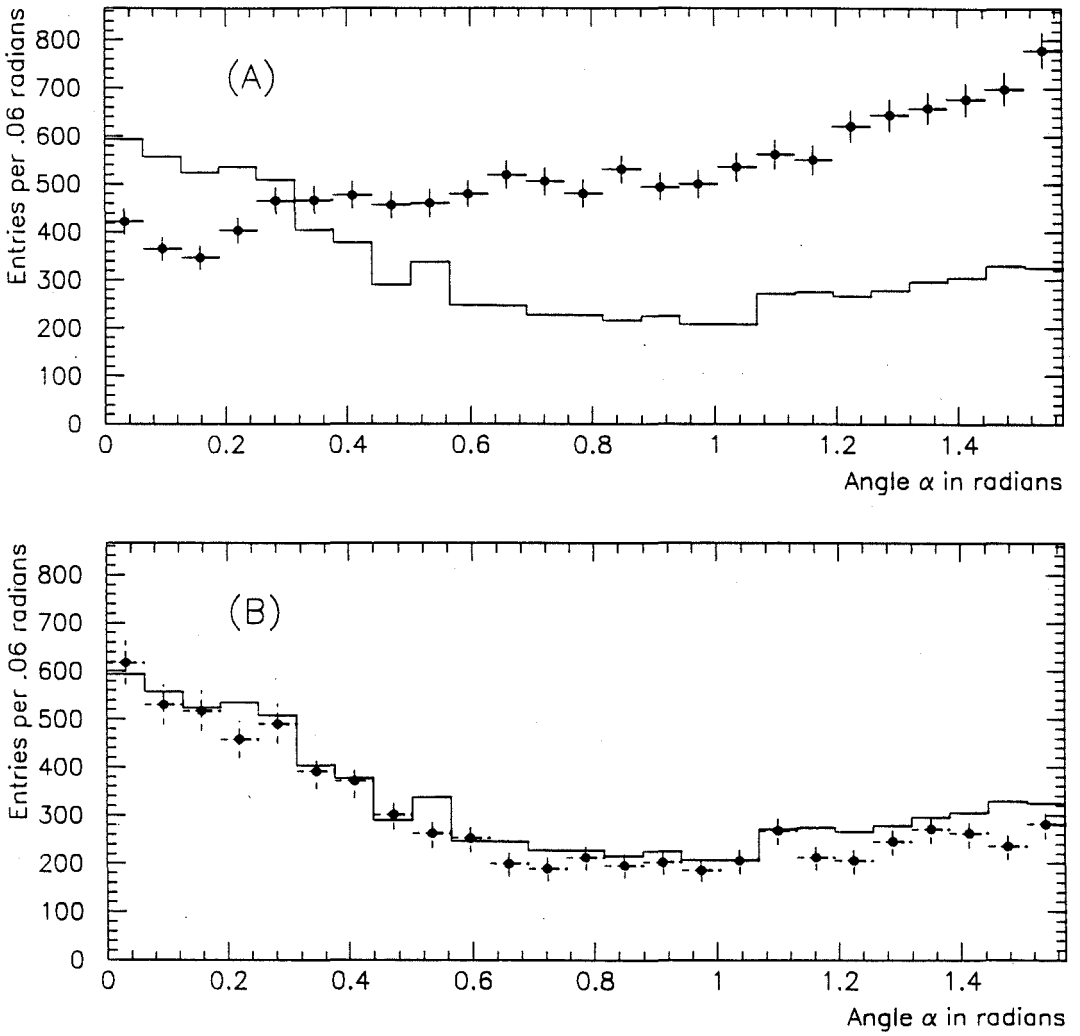

Figure 7.18 A comparison of α values, described in the text, between MC (solid points) and data (histogram) for η's with $p_T > 3.5$ GeV/c. The discrepancy in (a) stems from the differences between the event selection schemes for MC and data; MC selects events based on the p_T of the η while the trigger for the data selects on p_T of the individual photons when those MC η's which are very unlikely to satisfy the Single_Local trigger are removed. The two curves agree as shown in figure b.

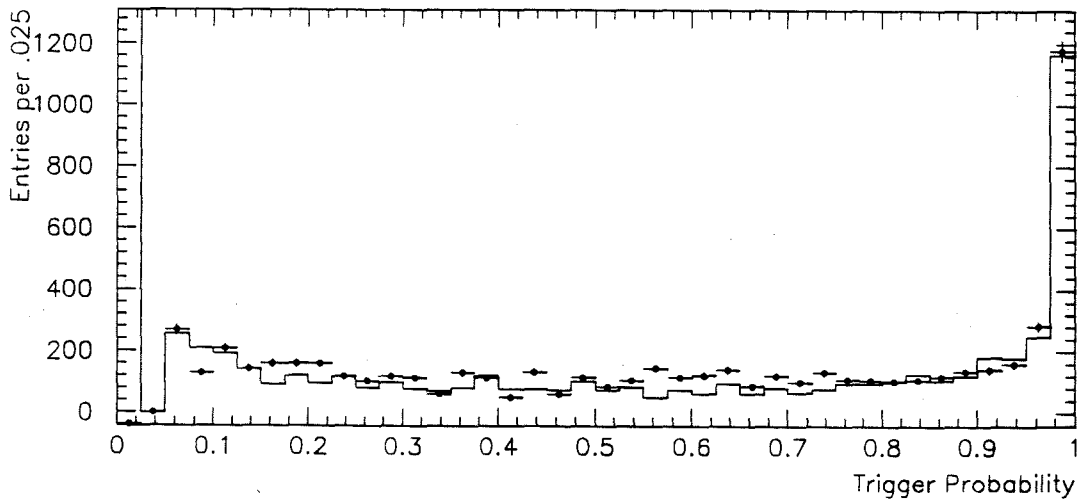

Figure 7.19 A trigger probability curve for η's with $p_T > 3.5$ GeV/c for both MC (histogram) and data (solid points). The excess events near zero probability for the MC is the result of not implementing a local trigger requirement on the generated events. These events typically had an asymmetry value around 0.5 and were spatially oriented so that each photon landed in separate local trigger sections. Since each photon was below trigger threshold, these events would not have satisfied the experimental trigger. Excluding these events that do not satisfy the trigger, the observed agreement indicates that the Single_Local trigger was properly simulated in the MC.

These losses discussed above have been taken into account in the reconstruction efficiency calculation described below.

7.11 Reconstruction Efficiency

The reconstruction efficiency was calculated based upon the sample of HERWIG generated MC events. These MC events were reconstructed using the prescription detailed in Chapter 6. For the π^0's, the reconstruction efficiency is the ratio of the number of reconstructed π^0's to the number of generated π^0's. For η's, the "reconstruction efficiency" is the ratio of the number of reconstructed η's with Single_Local trigger probability above the cutoff threshold of 0.05 to the number of generated η's. Only photons with $E_{front}/E_{total} > 0.2$ contributed to reconstructed π^0's or η's. Furthermore, only those η's that reconstructed within the signal region as defined in section 7.4 contributed to the count of reconstructed η's. This ratio was calculated as a function of p_T and rapidity. Figure 7.20 illustrates this reconstruction efficiency for η's.

7.12 Photon Conversion

Photons from π^0 and η decays sometimes convert into an electron/positron pair prior to reaching the LAC. If this conversion takes place downstream of the magnetic field of the analysis magnet, the position of the pair in the LAC will be the same as would have been the position of the photon and the energy measurement will be approximately correct. However, if the conversion occurs upstream of the magnet, the electron and positron will be swept apart and the

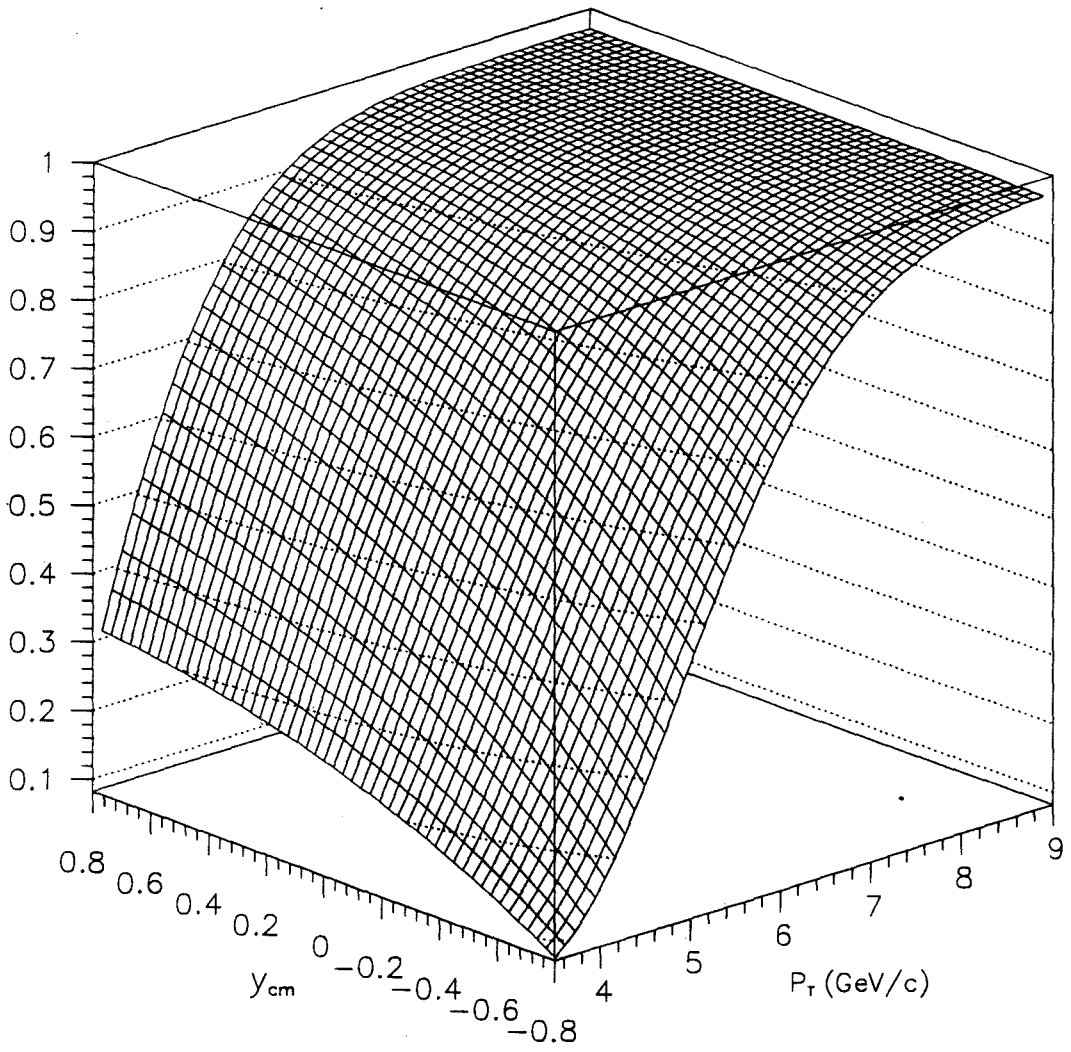

Figure 7.20 The reconstruction efficiency for η's as a function of p_T and rapidity.

LAC will detect two separate particles. One can either try to reconstruct these converted photons or else correct for the losses. For this analysis, a weight was calculated for each π^0 and η mesons reconstructed. The correction was based on the position of the reconstructed vertex and the angles which defined the amount and type of material which were traversed by photons prior to reaching the end of the magnetic field. The behavior of this correction is illustrated in Fig. 7.21.

7.13 Live Beam Count

The live beam count was calculated using scaler information acquired after each spill during the data taking process. The scalers were read out and written to the standard data output stream. In this experiment, the live_triggerable_beam was not directly counted. Live_triggerable_beam is the number of beam particles incident on target while the spectrometer is ready to record an interaction. To count live_triggerable_beam directly, the scalers themselves would have had to have been incorporated into the trigger system. Given the distances between various elements of the trigger, this was not considered feasible. Instead, the scalers were used to measure the live fraction and the total beam. To use this technique, a variety of quantities had to be measured.

- Clean Interaction Fraction — the fraction of interactions that satisfy the requirement that there be no other interaction within ± 60 ns of the interaction of interest. The clean interaction

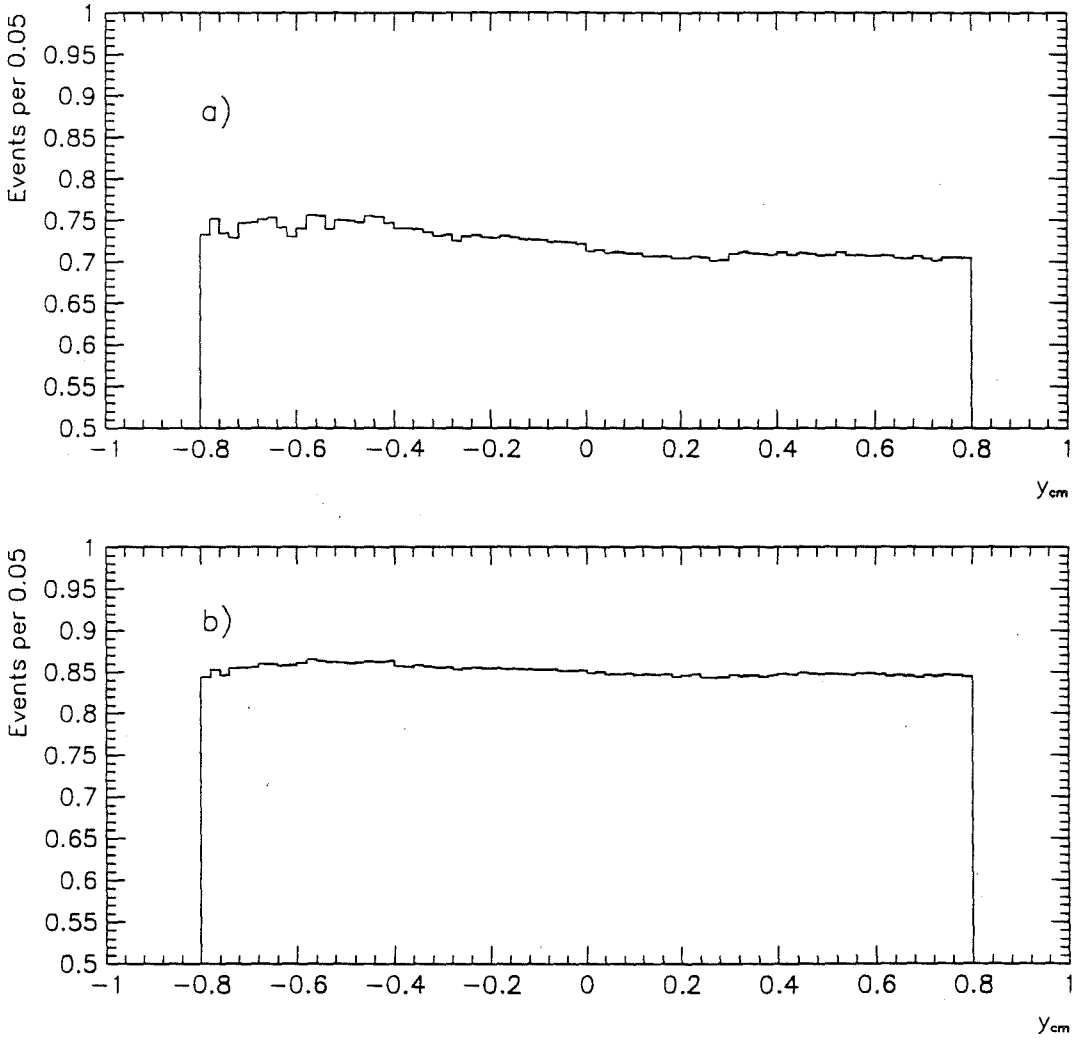

Figure 7.21 The probability that a photon converted into an e^+e^- pair in the region between the target and the end of the magnetic field for events which interacted in Cu (a) and events which interacted in Be (b).

requirement contributed to the dead time since an interaction was ignored if a second interaction occurred within this window.

- Computer Live Fraction — The fraction of interactions for which the data acquisition system was ready to trigger.
- Pretrigger Live Fraction — the fraction of pretrigger decisions not ignored due to busy pretrigger logic.
- Veto Live Fraction — the fraction of interactions not vetoed due to a coincidence with signals from the muon veto walls, power supply noise (SCRKILL), or by early deposition of p_T (residual energy from the previous event).

$$LiveFraction = \begin{pmatrix} CleanInteraction \\ Fraction \end{pmatrix} \times \begin{pmatrix} ComputerLive \\ Fraction \end{pmatrix} \times \begin{pmatrix} PretriggerLive \\ Fraction \end{pmatrix} \times \begin{pmatrix} VetoLive \\ Fraction \end{pmatrix} \quad 7.7$$

The Live_Triggerable_Beam is a product of this Live_Fraction and the total count of isolated beam particles which were not vetoed by the beam hole counter as expressed below:

$$Live\_Triggerable\_Beam = BEAM1 \bullet \overline{BH} \times LiveFraction \quad 7.8$$

7.14 Cross Section Calculation

The invariant cross section per nucleon is given by the expression:

$$E\frac{d\sigma}{d^3p} = \frac{N^{corr}(p_T, y)}{B(p_T)} \frac{1}{\rho l N_a} \quad 7.9$$

where the corrected differential distribution of the number of η's is

$$N^{corr}(p_T, y) = \sum_{\gamma\gamma comb.} \frac{N_{obs} W_{vw} W_{Dir*BAPT/p_T} W_{trig} W_{conv}}{C_{abs} 2\,\pi\, p_T \,\triangle\, p_T \,\triangle y E_A a E_{recon} E_{vrtx} B_R} \qquad 7.10$$

The meanings of the symbols in the above expressions are:

- N_{obs} : Number of signal particles observed;
- ρ : The density of the target material;
- l : The length of the target;
- N_a : Avogadros' number;
- W_{vw} : Correction for losses due to veto wall cut;
- $W_{Dir*BAPT/p_T}$: Correction for losses due to directionality and balanced p_T ratio cut;
- W_{trig} : Weight to account for trigger inefficiencies;
- W_{conv} : Weight to account for photon conversions;
- C_{abs} : Correction to account for beam absorption;
- $\triangle p_T$: Bin width in p_T;
- $\triangle y$: Bin width in rapidity;
- E_A : Correction for losses due to energy asymmetry cut;
- a : Geometric acceptance (including correction for fiducial cut);
- E_{recon} : Reconstruction efficiency (including correction for E_{front}/E_{total} cut, definition of signal region, and trigger cutoff threshold);
- E_{vrtx} : Vertex reconstruction efficiency;

- B_R : Branching ratio of $\eta \rightarrow \gamma\gamma$ decay mode;
- B_{p_T} : The number of beam particles incident on the fiducial region of the upstream face of the copper target.

	Beam and Target Type	
Correction	π^- on Be	π^- on Cu
Geometric Acceptance	Function of p_T and Rapidity	
Reconstruction Efficiency	Function of p_T and Rapidity	
Trigger Acceptance	Function of Run and p_T	
Photon Conversions	Function of V_z and θ	
Asymmetry < 0.75	1.3333	
BAPT and DIR	1.0452	
Veto Wall	1.0840	
Branching Ratio	0.389	
Vertex Efficiency	1.0040	
Beam Muon Contamination	1.0050	
Target Correction	1.3469	
Beam Absorption	Function of V_z	
λ of Si used in ABS	60.730	
λ used in ABS	57.953	19.289
Density (gm/cm^3)	1.848	8.96
Atomic Number	9	63.5

Table 7.2 Summary of the corrections applied to the data.

C_{abs} is given by the expression

$$C_{abs} = exp(-\triangle Z/\lambda_{Cu}) \tag{7.11}$$

for interactions in copper and

$$C_{abs} = [exp(-l_{Cu}/\lambda_{Cu}] \times [exp(-\triangle Z/\lambda_{Be}] \tag{7.12}$$

for interactions in beryllium, where $\triangle Z$ is the length of copper (beryllium) traversed by the incident beam particle prior to the interaction and λ_i is the pion interaction length of the target material [40].

The beam count, $B(p_T)$, differs from p_T bin to p_T bin due to the use of data sets containing runs with different trigger thresholds. $B(p_T)$ is given by the expression

$$B(p_T) = (Live\_Triggerable\_Beam) \times C_{Si} \times C_N \times C_{target} \tag{7.13}$$

where C_{Si} is a correction for beam absorption in the SSD's upstream of the target, C_N is a correction for the muon content of the beam [41] and C_{target} is the correction for the target fiducial cut.

The values of these correction factors are listed in Table 7.2 for π^- beam on Be and Cu targets. The cross sections reported in the following chapter were calculated as described in this section.

Chapter 8 Results

8.1 Cross Sections

Tables 8.1 and 8.2 show the invariant cross sections per nucleon for high p_T η production by 520 GeV/c π^- beam on Be for three regions of rapidity, as well as for the full rapidity range, as a function of p_T. A graphical representation of these data is presented in Figs. 8.1 and 8.2. The shapes of the cross section in rapidity for each of the four p_T bins (Fig. 8.1) are similar. Similarly, the cross sections as a function of p_T (Fig. 8.2) also have the same general shape. Figures 8.3 and 8.4 show the cross sections for η production on Be and Cu, respectively, over the rapidity region $-0.75 < y_{c.m.} < 0.75$. The data shown in these plots can be found in Tables 8.3 and 8.4.

The curves in Figs. 8.3 and 8.4 represent next-to-leading-log (NLL) QCD calculations based upon code provided by Greco *et al.* [8] using parton distribution functions for the pion and nucleon from Aurenche *et al.* [42] [43]. The cross sections are calculated for two choices of scale ($Q^2 = p_T^2$ and $Q^2 = p_T^2/4$). These calculated cross sections have been adjusted by the factor $A^{\alpha-1}$, where A is the appropriate atomic weight and $\alpha = 1.125 \pm 0.031$ is the average value measured for all p_T's in order to take into account nuclear dependence effects. This will be discussed further in section 8.2. Agreement between data and theory is better for the smaller choice of scale. The overall

shape of the NLL QCD calculation matches the data very well, but the curve, for the scale $Q^2 = p_T^2/4$ remains below the data by approximately 30%.

E706 also measured high p_T η production for 500 GeV/c π^- on Be during the 1988 fixed target run. A comparison of the present results with those obtained from the 1988 data is shown in Fig. 8.5. The 1988 measurement is low when compared to the current data. A fraction of this difference is attributed to the difference in beam energies between the two data samples. The curve on this plot is ratio of two NLL calculations for high p_T η's at $Q^2 = p_t^2/4$. The numerator in this ratio was calculated for a incident beam momentum of 520 GeV/c while the denominator had an incident beam momenta of 500 GeV/c; the ratio of beam momenta for the two data runs. The remaining difference between the two measurements is on the order of the systematic uncertainties associated with these measurements.

8.2 Nuclear Dependence

The expression for the cross section per nucleon, given by equation 7.9, was obtained by dividing the observed cross section per nucleus by A. However, effects such as nuclear shadowing or secondary scattering in the nucleus can result in deviations of the cross sections from a simple linear dependence on the number of nucleons per nucleus. The form A^α, with α being a parameter that can depend on rapidity, p_T, and on the nature of the particle in question, is often used to parametrize the A dependence. In order to determine α, the ratio of the measured cross section on Be to that on Cu was calculated. Specifically,

y_{cm}	4.0< p_T <4.5	4.5< p_T <5.0	5.0< p_T <6.0	6.0< p_T <8.0
-0.75→-0.60	660±330	130±86	29±15	2.4±1.7
-0.60→-0.45	1950±400	220±150	68±17	1.3±1.6
-0.45→-0.30	2000±400	460±120	111±17	3.6±1.9
-0.30→-0.15	2500±300	601±77	144±18	6.8±1.8
-0.15→0.00	2780±300	751±88	92±20	7.4±2.0
0.00→0.15	2230±260	709±90	125±21	7.4±2.0
0.15→0.30	2560±260	655±93	106±20	4.2±2.1
0.30→0.45	2340±250	746±79	160±16	7.4±2.0
0.45→0.60	1880±230	763±87	140±16	9.6±2.0
0.60→0.75	1940±180	593±73	111±15	6.2±1.8

Table 8.1 Invariant differential cross section for the inclusive reaction $\pi^- + Be \rightarrow \eta + X$. Cross sections are per nucleon in units of $pb/(GeV/c)^2$. Errors reported are purely statistical.

$$\sigma_{Cu}/\sigma_{Be} = (A_{Cu}/A_{Be})^{\alpha-1} \qquad 8.1$$

so that α is

$$\alpha = 1 + \frac{ln(\sigma_{Cu}/\sigma_{Be})}{ln(A_{Cu}/A_{Be})} \qquad 8.2$$

where σ_{Cu}, σ_{Be} are the measured cross sections per nucleon in the specified target. Table 8.5 shows the measured values of α for high p_T η production. The average value determined for α is 1.125 ± 0.031, which is one standard deviation above the corresponding value for high p_T π^0 production obtained from this data sample (1.083 ± 0.003) [32]. Both the π^0 and η results are consistent with

p_T (GeV/c)	-0.75< y_{cm} <-0.20	-0.2< y_{cm} <0.2	0.2< y_{cm} <0.75
3.50 → 3.75	6200±1000	14700±1100	11700±770
3.75 → 4.00	4250±600	6510±550	5700±400
4.00 → 4.25	2180±330	3470±280	2790±210
4.25 → 4.50	1170±190	1610±160	1540±110
4.50 → 4.75	480±100	1003±97	816±72
4.75 → 5.00	166±62	474±55	536±43
5.00 → 5.50	125±16	173±24	205±15
5.50 → 6.00	35.7±6.8	56±9.0	61.4±6.8
6.00 → 7.00	5.7±1.8	12.0±2.4	12.9±1.9
7.00 → 8.00	0.13±0.44	2.21±0.75	1.76±0.60
8.00 → 9.00	—	0.01 ±0.25	0.27±0.17

Table 8.2 Invariant differential cross section for the inclusive reaction $\pi^- + Be \rightarrow \eta + X$. Cross sections are per nucleon in units of $pb/(GeV/c)^2$. Errors reported are purely statistical.

previous measurements of α for high p_T production of mesons as reported by the Chicago-Princeton group [44], as well as recent measurements from Fermilab experiment E605 [45] for similar regions of p_T as shown in Fig. 8.6.

No measurement of the A dependence of high p_T η production was available from the E706 1988 run due to limited statistics on Cu. The NLL curves in Figs. 8.3 and 8.4 have been calculated using a value of α equal to 1.125.

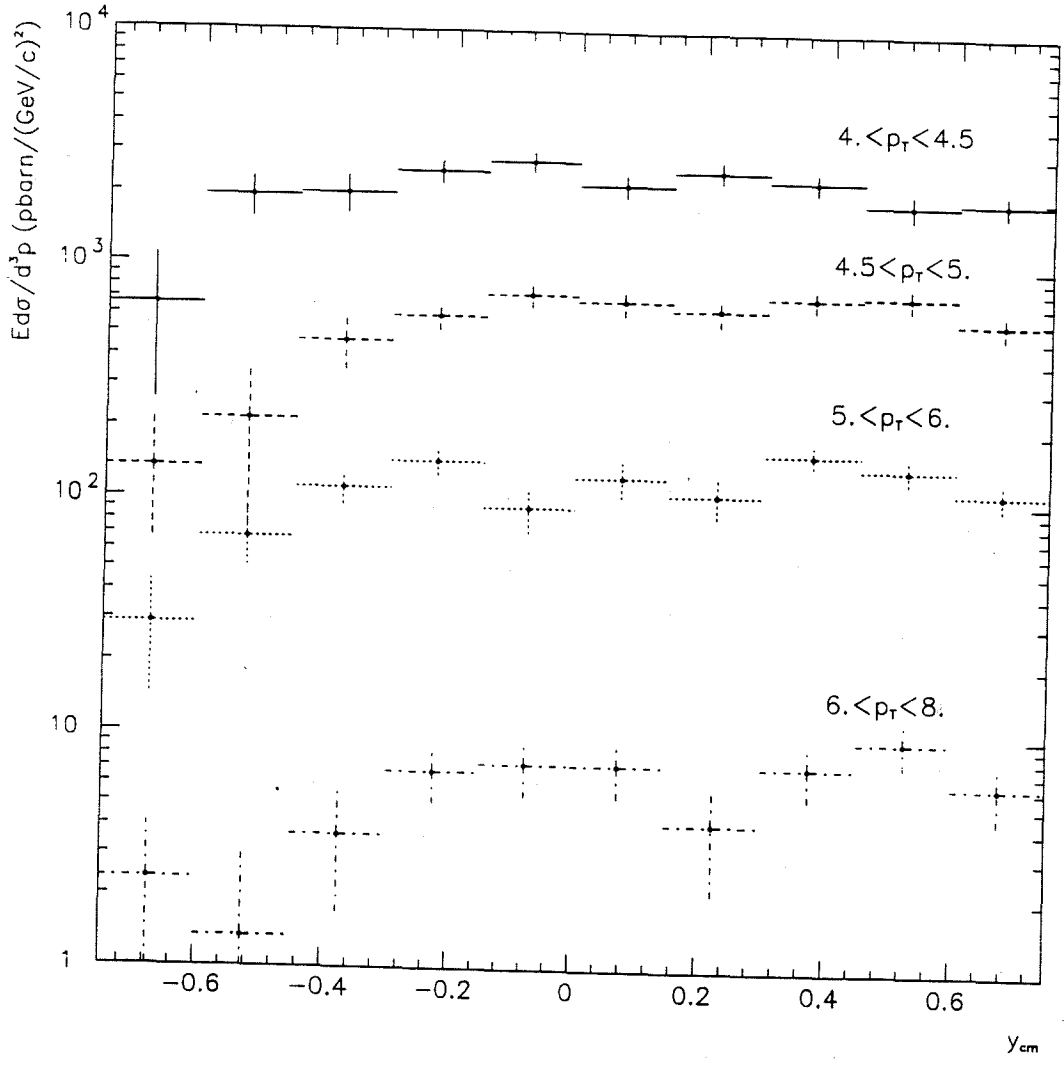

Figure 8.1 Invariant cross sections per nucleon for η production in π^- interactions on Be as a function of rapidity averaged over four different p_T ranges.

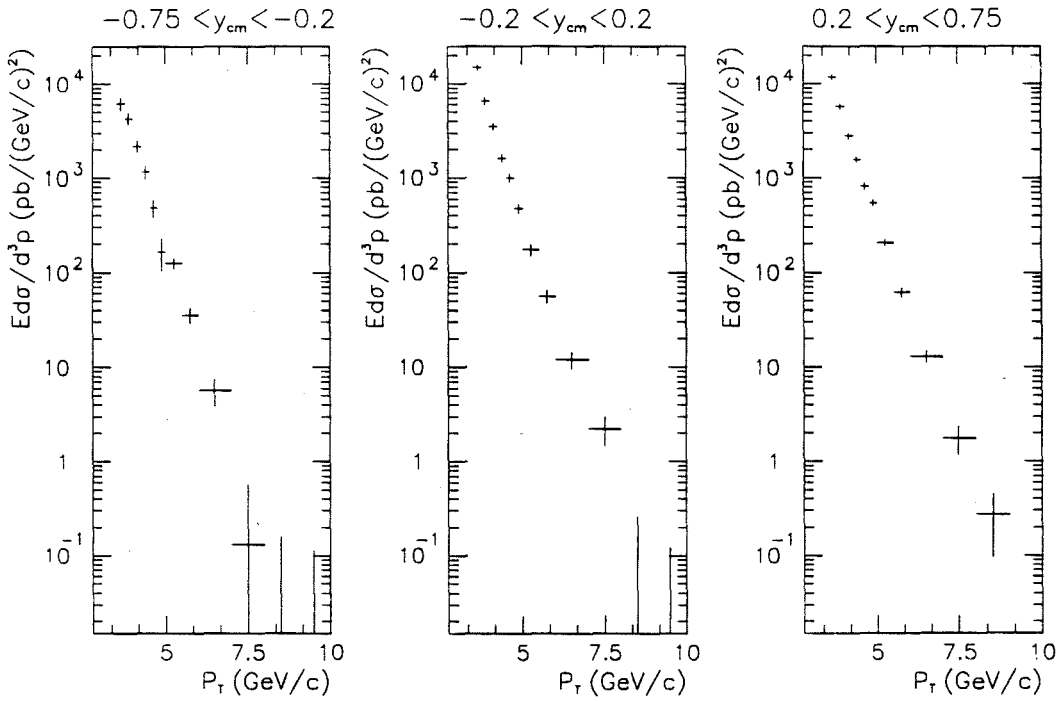

Figure 8.2 Invariant cross sections per nucleon for η production in π^- interactions on Be as a function of p_T averaged over three different rapidity ranges.

p_T (GeV/c)	$\pi^- + Be \rightarrow \eta + X$
3.40 → 3.60	13670 ± 870
3.60 → 3.80	8080 ± 520
3.80 → 4.00	5370± 300
4.00 → 4.20	2930± 190
4.20 → 4.40	1610± 120
4.40 → 4.60	1140± 73
4.60 → 4.80	586± 48
4.80 → 5.00	355± 32
5.00 → 5.25	215± 17
5.25 → 5.50	119± 10
5.50 → 5.75	67.3± 7.0
5.75 → 6.00	33.7± 4.9
6.00 → 6.50	15.9± 2.0
6.50 → 7.00	4.1± 1.2
7.00 → 7.50	1.31± 0.58
7.50 → 8.00	1.26± 0.35
8.00 → 9.00	0.10± 0.10

Table 8.3 Invariant differential cross section for the inclusive reaction $\pi^- + Be \rightarrow \eta + X$ averaged over the rapidity range of $-0.75 < y_{c.m.} < 0.75$. Cross sections are per nucleon in units of $pb/(GeV/c)^2$. Errors reported are purely statistical.

8.3 η/π^0 Ratio

The ratio of η to π^0 production for π^- beam on both copper and beryllium targets is shown in Fig. 8.7 for the p_T range 3.5 GeV/c to 9 GeV/c. The

p_T (GeV/c)	$\pi^- + Cu \rightarrow \eta + X$
3.50 → 3.75	15200 ± 2000
3.75 → 4.00	5580 ± 890
4.00 → 4.25	3050 ± 480
4.25 → 4.50	1990 ± 270
4.50 → 4.75	990 ± 170
4.75 → 5.00	459 ± 87
5.00 → 5.50	212 ± 47
5.50 → 6.00	62 ± 13
6.00 → 7.00	15.0 ± 3.8
7.00 → 8.00	2.16 ± 0.87

Table 8.4 Invariant differential cross section for the inclusive reaction $\pi^- + Cu \rightarrow \eta + X$ averaged over the rapidity range of $-0.75 < y_{c.m.} < 0.75$. Cross sections are per nucleon in units of $pb/(GeV/c)^2$. Errors reported are purely statistical.

data is also listed in Table 8.6. The π^0 cross section was calculated using the identical data sample. The cuts used in the π^0 analysis were nearly identical as well. The details of the π^0 analysis can be found elsewhere. [32] There is no significant dependence on either p_T or target material. The average value of η/π^0 is 0.52 ± 0.012 for Be and 0.56 ± 0.04 for Cu. E706 measured this ratio using its 1988 data sample of 500 GeV/c π^- on Be and found it to be $0.44 \pm 0.05 \pm 0.05$. The new measurement is higher than the one based on the 1988 data sample, but the difference is only $\approx$ 1.5 standard deviations in statistical uncertainty. Figure 8.8 summarizes the E706 results and those of previous measurements. The data from these experiments indicate no apparent dependence of the η/π^0

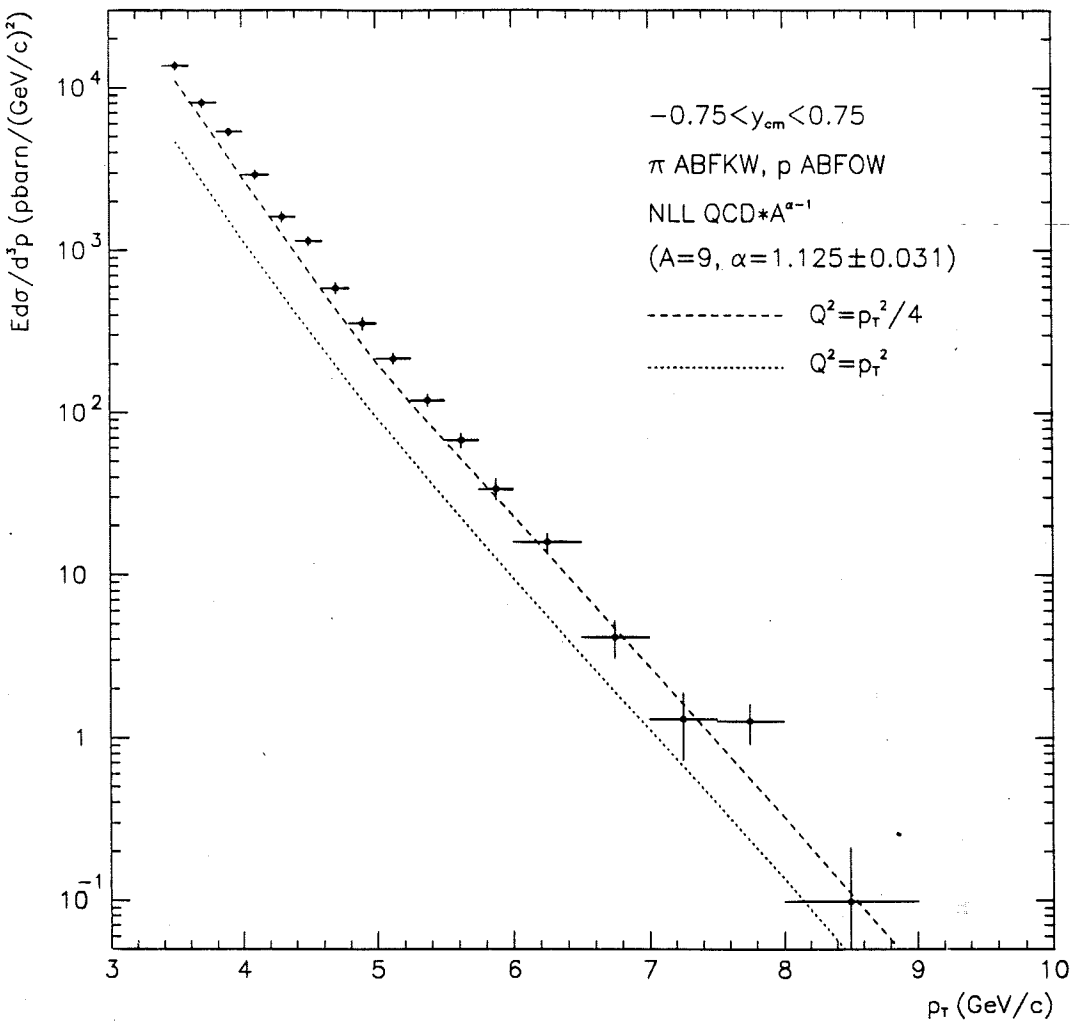

Figure 8.3 Invariant cross section per nucleon for η production in π^- interactions with Be at 520 GeV/c. Cross sections are shown for $p_T > 3.5$ GeV/c over the full rapidity range $-0.75 < y_{c.m.} < 0.75$. The curves represent NLL QCD calculations described in the text.

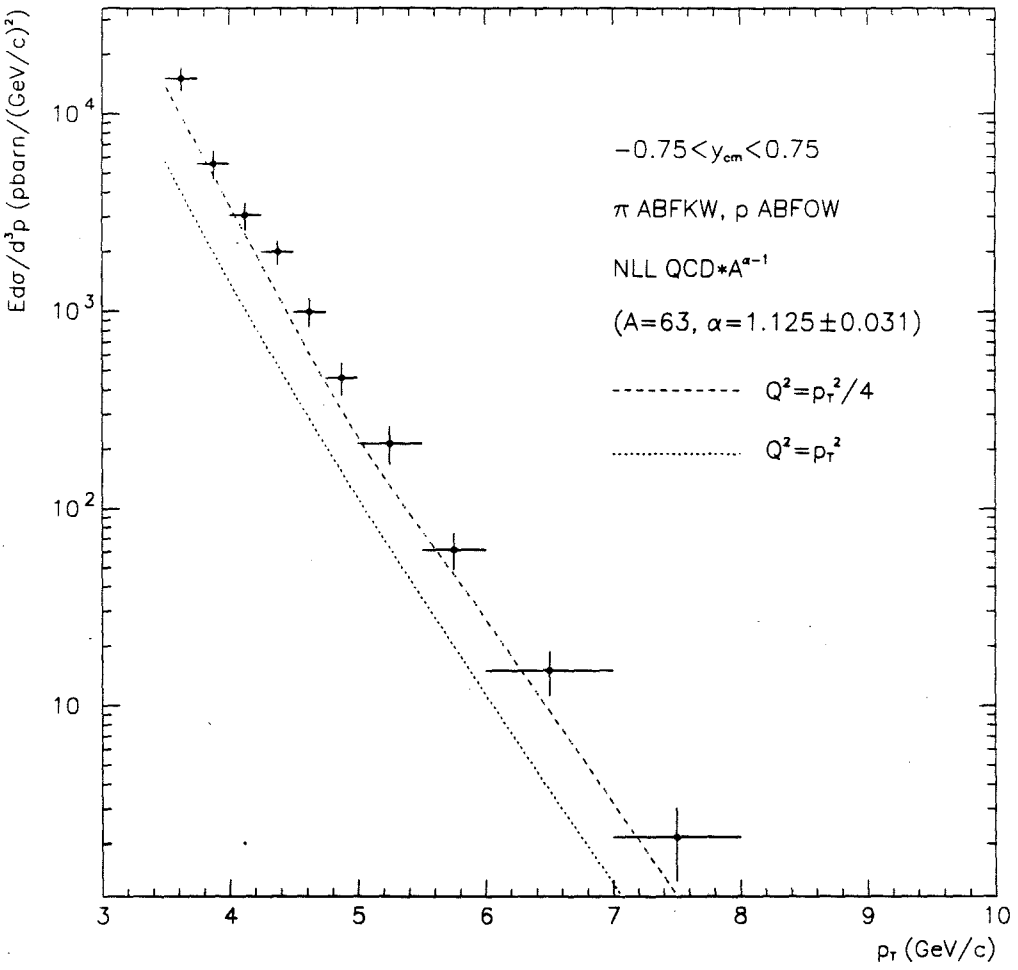

Figure 8.4 Invariant cross section per nucleon for η production in π^- interactions with Cu. Cross sections are shown for $p_T > 3.5$ GeV/c over the full rapidity range $-0.75 < y_{c.m.} < 0.75$. The curves represent NLL QCD calculations for Be scaled by the appropriate A^α value for Cu.

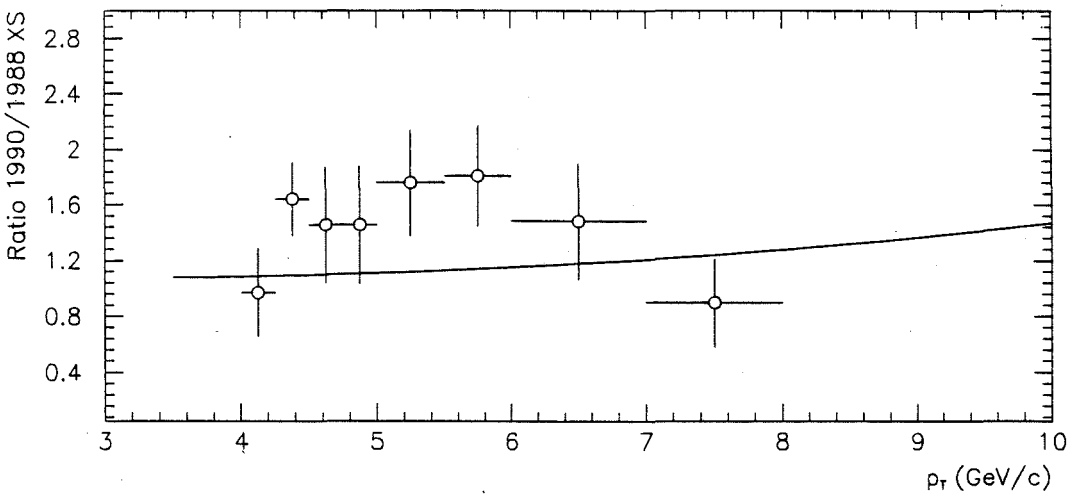

Figure 8.5 A ratio of the 1990/1988 results for the invariant cross section per nucleon in η production for π^- interactions with Be average over the rapidity range of $-0.7 < y_{c.m.} < 0.7$. The curve is the ratio of two NLL calculations processed at the appropriate beam momenta for each of the data sets.

p_T (GeV/c)	α_{π^-}
3.5 $\rightarrow$ 4.0	1.137 $\pm$ 0.058
4.0 $\rightarrow$ 4.5	1.097 $\pm$ 0.060
4.5 $\rightarrow$ 5.0	1.129 $\pm$ 0.073
5.0 $\rightarrow$ 5.5	1.12 $\pm$ 0.12
5.5 $\rightarrow$ 6.0	1.10 $\pm$ 0.11
6.0 $\rightarrow$ 7.0	1.12 $\pm$ 0.14
7.0 $\rightarrow$ 8.0	1.13 $\pm$ 0.25
3.5 $\rightarrow$ 8.0	1.125 $\pm$ 0.031

Table 8.5 Values for α averaged over the rapidity range of $-0.75 < y_{c.m.} < 0.75$ for π^- interactions at 520 GeV/c. α was determined assuming an A^α dependence for the cross sections on Be and Cu. Errors reported are purely statistical.

production ratio upon x_T ($x_T = 2p_t/\sqrt{s}$) nor any significant difference between incident pions or nucleons.

8.4 Systematic Uncertainties

The primary contributions to the systematic uncertainties arise from the following sources:

- Uncertainty in the determination of the EMLAC energy scale: Based on the analysis of the final distribution of $\gamma\gamma$ pairs in the π^0 and η mass ranges, the estimated uncertainty in the energy scale is 0.5%. This translates into $\approx$ 6% uncertainty in the cross sections.

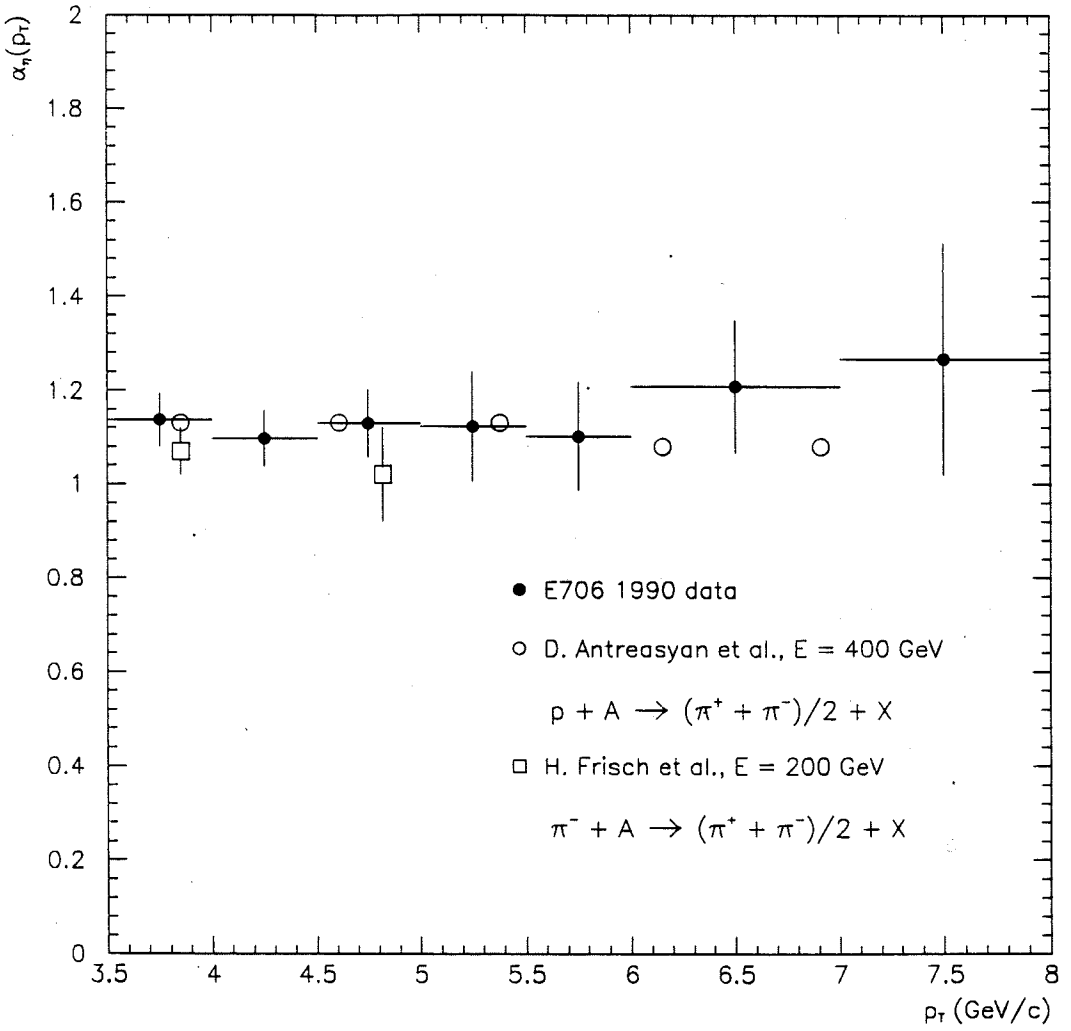

Figure 8.6 α as a function of p_T determined from the ratio of η cross sections for 520 GeV/c π^- interactions on beryllium and copper (solid dots) as well as comparisons to the Chicago-Princeton and E605 data for high p_T meson production in similar regions of p_T.

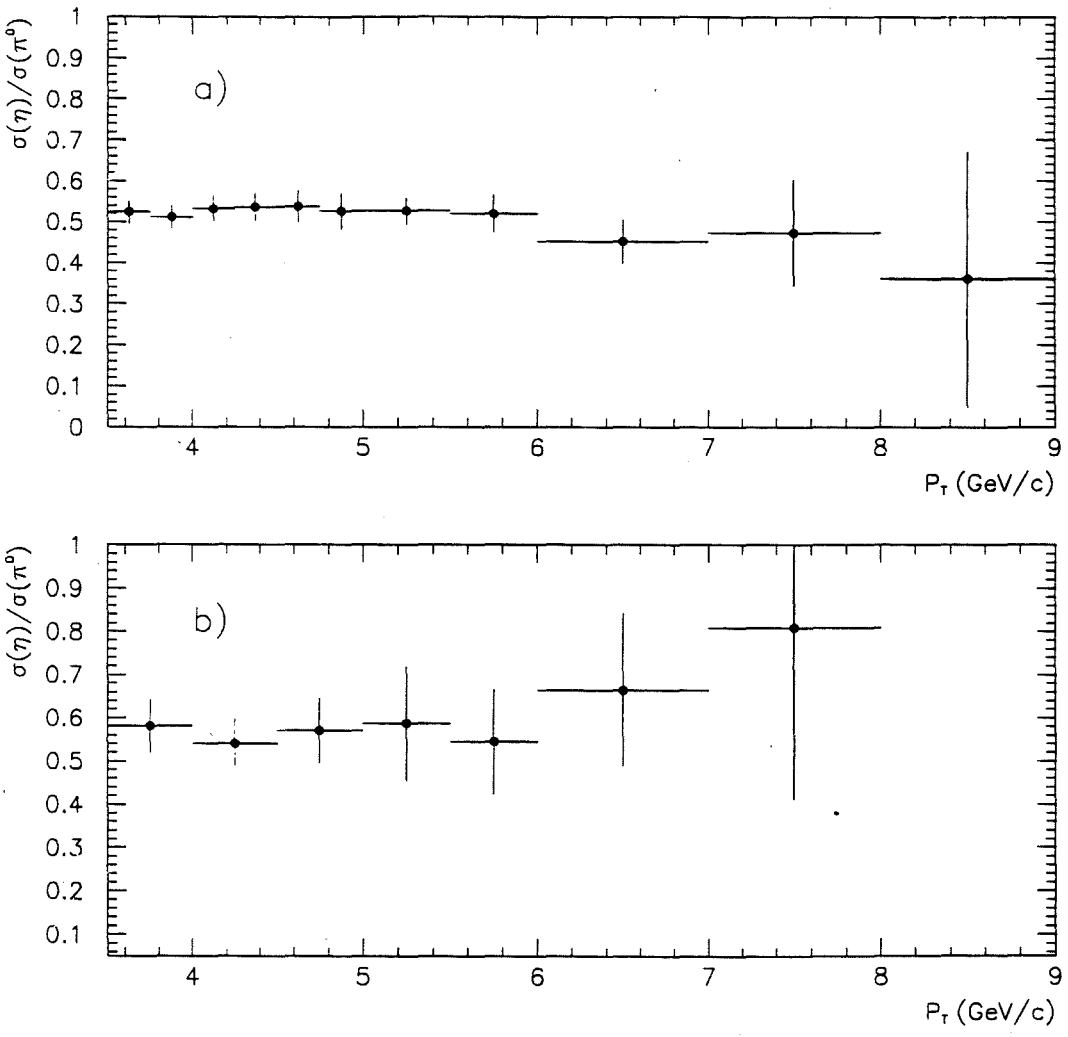

Figure 8.7 The ratio of η to π^0 production for π^- beam as a function of p_T on beryllium (a) and copper (b) targets.

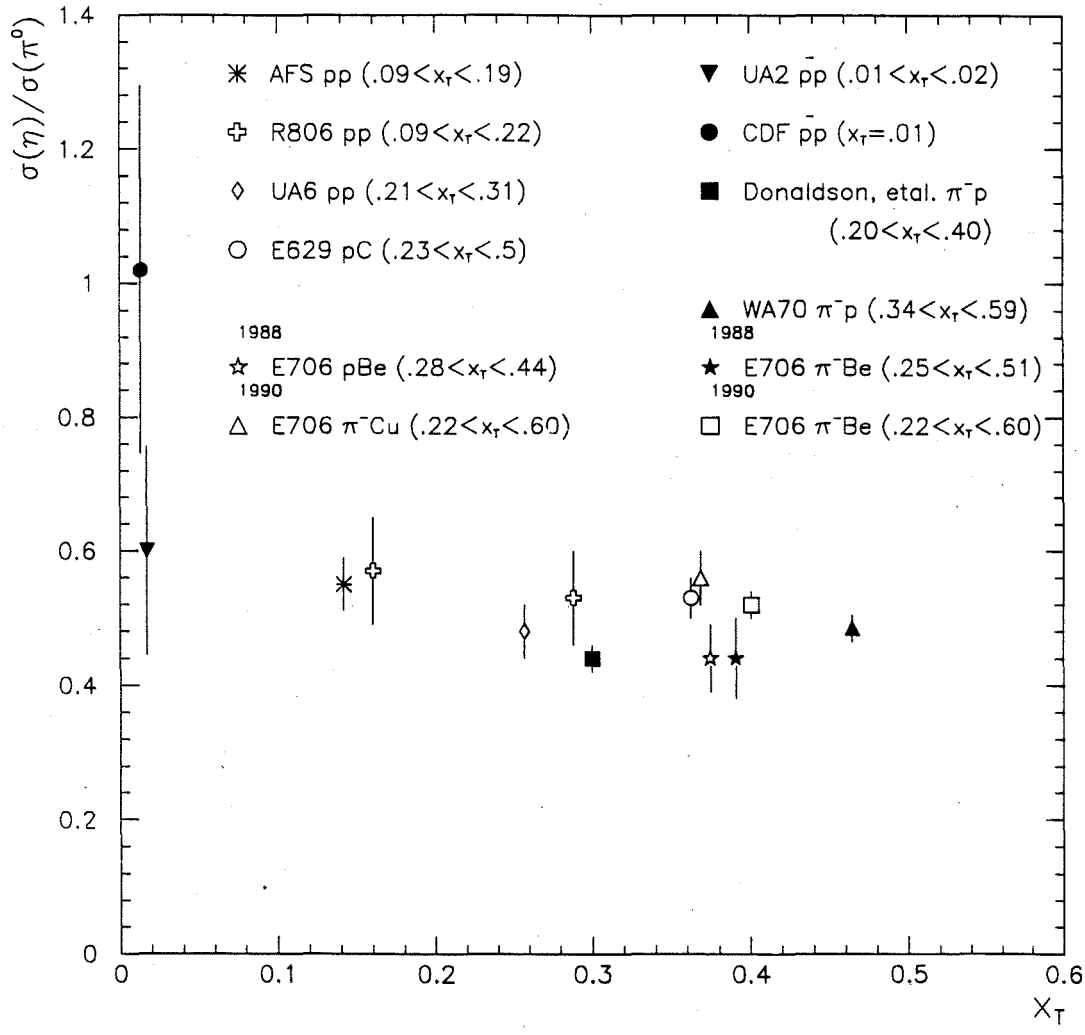

Figure 8.8 Ratio of the cross sections for η production to π^0 production as a function of x_T $(= 2p_T/\sqrt{s})$ for high p_T production experiments. The range in x_T covered by each experiment is listed and the data point is positioned at the center of this range.

p_T (GeV/c)	η/π^0 on Be
3.50 → 3.75	0.520 ± 0.032
3.75 → 4.00	0.518 ± 0.034
4.00 → 4.25	0.531 ± 0.033
4.25 → 4.50	0.531 ± 0.036
4.50 → 4.75	0.541 ± 0.041
4.75 → 5.00	0.526 ± 0.042
5.00 → 5.50	0.530 ± 0.038
5.50 → 6.00	0.523 ± 0.044
6.00 → 7.00	0.452 ± 0.050
7.00 → 8.00	0.48 ± 0.10
8.00 → 9.00	0.36 ± 0.31
3.5 → 9.0	0.520 ± 0.012

p_T (GeV/c)	η/π^0 on Cu
3.50 → 4.00	0.584 ± 0.068
4.00 → 4.50	0.546 ± 0.066
4.50 → 5.00	0.574 ± 0.071
5.00 → 5.50	0.59 ± 0.13
5.50 → 6.00	0.54 ± 0.12
6.00 → 7.00	0.66 ± 0.18
7.00 → 8.00	0.81 ± 0.40
3.5 → 8.0	0.56 ± 0.04

Table 8.6 Ratio of η/π^0 production for 520 GeV/c on Cu and Be as a function of p_T averaged over the entire rapidity region $-0.75 < y_{c.m.} < 0.75$. Errors reported are purely statistical.

- Uncertainty in the determination of the Monte Carlo EMLAC energy scale: Based on the analysis of the Monte Carlo $\gamma\gamma$ pairs in the π^0 and η mass ranges, the estimated uncertainty in the Monte Carlo energy scale is also 0.5%. This also translates into $\approx$ 6% uncertainty in the cross sections.
- Uncertainty in the magnitude of the trigger corrections: The uncertainty in the trigger correction is p_T dependent and ranged from $\approx$ 5% to $\approx$ 1%. The uncertainty in the trigger corrections

is larger for backward rapidities due to the limited statistics with which to calculate the trigger probabilities.

- Uncertainty in the the reconstruction efficiency: Studies were done on the stability of the reconstruction efficiency determination. For η's, this measurement was estimated to be accurate to within $\approx 5\%$, independent of p_T or rapidity.
- Uncertainty in the correction for photon conversions: The photon conversion correction is sensitive to the precise description of the materials encountered by the photons. The systematic uncertainty associated with the current version of this correction is estimated to be $\approx 10\%$. Studies are underway which should eventually allow a reduction in this uncertainty.
- Uncertainty in the beam normalization: At this stage in the analysis, the uncertainty in the beam normalization is estimated to be 10%.

Other uncertainties which contribute to a lesser extent include:

- Uncertainty due to the K^- content of the beam: Since the study of the identification of minority particles is in progress, results from the 1988 data sample were employed to estimate the contribution to the uncertainty due to the failure to tag the kaon content of the beam in this analysis. As previously cited, the kaon content of the beam is expected to be $\approx 3\%$, and based upon an analysis of the

1988 data, the η/π^0 reported for K^- beam was 0.65 ± 0.15. [46] Thus the reported η cross section has an uncertainty of $\approx 2\%$ due to failure to tag the kaons in this analysis.

- Uncertainty in the vertex reconstruction efficiency: Studies of the corrected number of observed J/ψ's as a function of position within the Be target indicate a systematic uncertainty in the vertex reconstruction efficiency of 2%.
- Uncertainty in the target fiducial cut correction: The variation in the position of the beam relative to the target was measured as described in section 7.3. The systematic uncertainty associated with the target fiducial cut correction is estimated to be $\approx 2\%$.
- Uncertainties in the definition of signal: The definition of the η signal and the associated side-band subtraction technique contribute to the systematic uncertainties. Studies were done using an alternative technique (see Section 7.5) and the variation in the measured cross section was on the order of 1%.
- Uncertainties in the correction for muon cuts: The correction for losses due to the muon cuts is estimated to have an uncertainty of 1% above $p_T > 5.5$ GeV/c.

These numbers added in quadrature yields a net systematic uncertainty in the η cross section of $\approx 18\%$.

Since the A dependence measurement is a ratio of cross sections, several above cited systematic uncertainties do not contribute to uncertainties in α. However, the measurement of α is sensitive to the determination of the vertex reconstruction efficiency and the photon conversion correction. Thus, at this stage of the analysis, the systematic uncertainty in the reported value of α is estimated to be ± 0.05.

For the η/π^0 measurement, many of the above systematic uncertainties cancel in calculating this ratio. The components of the systematic uncertainty which are relevant to the η/π^0 ratio include: a small fraction of the energy uncertainties to account for differences in the energy measurement between π^0's and η's, uncertainties in reconstruction efficiencies, uncertainties in the trigger correction, and the contribution of the kaon component of the beam to the η production. The systematic uncertainty in the η/π^0 ratio is estimated to be 7%.

The central value of the beam momentum was uncertain to $\approx 2\%$ [47]. This introduces an systematic uncertainty of $\approx 4\%$ at $p_T = 4$ and 13% at $p_T = 9$ in the comparisons with theoretical expectations.

Chapter 9 Conclusions

The study of high p_T inclusive hadron production offers the possibility of providing insights into hard scattering phenomena as well as testing the theory (QCD) used to describe strong interactions.

In this thesis, high p_T η production was studied using data collected during the 1990 fixed target run at Fermilab. The data correspond to an integrated luminosity of 5.2 events/pb on Be. The experiment measured the inclusive η cross section as a function of p_T and rapidity for 520 GeV/c π^- beam incident on Be and Cu targets, covering the kinematic regions of transverse momentum between 3.5 and 9 GeV/c and rapidity between -0.75 and 0.75 and represent the highest energy results ever obtained for inclusive η production using a π^- beam. The η cross sections have been compared with next-to-leading-log expectations from QCD. The agreement between data and the QCD calculation improves for low values of the Q^2 scale. This observation is consistent with results obtained from comparisons of high p_T π^0 production to QCD expectations.

The NLL QCD calculation for high p_T π^0 production using a $Q^2 = p_T^2/4$ is in excellent agreement with the data. Our measured η/π^0 ratio also agrees well with the world average. However, the current NLL QCD calculations for high p_T η production using a $Q^2 = p_T^2/4$ is about 30% lower than our data. These new data will help improve the current theoretical understanding of high p_T η production. For example, results from the HERWIG Monte Carlo on η production had been used as input for the fragmentation process in the

above QCD calculation because of the lack of experimental data on high p_T η production at these energies.

The nuclear dependence of high p_T η production in 520 GeV/c π^- interactions on Be and Cu has been parametrized by the form A^α. The measured value of α is $1.125 \pm 0.031 \pm 0.05$ and no p_T dependence is observed over the kinematic range $3.5 < p_T < 8$ GeV/c. This value of α is consistent with previous measurements of the nuclear dependence of neutral and charged pion production in similar kinematic regimes.

The ratio of η to π^0 production was measured to be $0.520 \pm 0.012 \pm 0.04$ on Be and $0.56 \pm 0.04 \pm 0.04$ on Cu. These results are consistent with an overall fit to world data. Efforts are underway to identify K^- particles in the incident beam. If this is successful, conclusions can be drawn regarding the relative importance of gluon, sea and valence quark fragmentation in the production of high p_T η mesons.

References

[1] G. Alverson *et al., Phys. Rev. D* **V48.1** (1993) 6.

[2] M. Gell-Mann, Phys. Lett. 8, 214 (1964). G Zweig, CERN Rep. TH 401, 412 unpublished. 1964.

[3] J.F. Owens,*Rev. Mod. Phys.* **59 No.2** (1987), 465-503.

[4] M.R. Pennington, *Rep. Prog. Phys.* **V46** (1983), 393-515.

[5] T. Ferbel and W.R. Molzon, *Rev. of Mod Phys.,* **56** (1984),181.

[6] D. Perkins, *Introduction to High Energy Physics*, Addison-Wesley, (1982) 188-196.

[7] B. Webber, *et al., Computer Physics Communications***V67** (1992), 465-508.

[8] M. Greco and S. Rolli, *Next to Leading Order Eta Production at Hadron Colliders*, Preprint FNT/T-93/13 1993.

[9] F. Abe *et al, Physics Review Letters* **68** (1992), 2734.

[10] G.J. Donaldson, *et al., Physics Review Letters* **V40,11** (1978), 684.

[11] J.Povlis, *et al., Physics Review Letters* **V51,11** (1983), 967.

[12] M. Bonesini, *et al., Zeitschrift fur Physik C* **42** (1989), 527-532.

[13] J. Antille, *et al., Physics Letters B,* **V194,4** (1987), 568.

[14] T. Akesson, *et al., Physics Letters* **158B** (1985), 282.

[15] F.W.Busser, *et al., Physics Letters* **55B,2** (1975), 232.

[16] C. Kourkoumelis,*et al., Phsics Letters* **84B,2** (1979), 277.

[17] E. Engels, *et. al., Nucl. Instru. and Methods* **A253** (1987), 523-529.

[18] K. Hartman, *Hadronic Production of* π^0 *Paris and Associated Event Structure*, PhD Thesis, Pennsylvania State University, 1990.

[19] C. Bromberg, *et. al., Nucl. Instru. and Methods* **A307** (1991), 292-297.

[20] W. Desoi, *Construction and Performance of a Liquid Argon Calorimeter for Use in E706 at FNAL*, PhD Thesis, University of Rochester, (1990).

[21] C. Lirakis, *A study of High Transverse Momentum* η *Production in 530 GeV/c Hadron Interactions*, PhD Thesis, Northeastern University, 1990.

[22] R. Benson, *Characteristics of Forward Energy Production in Proton-Nucleus and Pion-Nucleus Collisions at 530 GeV/c*, PhD thesis, University of Minnesota, 1990.

[23] VAXONLINE System, FNAL Computer Department PN 252.

[24] *IEEE Standard Fastbus Modular High-Speed Data Acquisition and Control System*, ANSI/IEEE 1985, ISBN 471-84472-1.

[25] G. Drake, *et al., Nucl. Inst. Meth. in Phys.* **A269** (1988), 68-81.

[26] C. Lirakis *E706 Data Acquisition System*, George Blanar, editor, Proceedings of The First Annual Conference on Electronics for Future Colliders, LeCroy Corporation, (1991), 37–50.

[27] 1821 Users's Manual, HN58, LeCroy Corporation. (1987).

[28] 1892 Users's Manual, LeCroy Corporation. (1987).

[29] Technical Manual, STR500 General Purpose Master, Struck Corporation (1988).

[30] L. Sorrell Internal E706 Note – in progress.

[31] R. Brun, *et al.*, ZEBRA Users Guide, Cern Program Library No.DD/EE/85-6.

[32] N. Varelas, π^0 *Production at High Transverse Momenta from* π^- *Collisions at 520 GeV/c on Be and Cu Targets*, PhD Thesis, University of Rochester, (1994).

[33] M. Zielinski, Private communication.

[34] Steve Blusk, PhD thesis, University of Pittsburgh, 1995.

[35] R. Brun, *et al.*, GEANT3 Users Guide, Cern Program Library No. DD/EE/84-1.

[36] Messel and Crawford, *Electron-Photon Shower Distribution Function Tables for Lead, Copper, and Air Absorbers*, Pergamon Press, 1970.

[37] H.U. Bengtsson and T. Sjostrand, *Computer Physics Commun.* **46** (1987) 43.

[38] J. Mansour Internal E706 Note 186.

[39] Multi Wire Proportional Chamber Readout Systems - MWPC-1, Nanometric Systems, Inc., Oak Park, Il.

[40] A. Carroll *et al., Phys. Lett.* **B 80** (1979), 319.

[41] G. Osborne Internal E706 Note 197.

[42] P. Aurenche, *et al., Phys. Rev.* **D 39** (1989), 3275.

[43] P. Aurenche, *et al., Phys. Lett.* **B 233** (1989), 517.

[44] H Frisch, *et al., Phys. Rev.* **D 27** (1983), 1001.

[45] D. Antreasyan, *et al., Phys. Rev.* **D 19** (1979), 764.

[46] D. Skow, *A Study of High Transverse Momentum Eta Meson Production*, PhD Thesis, University of Rochester, 1990.

[47] W. Baker, Private communication.